UNIVERSITÁ DI PADOVA

DIPARTIMENTO DI SCIENZE CHIMICHE

CORSO DI LAUREA MAGISTRALE IN CHIMICA INDUSTRIALE

TESI DI LAUREA MAGISTRALE

SYNTHESIS OF CARBON NANOSTRUCTURE DERIVATIVES AS FILLERS IN SCAFFOLDS FOR TISSUE ENGINEERING

Relatore: Prof. Enzo Menna

Controrelatore: Prof.ssa Francesca Arcudi

LAUREANDO: Francesco Sbalchiero

ANNO ACCADEMICO 2023-2024

Table of contents

Abbreviations

CNT: Carbon Nanotubes

CNH: Carbon Nanohorns

MWCNT: Multi-Wall Carbon Nanotubes

SWCNT: Single-Wall Carbon Nanotubes

SWCNH: Single-Wall Carbon Nanohorns

rGO: reduced Graphene Oxide

f-MWCNT: functionalized Multi-Wall Carbon Nanotubes

f-CNS: functionalized Carbon Nanostructures

f-SWCNH: functionalized Single-Wall Carbon Nanohorns

f-rGO: functionalized reduced Graphene Oxide

CNS: Carbon Nano Structures

MWCNH-S: Multiwall Carbon Nanohorns functionalized with benzenesulfonate group

MWCNH-N: Multiwall Carbon Nanohorns functionalized with N, N, N-trimethyl aminobenzene group

PLLA: poly-(L)-lactic acid

MW: Molecular Weight

AD: Arc-Discharge

LA: laser ablation

CVD: Chemical Vapor Deposition

TGA: Thermogravimetric Analysis

FD: Functionalization Degree

FG: Functional Group

UV-Vis-NIR: Ultraviolet-Visible-Near infrared spectroscopy

DLS: Dynamic Light Scattering

ZP: Zeta Potential

TEM: Transmission Electron Microscopy

CHP: N-cyclohexyl-2-pyrrolidone

PDI: Polydispersion Index

Fmoc: 9-fluorenylmethyloxycarbonyl

DMSO: Dimethyl Sulfoxide

DMEM: Dulbecco's Modified Eagle Medium

DMF: Dimethylformamide

TLC: Thin Layer Chromatography

NMR: Nuclear Magnetic Resonance

ESI-MS: Electro-Spray Ionization Mass Spectrometry

CHP: N-Cyclohexyl-2-pyrrolidone

Abstract

This thesis project concerns the study of chemical modification of carbon nanostructures, in particular single-walled nanohorns (SWCNH), multi-walled nanotubes (MWCNT) and reduced graphene oxide (rGO) to be used as fillers in composites to promote cell growth and differentiation and tissue regeneration. The aim of this project is to provide a variety of functionalizations of CNS with different organic moieties, in particular benzenesulfonate, methylsulfonylbenzene, trimethylbenzeneammonium and N-(p-aminobenzoyl) glycine groups.

All the functionalizations have been carried out by using Tour reaction, a versatile and relatively fast method to attach organic groups on the surface of carbon nanostructures. On CNS derivatives Thermogravimetric analysis, Dynamic Light Scattering, Zeta Potential, UV-Vis-NIR, Raman spectroscopy and FT-IR spectroscopy were performed. Water dispersibility was estimated by using sonication/centrifugation procedures.

Riassunto

Questo progetto di tesi riguarda lo studio della modificazione chimica e la caratterizzazione di nanostrutture di carbonio, in particolare nanoconi di carbonio a parete singola (SWCNH), nanotubi di carbonio a parete multipla (MWCNT) e ossido di grafene ridotto (rGO), da utilizzare in futuro come riempitivi nei compositi per favorire la crescita e la differenziazione delle cellule e la rigenerazione dei tessuti.

Il progetto è stato dedicato allo studio dell'effetto della funzionalizzazione di nanostrutture di carbonio con particolare interesse dal punto di vista della disperdibilità in acqua.

SWCNH e rGO sono stati funzionalizzati utilizzando la reazione di Tour con gruppi benzenesolfonato, metilsulfonilbenzene, trimetilbenzenammonio e N-(p-amminobenzoil)glicina per ottenere derivati disperdibili in acqua con diversa polarità, invece, MWCNT sono stati funzionalizzati solo con il gruppo N-(p-amminobenzoil)glicina, mentre gli altri tre gruppi sono già stati studiati su MWCNT nel precedente lavoro di tesi. Su ciascun derivato del CNS sono state eseguite analisi termogravimetriche, light scattering dinamico, potenziale Zeta, UV-Vis-NIR e analisi della misura della disperdibilità dell'acqua. Gli spettri Raman e Infrarossi sono stati registrati solo per i derivati del CNS con maggiore disperdibilità in acqua, quindi SWCNH-S, SWCNH-N, SWCNH-G, MWCNT-G e rGO-S.

1 Introduction

1.1 Regenerative medicine

Regenerative medicine is a relatively young field of medicine that combines several engineering techniques with the biology study of cells to repair diseased or damaged tissues and organs. Millions of people lose or have damage to an organ each year because of a disease or accident. In these situations, organ transplantation is the most widely recognized treatment, notwithstanding the restrictions imposed by age, compatibility, and donor availability. Therefore, regenerative medicine shows itself as a prospective substitute for transplantation because it gets around issues like the phenomenon of donor rejection or donor scarcity and incompatibility.

Tissue engineering is one area of regenerative medicine,[1] concerning the study and creation of biomaterials for the repair or regeneration of injured tissues.[2] Indeed, the field is interdisciplinary and encompasses materials science, cell biology, interactions between materials and cells, and surface characterization.[3] Creating natural or synthetic biomedical scaffolds that promote cellular adhesion, transplantation, and function is a crucial aspect of tissue engineering.[4,5]

Biopolymer-based matrices combined with biodegradable and bioactive nanofillers form nanocomposite materials, which are regarded as scaffolds that may correctly direct cellular activity and encourage the growth of new cells.[6]

1.1.1 Composite materials

The development of materials that mimic the extracellular matrix environment is essential to foster tissue growth. It is imperative that scaffolds have the appropriate composition, mechanical characteristics, and chemical stability to facilitate the replacement, repair, or rebuilding of a portion or the full tissue. Then, they must be able to promote and assist the adhesion, division, and proliferation of cells. Furthermore, the material porosity needs to be high to ensure intercellular

connections as well as the diffusion of metabolites and oxygen. Creating scaffolds that are both biologically active and have the best qualities is therefore essential to the success of tissue engineering.[7]

Composite materials are hybrid materials made up of a filler phase that serves as reinforcement and carries additional properties inside a predetermined matrix. Due to the heterogeneous nature of these materials, it can be challenging to determine the extent to which the volumes, shapes, and geometries of the various phases that make them up affect the overall properties of the materials. Polymers are the most often utilized matrices in the creation of composite materials. Instead, fillers that are more widely used include glass, Kevlar®, and carbon fibers, which are usually micrometer-sized materials. Nanocomposites, or materials with fillers that have at least one dimension smaller than 100 nm, have been developed recently. In contrast to other materials composites, nanocomposites have some intriguing characteristics.

For instance, because of their small size and porosity, the fillers have a particularly high surface area, which increases the interface between the filler and the matrix. Although uniform and well-dispersed fillers are normally necessary for materials to function as composites, this is not always the case, particularly when it comes to nanocomposites. The uniformity refers about where the reinforcer is placed within the matrix, and the dispersibility concerns the dimensions of the aggregates. It is frequently challenging to get excellent dispersions of nanofillers due to their enormous surface area.[8]

Bio-composites are generally characterized as composite materials that incorporate phases that are manufactured from natural polymers. Because these materials are easily recyclable, biodegradable, and commercially viable, they are intriguing for use in biological applications, such as tissue engineering. These are specifically described as composite materials used in biomedical scaffolds that are intended to interact with the biological environment. These scaffolds allow the cells to proliferate and create tissues with a three-dimensional structure.[9]

1.1.2 CNS in composite materials

Biomedical scaffolds containing carbon nanostructures (CNS) as fillers are showing promise in the diagnosis and treatment of medical conditions. There is a growing interest in materials based on carbon nanostructures for a range of applications, including tissue regeneration, drug delivery, and implants for doctors.

Current research[9] indicates that the mechanical, electrical, and structural qualities of carbon nanotubes (CNT) enhance some matrices in which they are incorporated. For instance, they raise the elastic modulus. Studies conducted in vitro have demonstrated that carbon nanotubes can occasionally absorb extracellular proteins, which enhance cellular connections and create scaffolds that are more biocompatible and bioactive.[9]

In the context of biomedical applications, it is imperative that the nanostructures have to be soluble in aqueous solutions to facilitate biocompatibility.

In addition to water, biological fluids can also contain chemical compounds and proteins, as well as varying pH and salt concentrations.[5,10,11] Therefore, it turns out that to make CNS dispersible in the cellular milieu in which they wish to be used, they must be sufficiently modified. Numerous investigations on embedding functionalized carbon nanotubes in matrices like collagen, L-polylactic acid (PLLA), and polycarbonate-urethane can be found in the literature.

Different nanocomposite materials have been prepared and studied in the past by Professor Enzo Menna's research group to promote the proliferation and differentiation of neural cells.

The first biocompatible scaffolds obtained in the group, using PLLA as the matrix and carbon nanotubes functionalized with p-methoxyphenyl groups as fillers, were able to encourage nerve cell attachment and differentiation.[12,13]

1.1.3 Matrices

Among the matrices that can be used to develop synthetic biomaterials hydrogels are the most popular. These are three-dimensional mesh systems composed of hydrophilic natural or synthetic polymers linked together by covalent bonds to

form chemical hydrogels or by intramolecular physical attractive forces to form physical hydrogel. Hydrogels are capable of absorbing large amounts of water or biological fluids, up to a percentage of thousands and swell without dissolving. In its “swollen” state, the hydrogel is soft and elastic, like most tissues in the human body. The high affinity of these matrices for water is due to the presence of hydrophilic components such as carboxyl, carbonyl, amino and amides distributed along the polymer chain.[3]

Hydrogels are often considered biocompatible materials also because their structure and composition have some similarities to the extracellular matrix and macromolecular components of the body. Biocompatibility is the ability of the material to be inserted in the body without damaging neighboring cells or causing a reaction that reduces the effectiveness of the desired function. In recent times, hydrogels have been widely used in many applications, including tissue engineering to be used in this field and promote new tissue formation, hydrogels must meet criteria including physical parameters related to mechanical degradation and related to biological activity such as cell adhesion and biocompatibility.[2]

The mechanical properties of mainly depend on the stiffness of the original polymer chain, the type of cross-linking, the bond density, and the swelling degree of the polymer chains.

All these factors influence cell adhesion and the design of the gel, which must create and maintain appropriate space for tissue growth. The developmental interactions between cells and hydrogels significantly influence cell adhesion, migration, and differentiation. In fact, inappropriate interactions can cause the model to form in an undesirable way.[2]

In the research group, after analyzing the rheological properties of PLLA-based scaffolds, it was found that the elastic modulus of this nanocomposite was too high compared to typical tissues of the nervous system.

Therefore, the attention was shifted to hydrogels was chosen because they have tunable and compatible rheological properties compatible with nervous tissue.[14]

1.1.4 Hydrogels

A hydrogel is defined by IUPAC as a gel in which the swelling agent is water. A gel is made up of a three-dimensional network, or matrix, of a polymeric nature which traps a large amount of solvent. Hydrogels can be classified according to different criteria. In hydrogels, the networks are generally cross-linked and they are rich in hydrophilic groups/domains.[15]

Depending on the sort of cross-linking, there are two fundamental categories: those physically cross-linked and those chemically cross-linked. A hydrogel is characterized as chemical when the cross-linking is covalent, see Figure 1: different types of hydrogels[16] These gels are exceptionally steady and mechanically solid thanks to the covalent nature of lattice interaction. In a physical or supramolecular gel, cross-linking happens by means of non-covalent, such as hydrogen bonds, ionic bonds and Van der Waals interactions. These bonds have weak and reversible nature; thus, physical gels are mechanically less strong. They have the advantage of being dynamic frameworks, besides they can be arranged without the addition of cross-linking agents which are frequently harmful to the cells, and they can have an impact on the movement of organic particles typified within the gel.

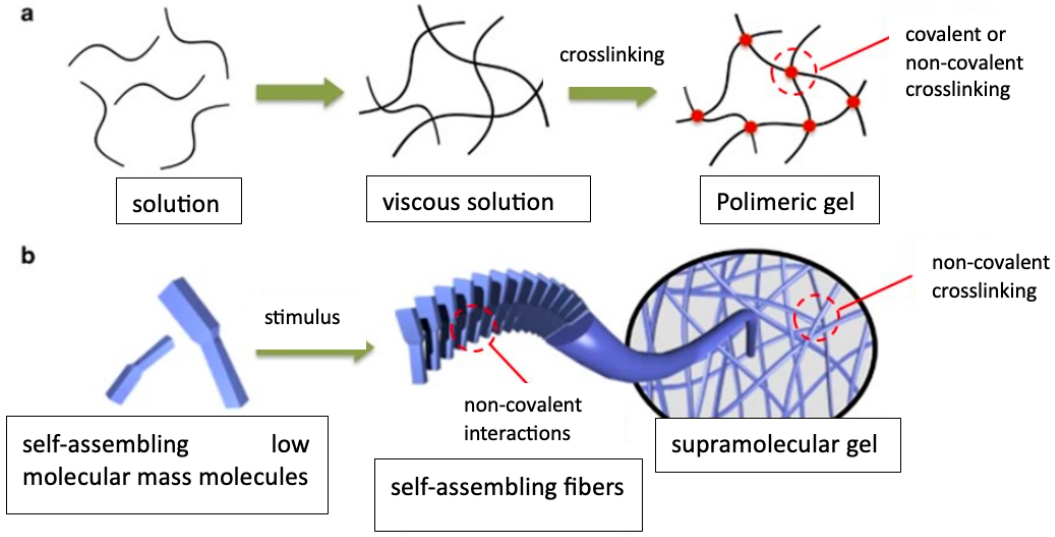

Figure 1: different types of hydrogels[16]

Hydrogels can be obtained from common polymers, in which the chain is shaped by covalently connected monomers: they constitute the classic polymeric

hydrogels. On the other hand, they can be obtained from supramolecular polymers, in which the monomers are little particles that constitute the polymer chains through a self-assembly mechanism.

Hydrogels can be classified as natural or synthetic, depending on the origin of the polymer. Synthetic polymers have a precise and conventional chemistry and their properties can be controlled.

By changing the chemical composition of the hydrogel it's possible to influence the other two parameters. There's a wide choice of materials that can frame hydrogels. Some examples are polyethylene oxide (PEO), polyethylene glycol (PEG), polyvinyl alcohol (PVA), polyacrylic acid (PAA), poly-L-lactic acid (PLLA) and peptides.[17,18] Agarose, alginate, chitosan, gelatin and hyaluronic acid are the most known natural derivatives.[19]

Biopolymer based hydrogels have also an added advantage in that these are easily degraded in an aqueous environment as well as exhibit tunable properties. These hydrogels also exhibit the ability to simulate natural tissues because of their high-water content, good biocompatibility and special surfaces properties.[15]

1.2 Carbon nanostructures

Carbon is one of the most important chemical elements especially known for its relevance for life on Earth. It's a non-metal and it represents the base of the organic chemistry. Carbon has various allotropic forms, either natural or synthetic. Allotropy is a characteristic of some chemical substances which have the property to exits in different forms constitutes from the same atomic species.

Carbon nanostructures embrace a wide variety of carbon allotropes, with many shapes and sizes, such as carbon dots, carbon nanotubes (CNT), carbon nanohorns (CNH) and reduce graphene oxide (rGO) as well as other less-explored carbon nanoforms such as graphene quantum dots, nanodiamonds, fullerenes carbon nano onions, carbon nanohorns and carbon nanotubes. In these allotropic forms carbon has a sp^3 and sp^2 hybridization and this can influence the shape of the nanostructure according to how many covalent bonds a carbon atom can handle

with. Carbon nanostructures can be classified according to the number of dimensions, which are not confined to the nano scale range (below 100 nm). This variety shown in Figure 2, stems from the carbon atom's capacity to manifest itself in several hybridization. One-dimensional structures like CNT two- or three-dimensional structures like fullerenes, and dimensionless structures like CNH can all be distinguished inside the CNS.[7]

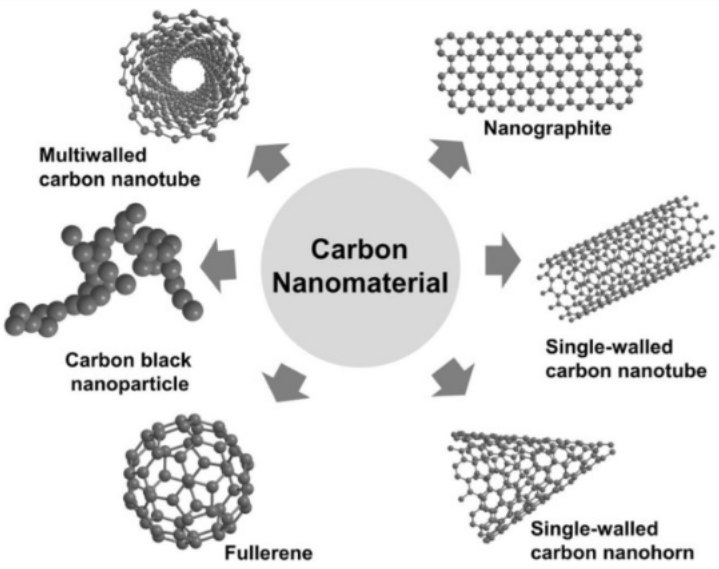

Figure 2: examples of carbon nanostructures [20]

CNS have drawn more attention in the last few decades due to their unique physical, chemical, optical, and electrical characteristics. In particular, the scientific community has shown a great deal of interest in the properties and applications of carbon nanotubes. [11] Research has recently turned its attention to the biomedical field, although previously it was centered on applications that took advantage of its physical features.[21]

1.2.1 Carbon Nanohorns

Nanohorns and their nanocomposites have been studied for several uses, such as gas absorption and transport, catalyst support, sensors, and biomedical engineering. The significant surface area of single-walled carbon nanohorns (SWCNH) is one of its most intriguing features. SWCNHs are composed of

covalently bound sp^2 hybridized carbon atoms and have a conical tip resembling a horn,[22] Figure 3. It is produced by laser ablation of pure graphite at room temperature, in a short amount of time, and with high yields all without the need for metallic catalysts.[23]

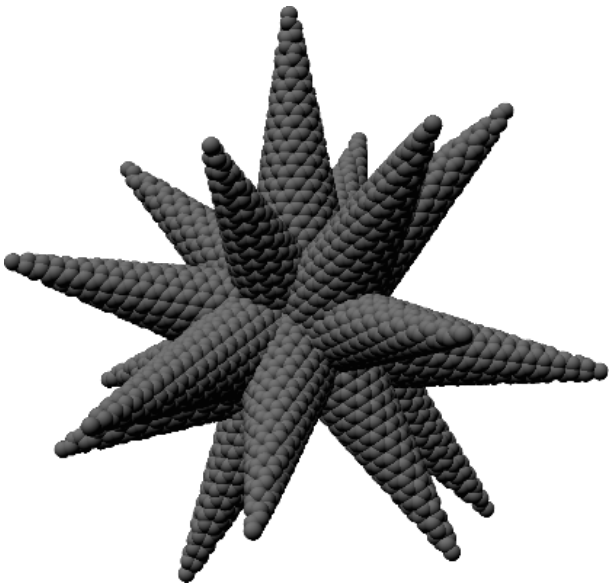

Figure 3: representation of SWCNH structure

Van der Waals-type interactions between nanohorns give rise to aggregates with a diameter of about 100 nm. Although CNH has a significant tendency to aggregate, its structural features, reactivity, and synthetic technique have made it a subject of study for a variety of applications (adsorption, drug delivery, catalyst support, solar cells, etc.).

When considered separately, SWCNHs resemble cones that are 40–50 nm long and have a diameter of 2–5 nm. They are composed of a combination of pentagons, hexagons, and heptagons from a structural perspective. The structure of a CNH is similar to the outcome of a single graphite sheet being distorted. There are three ways to go from a disk flat to a conical shape, Figure 4. In the first, a double fold is trained (a), in the second, a triangle section of the disk is removed, and the ends are reconnected (b), and in the third, the ends are cut, then folded and overlapped to form a sort of helix (c).[24]

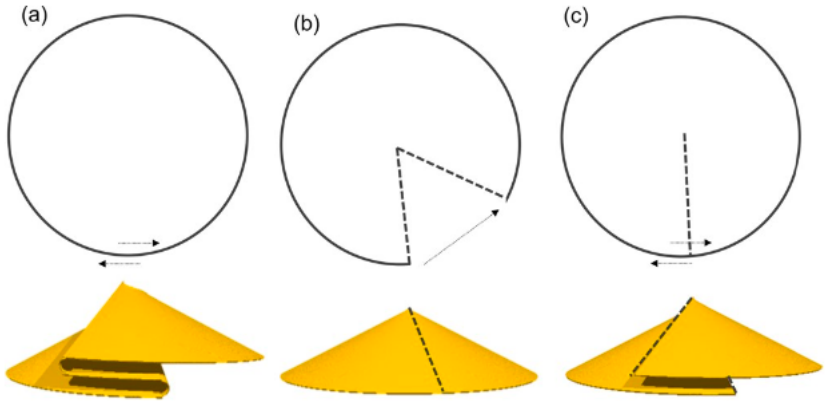

Figure 4: three common ways to obtain a conical structure starting from a flat disc: (a) double fold, (b) by removing a section and reconnecting the ends, (c) cutting and stacking out of plane to form a helical structure [24]

It is possible to create conical nanostructures with any vertex angle by using techniques (a) and (c) when applying what is shown in Figure 5 to graphene to create a SWCNH. Conversely, method (b) allows for only a finite range of vertex angles. These restrictions result from the fact that, given graphite's aromatic system, "slices" with angles of 60° (or multiples of 60°) must be removed to preserve the continuity of the bonds. Because of graphene's hexagonal shape, every removal of a triangle causes at least one pentagon to form in the direction of the nanohorn's tip.[24]

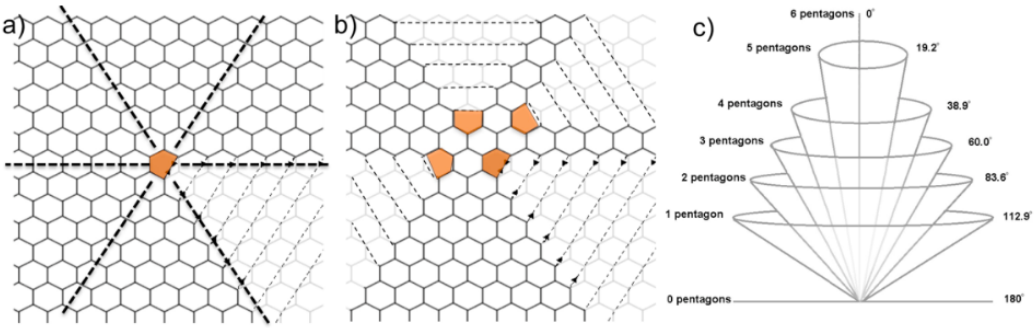

Figure 5: creation of a SWCNH from graphene through the removal of a triangular piece (shown in grey) and the creation of new connections between the ends (shown as dotted lines). Cones with one pentagon in (a), four pentagons in (b), and potential cones with their vertex angles and pentagon counts in (c) [24]

The variation in the vertex angle of SWCNH with the number of pentagons in the tip is depicted in Figure 5c. Typically, a nanohorn consists of a short, cylindrical

portion that resembles the structure of a nanotube, followed by a conical end. The tips of CNHs typically have five pentagons, but in order to keep the wall of the CNH parallel to the central axis, as occurs in CNTs, an additional pentagon needs to be positioned far from the tip, Figure 6c. Find a heptagon nearby to make up for the curvature caused by the presence of the sixth pentagon.[24]

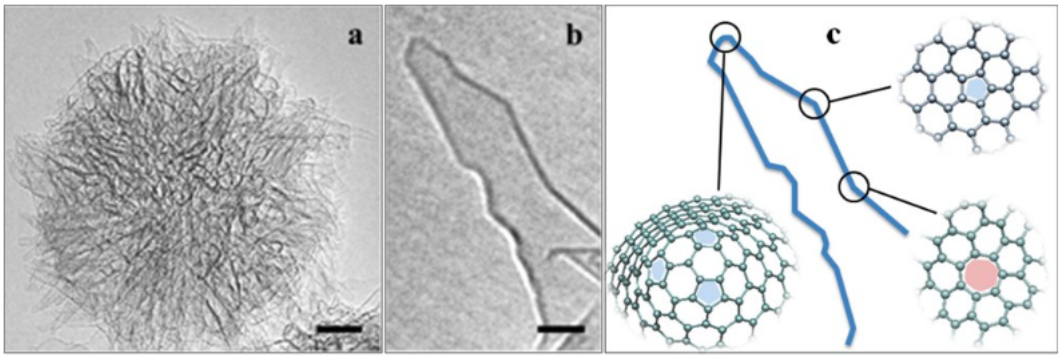

Figure 6: HRTEM images of (a) a dahlia-like CNH aggregate and (b) a single CNH. (c) Schematic representation of the typical arrangement of pentagons (blue) and heptagons (pink) [24]

The combination of these two geometries, the pentagon and the heptagon, involves a modification of the initial structure that permits the nanohorn's curvature to be retained while affecting its reactivity. Heptagons and the Pentagon are sites that are more easily targeted because they deviate from aromaticity. Because of the pyramidal distortion of the carbon bonds that are sp^2 hybridized, even the regions with significant curvature encourage localized chemical reaction. As a result, in the case of CNH, the chemical reactivity is mostly restricted in the vicinity of the tip and the flaws. Chemical functionalization is a primary method of altering the surface of CNH by incorporating inorganic molecules, ions, or particles. Chemically altering CNH can lead to new discoveries in the field of materials science research and increase its solubility in water, which is a crucial need for applications in the biological sciences. There are two main ways to introduce chemical modifications on CNH: either by non-covalently assembling molecules functional through π-π stacking, electrostatic interaction, or immobilization of inorganic particles, or by covalently attacking organic molecules by forming stable bonds in the external wall.[24]

Covalent functionalizations can be further classified into two groups: direct insertion of functional groups into the CNH wall and oxidation of conical ends, which results in the introduction of oxidized species (mostly carboxyl groups) that can undergo further chemical changes.[25]

1.2.2 Carbon Nanotubes

Carbon nanotubes are especially well-suited for neural applications of this kind. This propensity is brought about by their large surface area, significant mechanical and electrical characteristics, and inherent ability to promote neuronal cell attachment. The remarkable potential of the carbon surface of nanotubes as a biocompatible substrate that neurons can adhere to has been validated by recent investigations. This affinity appears to be closely related to surface characteristics including charge, polarity, and roughness.[26]

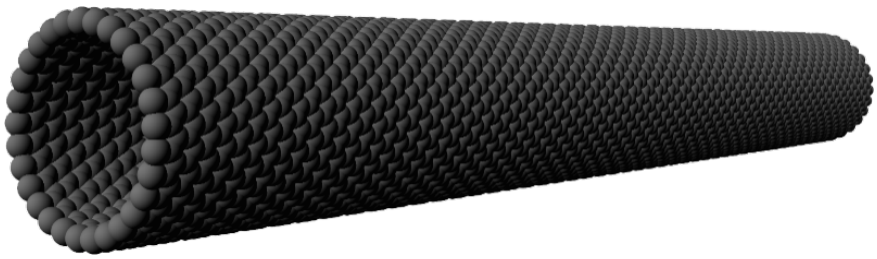

Figure 7: schematic representation of SWCNT structure

Figure 8: schematic representation of MWCNT structure

CNT are made completely of covalent connections between carbon atoms that have undergone sp^2 hybridization. They resemble cylindrical structures composed of rolled graphene sheets, with diameters perhaps in the range of nanometers. A single carbon nanotube typically has at least one closed end and a hemispherical structure resembling that of fullerene.[26] There are two types of CNT: single-walled (SWCNT), Figure 7 and multi-walled (MWCNT), Figure 8, depending on the manufacturing procedure. The former is composed of a single rolled sheet of graphene is used, whereas in the latter, two or more sheets are coaxially wrapped around an empty cylinder. Van der Waals forces sustain this kind of structure between neighboring layers.[27]

Despite having a basic binding system and a chemical makeup like other nanomaterials, carbon nanotubes exhibit tremendous structural heterogeneity and linkage between structure and characteristics. You can modify the qualities and structural features of CNT by adjusting the synthesis methods. However, achieving the desired features in CNT synthesis necessitates extraordinary control over atomic rearrangement. CNTs are primarily synthesized via arc-discharge (AD), chemical vapor deposition (CVD), and laser ablation (LA).[27]

The first two are distinguished by the vaporization of carbon at high temperatures (thousands of degrees Celsius) and the use of solid-state carbon sources as precursors for plant growth nanotubes. In contrast, CVD produces CNT at relatively low temperatures (500–1000 °C) by utilizing metal catalyst particles as "seeds" in addition to using gaseous hydrocarbons as a carbon source.

Even though the precise growth mechanism of carbon nanotubes (CNTs) is unknown, researchers are constantly looking for new synthesis techniques to produce CNTs with lower defect levels and higher yields.

The CVD method was employed to obtain the MWCNTs used in this thesis work.

Chair, zigzag, and chiral ellipticities are the three possible CNT configurations based on the "rolling angle" of the graphite sheets. The chiral vector defines the chirality of the single nanotube:

$$C_h = na_1 + ma_2$$

Equation 1

where the coefficients along the hexagonal lattice's vectors a_1 and a_2 are represented by the numbers n and m. There are three different orientations that carbon atoms can take on around the circumference of a carbon nanotube (CNT) using this scheme, which is described as (n, m). The values n and m determine chirality: if n = m, we talk about "chair" nanotubes; if m = 0, we talk about "zigzag" nanotubes; and in all other circumstances, where n ≠ m, we talk about "chiral" nanotubes, Figure 9.

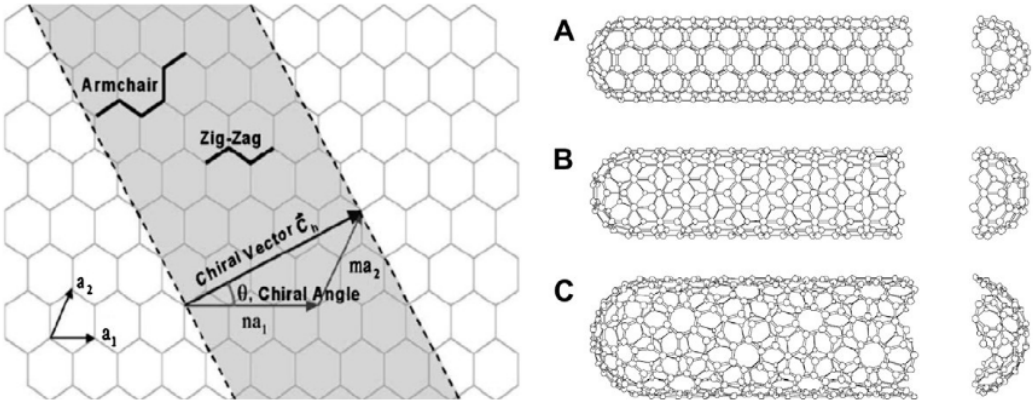

Figure 9: representation of a hexagonal lattice of a single layer graphene and CNS profiles within different ellipticity [27]

The characteristics of CNT, especially the electrical ones, are greatly influenced by its ellipticity: a nanotube is classified as metallic if (2n + m) is a multiple of three, and as semiconductor if it is not. However, because each MWCNT is made up of several graphene sheets, each of which may have a different ellipticity, it is difficult to determine the electrical properties.[28]

Ideally, pure carbon nanotubes are insoluble in all organic solvents and aqueous solutions. They can be sonicated into dispersion in certain solvents, but if the process is stopped, they precipitate. Chemical treatment is required to produce the most soluble CNTs for integration into biological, organic, or inorganic systems. Three main methods exist for modifying these one-dimensional CNS: (a) covalent functional group attachment via reactions to the π-conjugated bond skeleton; (b) noncovalent molecular absorption or capture on the CNT surface; and (c) filling the internal cavity.[29]

MWCNT were chemically altered in this thesis project in accordance with approach (a). It is helpful to separate the CNT structure into two regions: sidewall and part terminal, to better explain chemical reactivity. In fact, the end of a SWCNT (5,5) on Figure 10c resembles a fullerene C60. The latter has a structure akin to the hemisphere of a fullerene.

Therefore, it is vital to discuss the reactivity of fullerenes and the structural elements that affect it to comprehend the reactivity of CNT.

The primary factor influencing the reactivity of fullerenes is the high bond tension caused by their spherical geometry, which is represented by the carbon atoms' pyramiding angle (θ_p). The angle between the carbon atom's orbital π and the nearby σ bond, from which one subtracts a 90° contribution, is known as the corner of pyramidalization Figure 10b. The carbon atoms that have undergone sp2 hybridization tend to form contacts with other atoms in a planar trigonal geometry, implying pyramiding angles of θp = 0°.

Alternatively, carbon atoms sp^3 hybridized, assuming a tetrahedral shape with θp = 19.5°. All carbon atoms (sp^2) in the C60 fullerene have θp = 11.6°, meaning that the geometry of their bonds is more tetrahedral than trigonal planar. This explains why the addition processes that turn trivalent carbons into tetravalent carbons are preferred in fullerenes. Therefore, regardless of the diameter of the carbon nanotube, the terminal part of a single-walled or multiple-walled carbon nanotube is always more reactive than the lateral wall.[29]

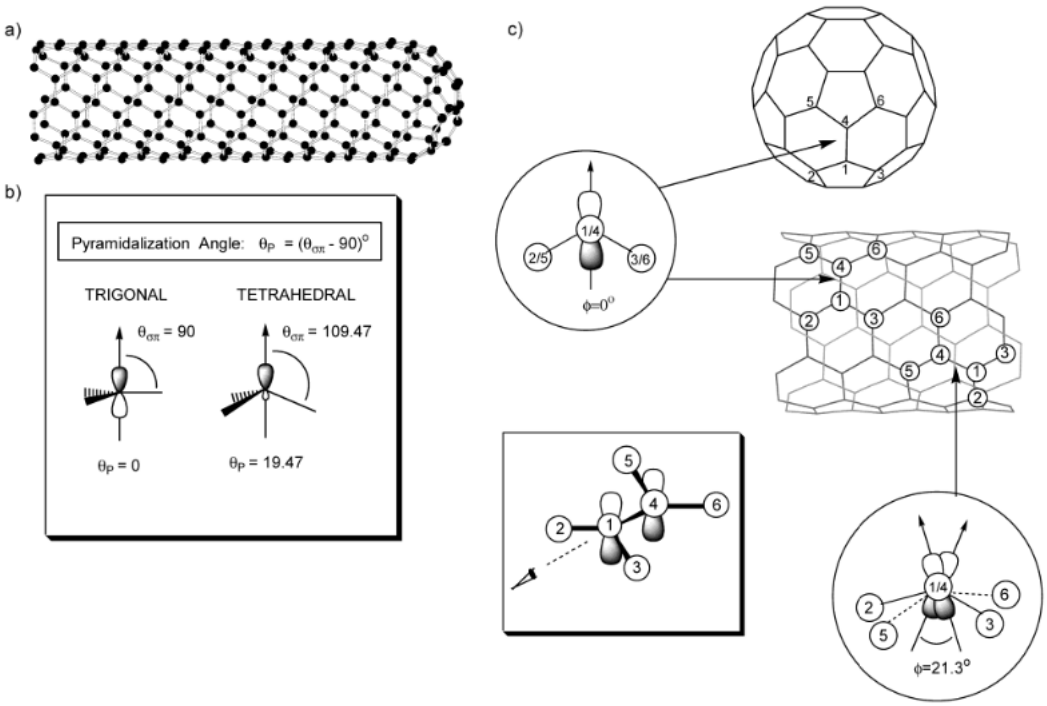

Figure 10: (a) SWCNT (b) pyramiding angle and (c) misalignment angle of the π orbitals along the C1-C4 covalent bond in the C60 fullerene and in the SWCNT [30]

Because a perfect CNT only consists of covalent connections between carbon atoms, it is thought to be chemically inert, Figure 10a. Perfect CNTs are devoid of

defects and functional groups. Nonetheless, a local tension created by the misalignment of the carbon atoms' π orbitals, and the curvature brought about by pyramidalization makes CNTs more reactive than a graphene sheet.[30]

Upon examining the structure of a carbon nanotube on Figure 10c, we observe that, despite the identical atoms that make it up, two kinds of bonds can be identified: those that run perpendicular to the nanotube's axis or parallel to its circumference, like C4-C6, and those that form an angle with the circumference, like C1-C4.

The carbon atoms in the π orbitals of these bonds are exactly overlapped in the first example, but there is a detectable phase shift between the two orbitals in the C1-C4 bond due to the misalignment angle (φ). In moles, the π orbital alignment is nearly flawless, in contrast to nanotubes. Features that affect the nanostructure's reactivity include misalignment and pyramiding angles, which vary inversely with the diameter of the CNTs.[3031]

1.2.3 Reduced Graphene Oxide

Graphene is an allotrope of carbon in which each atom bonds to three adjacent atoms to form a honeycomb network the thickness of a single atom, a peculiarity that makes it in effect a two-dimensional crystal, [32] Figure 11.

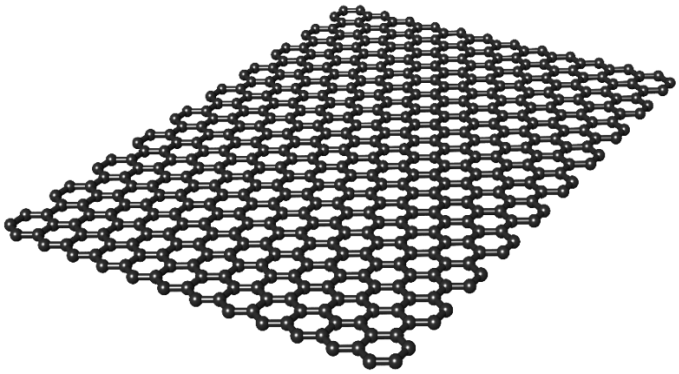

Figure 11: schematic representation of rGO structure

The crystalline lattice of graphene has a hexagonal honeycomb structure, in which each atom is able to bond to three adjacent atoms, placed at 120° from each other, with an interatomic distance d = 1.42 Å and center-to-center distance of 2.46 Å, see Figure 12. To illustrate the crystalline lattice of graphene some mathematical-geometric tools that help us describe the spatial arrangement of atoms in crystalline solids are needed.

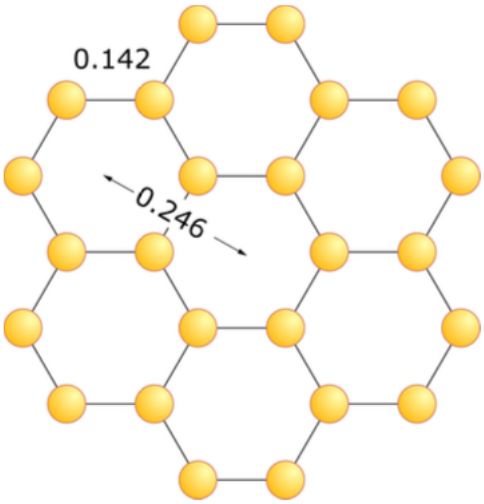

Figure 12: honeycomb crystalline lattice. Each carbon atom has three bonds to adjacent atoms, with a bond length of d = 1.42 Å. These hexagons, like those of the benzene molecule, have a center-to-center distance of 2.46 Å [32]

Graphene is pretty transparent, retaining around 2.3% of unmistakable light. Its thermal conductivity, k, is measured with an esteem of ≈ 5000 $W \cdot mK^{-1}$ for a single-layer sheet at room temperature.[33] Graphene moreover has fabulous mechanical quality. The inherent mechanical properties of free-standing monolayer graphene films were measured by nano-indentation in atomic force microscope.[34] The breaking quality was found to be 42 N m^{-1} and the Young's modulus 1.0 TPa, demonstrating is one of the most grounded materials ever measured.[35]

There are many graphene-based materials that have been synthesized and studied: graphene oxide, reduced graphene oxide, ultrafine graphite, graphite ribbons and graphene dots. Wick et al. showed an interesting representation of graphene-based materials according to tree fundamental properties: average lateral dimension, carbon/oxygen atomic ratio and the number of graphene layers, Figure 13.

In this work of thesis rGO is functionalized. It is a derivative of graphene oxide (GO) that has undergone a reduction process to remove a major part of the oxygen-containing functional groups present in GO. This reduction process can be achieved through various methods, including thermal treatment or chemical reduction using agents like hydrazine or ascorbic acid. rGO retains some of the structural features of graphene, but it typically has a lower degree of oxidation compared to GO. This results in improved electrical conductivity and mechanical properties, making RGO more similar to graphene while still containing some residual functional groups that can affect its properties and interactions in biological applications. [36]

The properties of rGO depend on the method of reduction used, the extent of reduction, and the presence of impurities. These factors influence its potential applications in fields such as electronics, energy storage, and biomedical engineering.[36]

rGO can contain nitrogen (N) atoms, particularly if it is synthesized using chemical reduction methods that introduce nitrogen atoms during the reduction process.

For example, reducing GO with hydrazine can lead to nitrogen doping in the RGO structure. This doping can enhance certain properties of rGO, such as its electrical conductivity and electrochemical performance, making it suitable for various applications, including sensors and energy storage devices.[36] However, the presence of nitrogen in rGO is not guaranteed and depends on the specific reduction method used and the conditions under which the reduction occurs. The extent of nitrogen incorporation can vary, and it is important to characterize the resulting material to understand its composition and properties.[36]

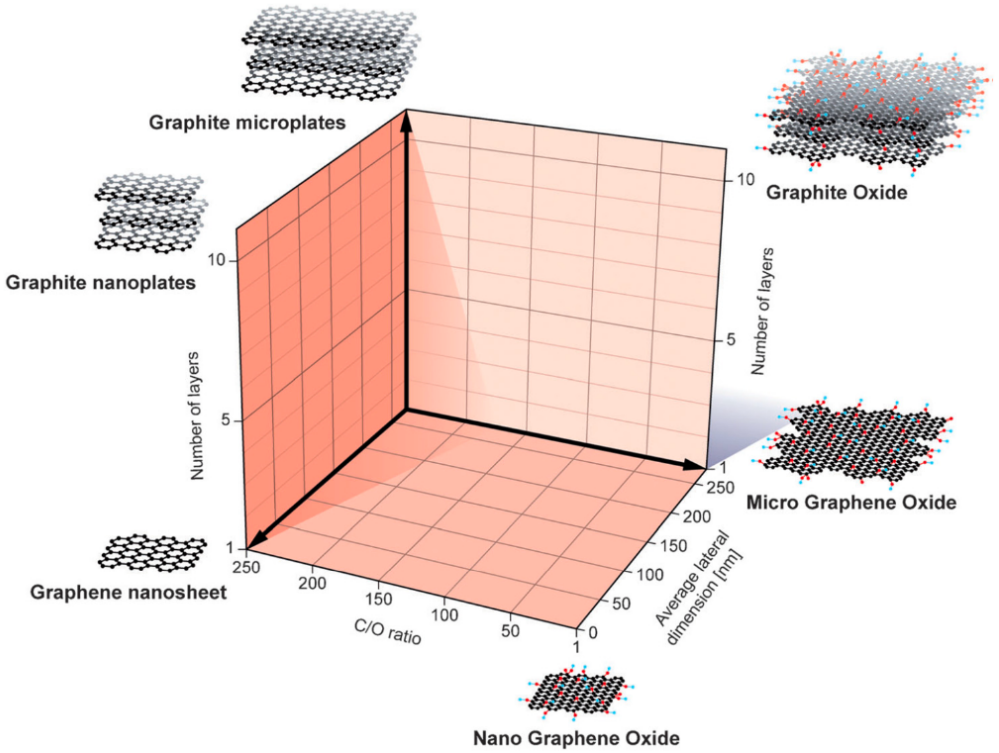

Figure 13: representation of graphene-based materials proposed by Wick et al. [37]

The C/O ratio is considered as a useful trait since the family of graphene-based materials incorporates materials with broadly variable surface oxygen substance. Depending on how they are prepared, these materials can have immensely diverse chemical structures and properties. Many of the pristine graphene properties come from quantum effects, which are the most prominent when single atomic

layers are present. Thus, preventing aggregation and restacking to form a graphitic structure is the main challenge when working with this material. The low-yield production techniques such as mechanical exfoliation, liquid exfoliation, epitaxial growth and chemical vapor deposition limit the studies using pristine graphene. These methods result in monolayers of the material on a substrate (≈ 0.8 mg/m^2) or in diluted suspensions (≈ 0.01 mg/mL). Liquid exfoliation involves sonication of graphite in the presence of a solvent such as N-methyl-pyrrolidone. The resulting suspension is a mixture of single, few, and multilayered graphene sheets. For the CVD technique, a gaseous carbonaceous precursor like methane is flowed at high temperatures around 1000 °C over a metal substrate which can be copper or nickel. Reduced graphene oxide has been the most promising approach for bulk production of graphene materials. With this technique, graphite is first oxidized using strong oxidants and intercalating compounds. Graphite oxide can be exfoliated in water through ultrasonic agitation, producing stable suspension of GO, which can then undergo reduction by chemical, electrochemical, thermal means.[38] The resulting reduced graphene oxide (rGO) has intermediate structure and properties somewhere along the spectrum between graphene oxide and pristine graphene, depending on the degree of reduction and the starting structure of the graphene oxide, Figure 14.

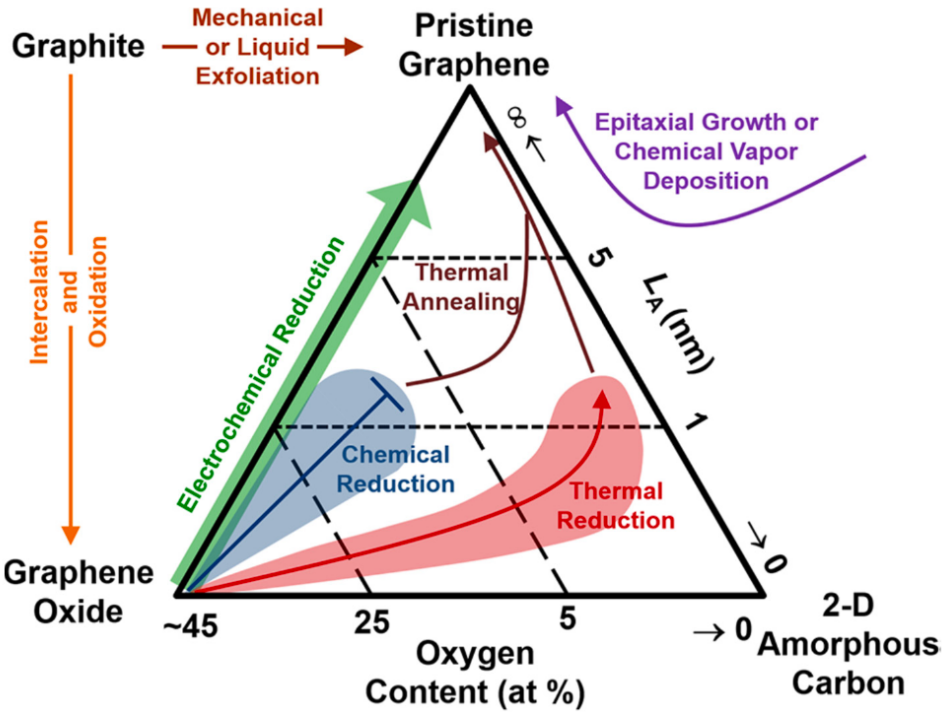

Figure 14: different production methods for graphene-based materials [38]

1.2.4 Reactivity of carbon nanostructures

For an extended period, the insolubility and incompatibility of carbon nanostructures with polymers have hindered their usage as fillers in composite materials. Functionalization significantly reduces the propensity for the normal aggregation of CNS and increases their solubility in organic solvents or water. It is important to emphasize that the filtration and dispersion preparation processes have a significant impact on the solubility values of the nanostructures. To enable consistent comparisons and assessments, it is crucial to specify the methodology followed in the determination process when providing solubility data.

Approaches that forecast the filling of the cavity or the covalent or non-covalent functionalization covalent, along the walls, at the ends, or at the structural defects can generally be used to modify CNS. Oxidation is one of the most researched strategies for molecular attachment to the CNS surface.[39] Sadly, this process produces highly defective nanostructures, which drastically changes their mechanical and electrical characteristics. Altering the CNS wall chemically is a less

important and aggressive strategy that is consequently preferable in situations when, for example, it is desired to preserve the CNT's electrical properties.[39]

The coupling with diazonium salts, or "Tour reaction," is one of the most crucial synthetic techniques for the chemical alteration of the CNS surface.[40]

Through the Tour reaction, all the synthesized compounds used in this thesis work were acquired to change carbon nanostructures.

1.2.5 Tour reaction

Carbon nanostructures can be functionalized in a cost-effective way by using the diazonium chemistry.

Diazonium chemistry is a flexible, scalable, and inexpensive method of functionalizing carbon nanostructures to produce soluble nanomaterials with some of the greatest functionalization levels ever achieved.

The most widely accepted synthetic route is based on the Gomberg-Bachmann mechanism, which is still up for debate but states that the reaction happens when an electron is transferred from the nanostructure to the diazonium salt, releasing N_2 and creating a reactive aryl radical that can attach to the nanostructure wall to form a covalent bond. Tour and his associates made a significant contribution to the creation of an easy, quick, and convenient method for obtaining highly functionalized and soluble CNTs. They showed that p-substituted anilines treated with isopentylnitrite might produce diazonium salts that could be used to functionalize carbon nanostructures, see Figure 15. This kind of method eliminates the need to separate and store potentially explosive aryl, photosensitive, and diazonium salts. It is widely acknowledged that the reductive dissociation of the diazonium salt, which results in the loss of N_2 and the creation of an aryl radical that has the potential to attack a carbon-carbon double bond, is the first step in the dinitrogenation reaction.

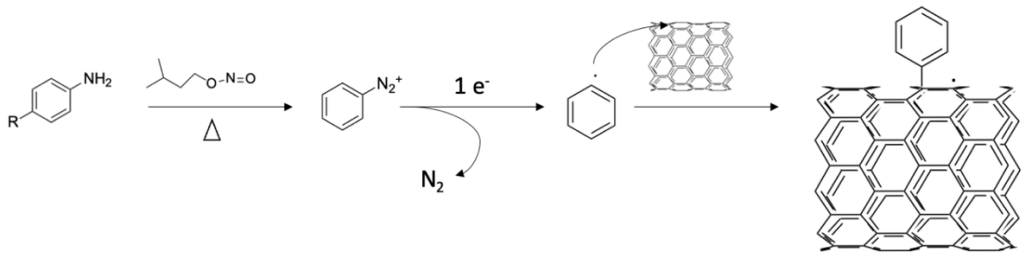

Figure 15: radical mechanism of Tour reaction with diazonium salts generated in situ

This technique produces highly functionalized and valued nanotubes with solubility among the highest reported in the literature, perhaps because the species radicals involved are very reactive. It has recently been attempted to demonstrate that diazonium chemistry may also be applied to various carbon allotropes.[41,42]

1.3 Characterizations

1.3.1 Thermogravimetric analysis (TGA)

TGA is a fundamental technique used for studying thermal properties of nanostructures; it consists of monitoring the change in mass of a sample which is heated in a controlled manner, modulating the time, the temperature and the atmosphere which can be oxidizing or inert. They analysis returns the thermogram, which is the representation of the percent mass decay of the sample versus the temperature, as shown in

Figure *16*. Mass losses can be attributed to phenomena of evaporation, decomposition and oxidation (in this case the process occurs in air). The CNS are characterized by a high thermal stability that derives from their composition and structure which make them refractory to decomposition in general up to approximately 700 °C. In the case of the CNS are functionalized it is possible to observe losses in the sample mass at lower temperatures and which may be associated with decomposition of molecules bound to the surface.

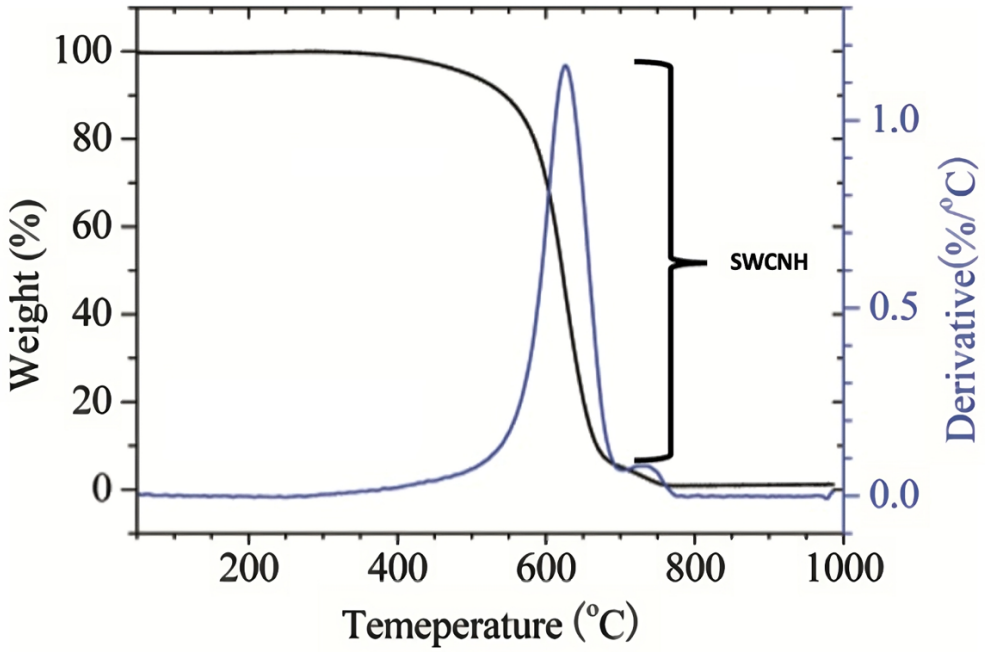

Figure 16: example of thermogram of pristine SWCNH [43]

The analyzer usually consists of a high-precision balance with a pan loaded and a furnace. The loss of mass is recorded as a function of the high temperature. To be able to interpret data, a computer is connected to TGA instrument. The sample is suspended into a platinum pan which is hanging on a hook located above the furnace, Figure 17.

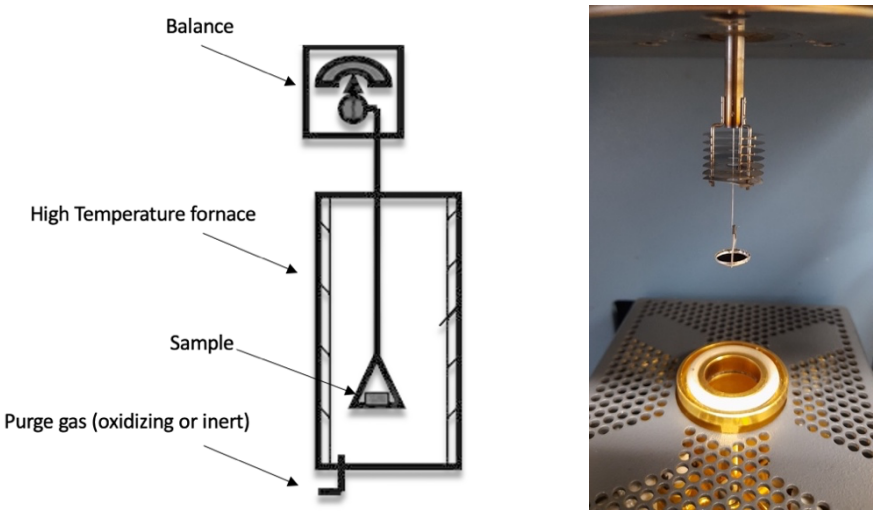

Figure 17: scheme of the TGA instrument

By analyzing the two main mass losses, it is possible to calculate the degree of functionalization (FD) of nanostructures through the relationship between the number of moles of functional group (nFG) and the number of moles of carbon (nC) present in the sample.

$$FD = \frac{n_{FG}}{n_C}$$

Equation 2

The number of moles of the functional group is calculated as the ratio between the mass loss attributed to the decomposition of the functional group (FG) and its molecular mass (MM_{FG}). The temperature range in which the degradation of FG is observed goes from 100 °C to approximately 640 °C for SWCNH. Similarly, n_c is given by the ratio between the residual mass of the sample at the temperature at which the functional group degradation ends (T_{FG}) and the atomic mass of carbon (MM_C):

$$n_{FG} = \frac{(M_{150\,°C} - M_{TFG})}{MM_{FG}}$$

Equation 3

$$n_C = \frac{M_{TFG}}{MM_C}$$

Equation 4

1.3.2 UV-Vis-NIR Spectroscopy

The UV-Vis-NIR absorption measurement is conducted over a range of very broad wavelengths ranging from 400 nm to 2500 nm. The spectrum of absorption of carbon nanostructures is characterized by a linear region, called plasmonic, relating to the absorption of electrons delocalized of sp^2 carbons. Given the natural tendency of the nanostructures of carbon to aggregate, it is very likely that in the

analyzed solution there are aggregates of comparable size or sometimes greater than wavelength of the incident radiation, causing Mie scattering phenomena.
UV-Vis-NIR measurements therefore measure the attenuation of light given by sum of two contributions: the absorption of the individual CNS and the scattering of the radiation incident on the surface of the aggregates. In case the f-CNS are well dispersed in the solvent, it is possible to correlate the absorbance of the sample at its concentration through the Lambert-Beer law:

$$A = \varepsilon \cdot C \cdot l$$

Equation 5

In which A stays for absorbance of the sample, C for the concentration of the sample [$mg \cdot mL^{-1}$], ε is the molar extinction coefficient [$mL \cdot mg^{-1} \cdot cm^{-1}$] and l represent the length of the optical path [cm]. The value of ε is not determined given the inhomogeneous nature of carbon nanostructures.[44]

1.3.3 Dynamic Light Scattering (DLS)

The hydrodynamic radius value of nanoparticles distributed in solution is obtained using the DLS approach. The hydrodynamic radius is equal to the radius of a fictitious hard sphere that diffuses at the same speed as the particle under study when subjected to DLS, Figure 18.

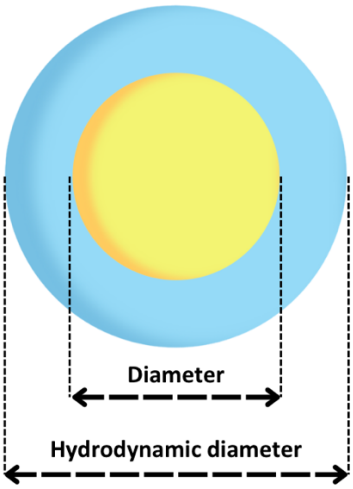

Figure 18: Comparison between the diameter of a spherical particle and its hydrodynamic diameter

Using a mathematical model, the device links the intensity of light scattered by the nanoparticles with the sample's diffusion coefficient. The Stokes-Einstein equation is then used to get the value of the hydrodynamic radius:

$$D = \frac{k_b T}{6\pi\eta R_H}$$

Equation 6

where D is the diffusion coefficient, kb the Boltzmann constant, η la viscosity of the sample and R_H the hydrodynamic radius of the spherical particle.

1.3.4 Zeta Potential (ZP)

The measurement of Zeta potential is also based on the scattering of light. When a charged particle is in a dispersing medium, to which it comes when an electric field is applied, it moves towards the sign electrode opposite (electrophoresis). When a charged particle, for instance, has 20 negative charges, a diffuse layer containing both positive and negative particles forms beyond the Stern layer, which is located close to the particle's surface and contains a large number of ions with opposite charges. The total of the diffuse layer and the Stern layer is referred

to as a double layer electric. The interface between the moving particle and the medium dispersant during electrophoresis is referred to as the slip plane,

Figure 19. During this process, the particles with their double electrical layer migrate in the direction of the opposite electrode. The potential at the slip plane is known as the Zeta potential. levels less than -30 mV and greater than 30 mV are often regarded as high Zeta potential levels.[45,46]

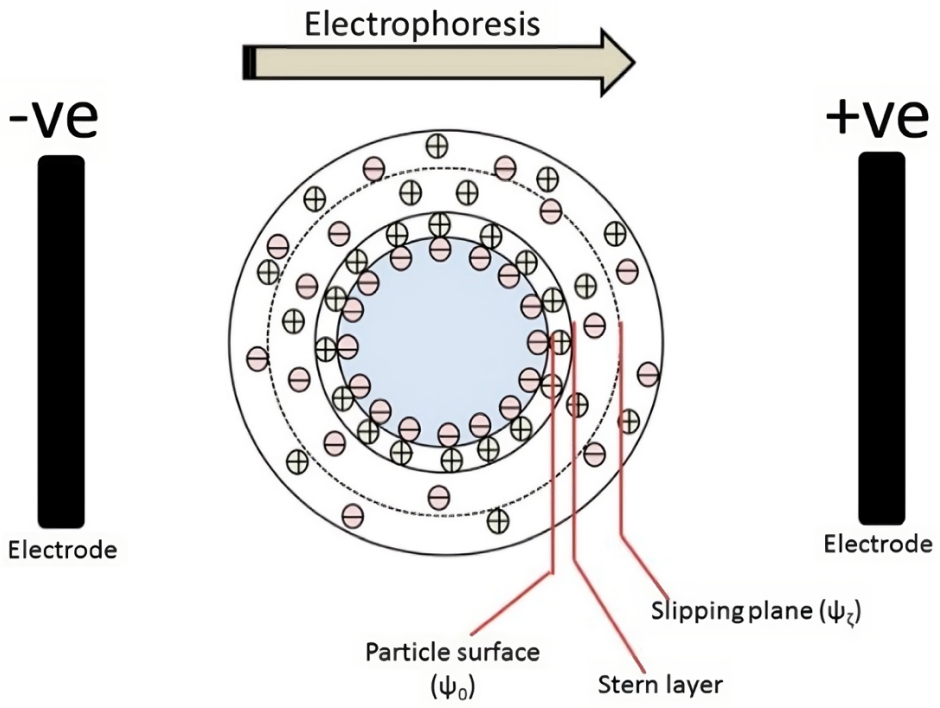

Figure 19: representation of the double electric layer of a negative particle [45]

1.3.5 Raman spectroscopy

Raman spectroscopy is a commonly used technique in chemistry. The vibrational information provides a very specific fingerprint of the chemical bonds in the molecule. In Raman spectroscopy a vibrational transition is considered active if it causes a deviation of the polarizability of the molecule.

The device consists of three components: laser source, sample illumination system and spectrophotometer.[47]

The widely used Raman source is a helium/neon laser operating in continuous mode at 50 mW power. Laser radiation is often generated at a wavelength of 633.0 nm, like in this work. When higher sensitivity is required, argon ion lasers with lines at wavelengths of 488 and 514 nm are also used. The region of organic molecules commonly studied is from 500 to 2000 cm^{-1}.[47]

Raman spectroscopy on carbon nanotubes

The Raman spectrum of carbon nanotubes provides a lot of information about the structure and properties of nanostructures derivatives. Each part of the Raman spectrum, the radial breathing mode (RBM), the disruptive mode (D mode), and the tangential mode (G mode), can be used to access other properties together. The radial breathing mode (RBM) occurs in the range from 120 to 250 cm^{-1}.[47]
This corresponds to the atomic vibration of the C atom in the radial direction, as if the nanostructures were breathing,[48] Figure 20.

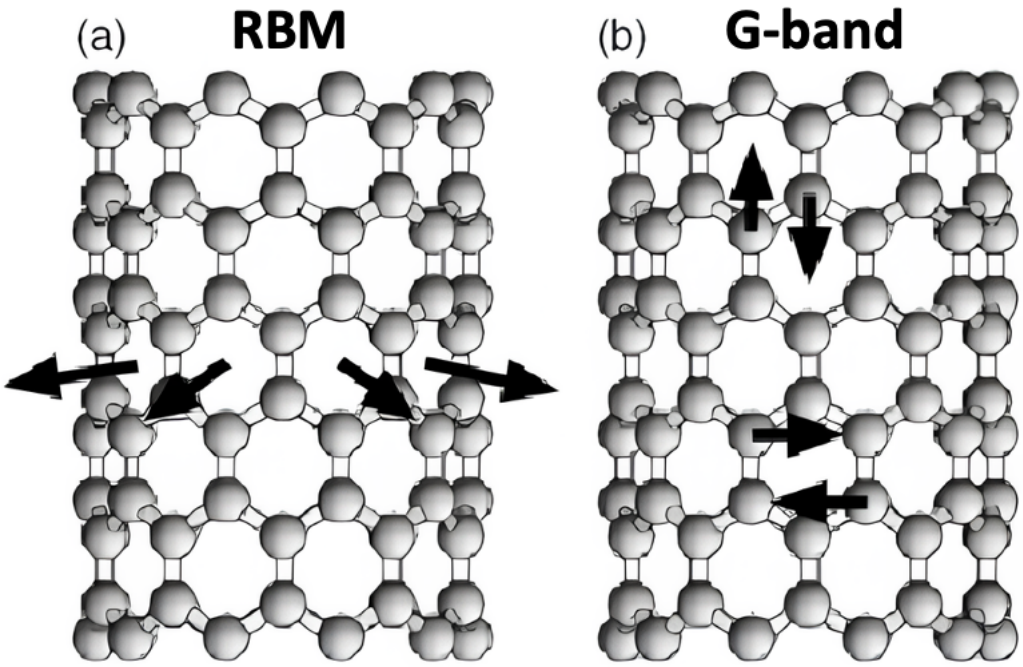

Figure 20: schematic picture showing the atomic vibrations for (a) the RBM and (b) the G band modes [49]

The frequency of the radial breathing mode can be used to determine the diameter of the nanostructure. In fact, the Raman shift of a RBM mode is proportional to

the inverse of the nanotube diameter. For tubes with large diameters (> 2 nm), the RBM characteristic intensity is weak and difficult to observe.

The observation of characteristic multi-peak features around 1580 cm^{-1} (G band) also provides a signature of carbon nanotubes. Spectra in this frequency range can be used to characterize SWCNT, independently of RBM observations.

These multiple peak features can also be used to characterize the diameter, although the information obtained is less precise than the RBM feature. The G band also provides information about the metallic properties of SWNTs resonating with a given laser line. In fact, Raman scattering can distinguish between metallic and semiconductor nanotubes.

Finally, observation of the peak around 1450 cm^{-1} disorder-induced D band can be used to identify defects structural defects. Additionally, it can be used to monitor the functionalization process that converts sp^2 sites into sp^3 sites. In our study, all Raman spectra were normalized to G-band and D-band intensities before and after the reaction is compared.[49]

The I_D/I_G ratio for CNT is a critical parameter used to assess the level of disorder in the material. In the context of MWCNT the I_D band is associated with defects and disorder, while the I_G band is related to the graphitic structure.[47] The I_D/I_G ratio can vary based on several factors:

- Disorder level: a higher I_D/I_G ratio indicates more disorder within the CNT. Conversely, a lower ratio suggests a more ordered structure.[47]
- Effects of laser power and ion irradiation: the I_D/I_G ratio decreases with increasing laser power density and also varies with ion irradiation, where it decreases at low ion influence and increases at high ion flux.[47]
- Correlation with wall number: the intensity ratios of the G' and G bands are correlated with the number of walls in the carbon nanotubes, indicating that the the I_D/I_G ratio can also provide insights into the structural characteristics of the nanotubes.[47]

In summary, the I_D/I_G ratio is a valuable metric for evaluating the structural integrity and disorder of CNT with specific values depending on the experimental conditions and the nature of the samples being analyzed.[47]

Raman spectroscopy on graphene

Graphene, a two-dimensional carbon allotrope composed of a single layer of carbon atoms arranged in a hexagonal lattice, exhibits unique Raman spectra due to its sp^2 hybridization and phonon dispersion characteristics. The utility of Raman techniques lies in the ability to differentiate single, double, and triple-layer graphene. In other words, Raman techniques can determine layer thickness at atomic layer resolution for graphene layer thicknesses of less than four layers [50]. The Raman spectrum of graphene typically consists of several prominent peaks:

- G peak (Graphitic peak): this peak arises from the in-plane vibrational mode of sp^2 hybridized carbon atoms which constitute the graphene layer. It is located around 1587 cm^{-1} and is associated with the integrity of the graphene lattice [50]
- 2D peak (Double resonance peak): the 2D peak is a second-order Raman scattering process and represents a two-phonon process involving two in-plane phonons. It is sensitive to the number of graphene layers and is typically observed around 2700-2900 cm^{-1} [51]
- D peak (Defect peak): the D peak, located around 1350 cm^{-1}, arises due to defects, disorder, or structural imperfections in the graphene lattice, such as vacancies, edges, or grain boundaries. It is associated with the breathing mode of sp^2 carbon atoms and indicates the presence of disorder-induced phonon scattering [51]

All these bands are shown in Figure 21.

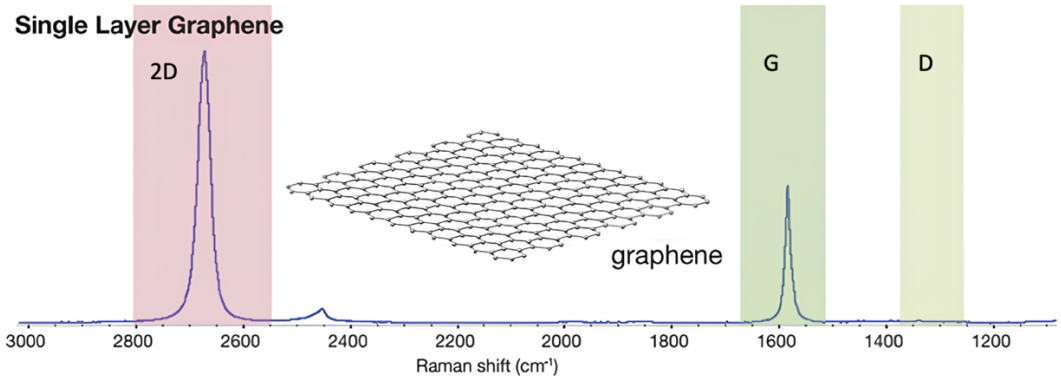

Figure 21: Raman spectrum of angle layer graphene collected with 532 nm excitation [50]

Raman spectroscopy provides insights into the structural quality, doping level, strain, and functionalization of graphene, making it an indispensable tool for graphene characterization and quality control.

The ratio I_{2D}/I_G of these bands for high quality or defect-free, single layer graphene will be seen to be equal to two, Figure 22. This ratio or lack of a D-band with a sharp symmetric 2D-band is often used to confirm a high-quality, defect-free graphene sample.[50]

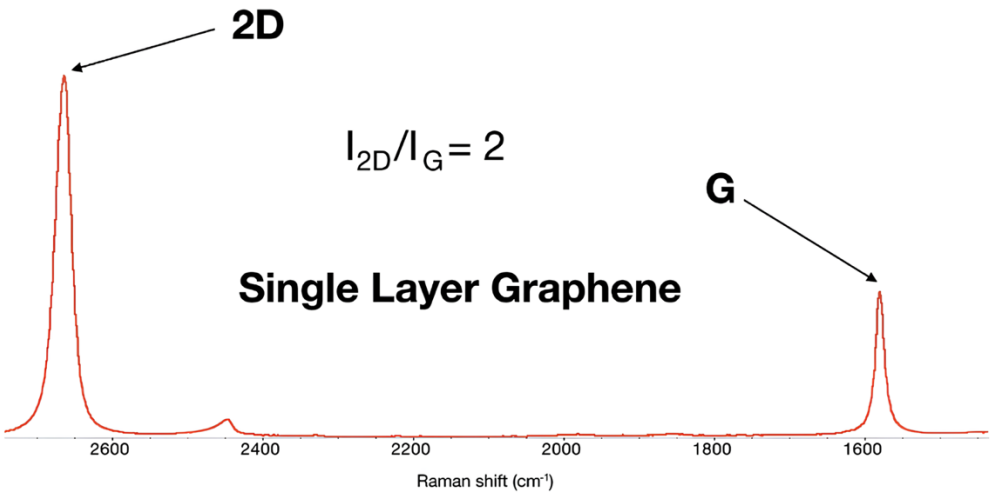

Figure 22: single layer graphene identification by the intensity ratio of the 2D-band to G-band [50]

Raman spectroscopy on carbon nanohorns

Raman spectroscopy is a valuable technique for characterizing carbon nanohorns (CNH), which are a unique class of carbon nanomaterials with horn-shaped structures composed of graphene sheets rolled into a tubular morphology. Raman

spectroscopy provides insights into the structural, electronic, and vibrational properties of CNH, offering valuable information for their characterization and applications.[47]

When applied to CNH, Raman spectroscopy typically reveals several characteristic peaks:

- G peak (Graphitic peak): similar to graphene, the G peak in CNH arises from the in-plane vibrational mode of sp^2 hybridized carbon atoms and represents the E_2g phonon mode. It is typically observed around 1587 cm^{-1} and provides information about the graphitic nature and integrity of CNHs.
- G’ peak (also known as the 2D peak) in the Raman spectra of SWCNH is an important feature for characterizing these materials. This peak is the result of a second-order Raman process and typically appears around 2600-2700 cm^{-1}. The G' peak provides insight into the electronic and structural properties of SWCNH. For instance, doping with elements like nitrogen or boron can shift the position and alter the intensity of the G' peak, indicating changes in the electronic environment and structural integrity of the SWCNH.
- D peak (Defect peak): the D peak, located around 1350 cm^{-1}, is associated with defects, disorder, or structural imperfections in CNH, such as vacancies, edges, or curvature-induced strain. It indicates the presence of disorder-induced phonon scattering and provides insights into the quality and structural defects of CNH.
- D' peak (Doubly-resonant D peak): similar to graphene, the D' peak, located around 1620 cm^{-1}, may be observed in CNHs, particularly in highly-defective or functionalized samples. It is associated with the overtones of the D peak and provides additional information about defect-induced vibrational modes.

CNHs may exhibit additional Raman peaks corresponding to different vibrational modes and structural features. These peaks can provide further insights into the unique properties and characteristics of CNH.[47]

Raman spectroscopy allows researchers to study the quality, purity, defect density, doping level, and functionalization of CNH, as well as their structural transformations under different processing conditions. It is also useful for investigating the interactions between CNH and other materials in composite systems or device applications.

The common Raman bands of CNH are shown in Figure 23. The spectrum shows two main bands at 1588 and 1313 cm^{-1}, which can be assigned to G and D modes, respectively. The G band comes from the intrinsic properties of a graphite sheet. For graphite, the band is observed at 1582 cm^{-1}, which is a slightly lower value than for SWCNH; nevertheless, for carbon nanotubes (CNT), the G mode is observed at 1590 cm^{-1}. A defect-induced D band in SWCNH results from the two topological distortions: layer folding and pentagon carbon rings in a conical SWCNH structure.[52] The D band is dependent on the excitation energy.[52]

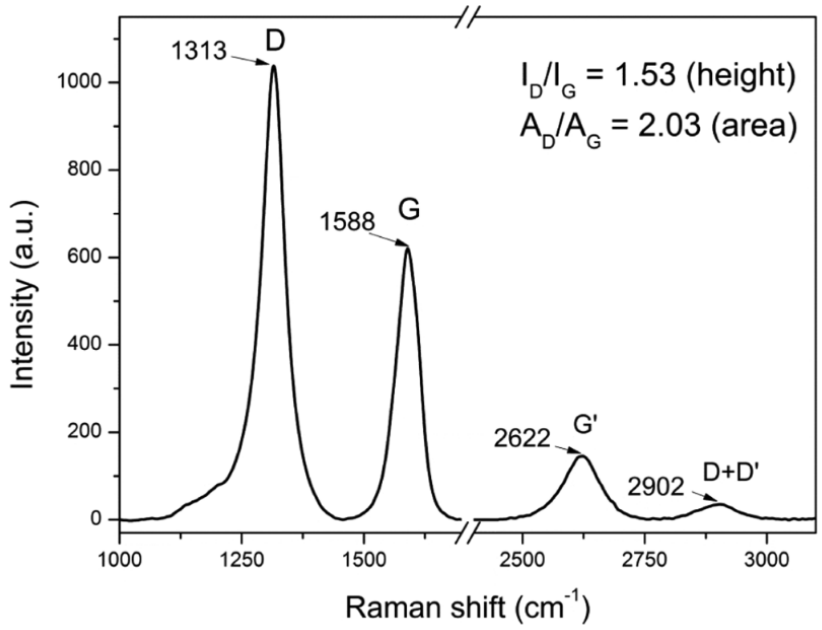

Figure 23: Raman spectrum of SWCNH, excitation length 633 nm [52]

1.3.6 FT-IR spectroscopy

Fourier Transform Infrared Spectroscopy (FT-IR) is a powerful analytical technique widely employed in the characterization of carbon nanostructures. From pristine graphene to complex carbon nanotubes and nanohorns derivatives, FT-IR offers valuable insights into their structural properties, surface functionalization, and chemical composition.[53]

At its core, FT-IR operates by measuring the absorption of infrared radiation by a material. Carbon nanostructures exhibit unique infrared spectra due to the vibrational modes of their constituent atoms. In the case of graphene-based materials, these spectra are dominated by the stretching and bending vibrations of carbon-carbon (C-C) bonds, as well as functional groups attached to the surface.

One of the primary applications of FT-IR in carbon nanostructure analysis is the identification of functional groups. By comparing the spectra of pristine and modified carbon nanomaterials, researchers can detect changes in peak positions and intensities, indicating the presence of specific chemical moieties. For instance, the appearance of peaks associated with oxygen-containing groups (such as hydroxyl, carbonyl, and carboxyl) suggests successful oxidation or functionalization of graphene or carbon nanotubes.[53]

Moreover, FT-IR provides crucial information about the degree of structural disorder in carbon nanostructures. The intensity ratio of the D-band (associated with defects and disorder) to the G-band (related to graphitic sp^2 carbon) in the Raman spectrum is often used as a measure of structural integrity. FT-IR complements this analysis by offering insights into the chemical nature of defects, such as edge functionalization or vacancies, which can manifest as additional peaks or shifts in the infrared spectrum.

Another significant application of FT-IR in carbon nanostructure research is the investigation of intermolecular interactions and composite formation. By examining changes in infrared spectra upon the incorporation of carbon nanomaterials into polymer matrices or hybrid structures, researchers can elucidate bonding mechanisms and assess the compatibility of components. This

information is crucial for the design and optimization of carbon-based nanocomposites with tailored mechanical, electrical, and thermal properties.

In an FT-IR experiment on functionalized CNS, a sample containing dispersed CNS or a thin film is typically prepared and placed in the path of an infrared beam. The FT-IR instrument measures the absorbance or transmittance of infrared radiation across a range of wavelengths. The resulting spectrum provides a fingerprint of the functional groups present in the sample, based on the characteristic vibrations of chemical bonds.[54]

Key features of the FT-IR spectrum of functionalized carbon nanotubes include:

- functional group identification: peaks corresponding to stretching and bending vibrations of functional groups attached to the CNS surface are observed in the spectrum. Common functional groups introduced during modification processes include carboxyl (-COOH), hydroxyl (-OH), amine (-NH_2), and carbonyl (-C=O) groups. These peaks provide direct evidence of chemical modifications and can be used to assess the success of functionalization reactions.
- degree of functionalization: the relative intensities of peaks associated with different functional groups can provide insights into the degree of functionalization of CNS. Higher intensities of peaks corresponding to specific functional groups indicate greater levels of surface modification.
- surface chemistry: changes in peak positions and intensities compared to pristine CNS can reveal alterations in the surface chemistry of functionalized nanotubes. These changes may result from covalent or non-covalent interactions between the CNS and functionalizing agents.
- structural integrity: analysis of the FT-IR spectrum can also provide information about the structural integrity of CNS. For example, shifts in the intensity ratio of the D-band to the G-band, as observed in Raman spectroscopy, may indicate changes in the sp^2/sp^3 carbon ratio due to functionalization processes.

In summary, FT-IR spectroscopy plays a vital role in the comprehensive characterization of CNS, offering valuable insights into their chemical composition, structural integrity, and functionalization. By leveraging the unique infrared signatures of carbon-based materials, researchers can advance our understanding of their properties and pave the way for their diverse applications in fields ranging from electronics and energy storage to biomedicine and environmental remediation.

FT-IR applied to CNT

Fourier Transform Infrared Spectroscopy (FT-IR) is a versatile analytical technique commonly employed in the characterization of f-CNT providing valuable insights into their chemical composition, surface modifications, and structural integrity.[54]

FT-IR spectroscopy is a powerful tool to characterize nanotubes thanks to the specific absorption bands they exhibit in that range (600-2500 nm, that is about 16000-3400 cm^{-1}), because of electronic transition between semiconducting or metallic bands,[54] Figure 24.

Functionalized CNT, which involve the introduction of various chemical moieties onto the nanotube surface, exhibit distinct infrared spectra that reflect the presence of functional groups and the degree of modification. FT-IR spectroscopy is particularly well-suited for probing these functional groups, as they exhibit characteristic vibrational modes in the infrared region.[55]

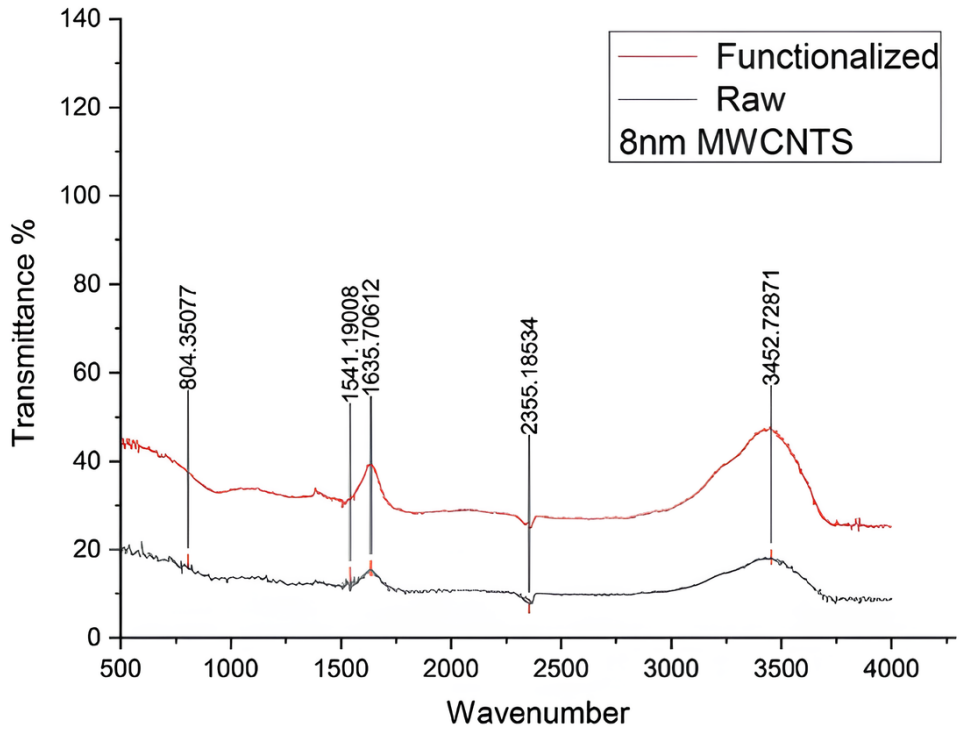

Figure 24: example of FT-IR spectrum on pristine MWCNT and MWCNT derivative [56]

By leveraging the unique infrared signatures of functionalized carbon nanotubes, FT-IR spectroscopy enables researchers to gain comprehensive insights into their chemical structure, surface properties, and degree of modification. This information is crucial for tailoring the properties of CNT for a wide range of applications, including nanocomposites, sensors, drug delivery systems, and nanoelectronics.[56]

FT-IR applied to rGO

Fourier Transform Infrared Spectroscopy (FT-IR) is a versatile analytical technique widely employed in the characterization of functionalized rGO, offering valuable insights into its chemical structure, surface functional groups, and degree of oxidation.

FT-IR spectroscopy is particularly well-suited for probing the presence of hydroxyl (-OH), epoxy (-O), and carboxyl (-COOH) functional groups, as they exhibit distinct vibrational modes in the infrared region.[53]

Peaks corresponding to stretching and bending vibrations of -OH, -O, and -COOH groups are prominent in the spectrum. For example, the broad band around 3400-3200 cm^{-1} is attributed to O-H stretching vibrations, while peaks at around 1050-1250 cm^{-1} correspond to C-O stretching vibrations. The degree of oxidation of graphene can be estimated from the relative intensities of peaks associated with different functional groups can be used to estimate the degree of oxidation in rGO. Higher intensities of carboxyl (-COOH) and carbonyl (-C=O) peaks, for instance, suggest increased oxidation levels,[57] Figure 25.

FT-IR spectroscopy is also valuable for monitoring chemical modifications and surface functionalization of rGO. Additional peaks or shifts in existing peaks may appear in the spectrum upon the introduction of new functional groups or chemical reactions with the rGO surface.

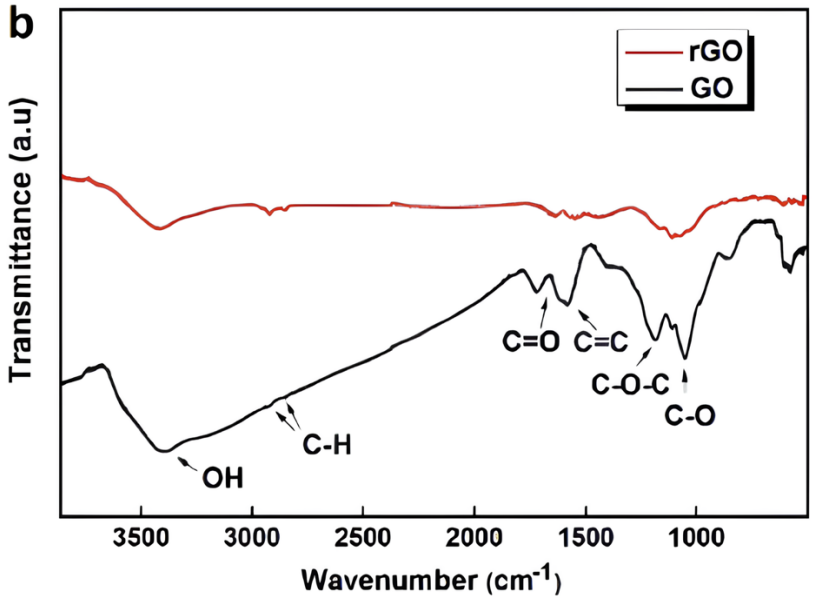

Figure 25: example of FT-IR spectrum of reduced graphene oxide [57]

FT-IR applied to CNH

FT-IR spectroscopy is a powerful analytical tool extensively utilized for characterizing CNH offering valuable insights into their chemical composition, surface modifications, and structural properties.

Functionalized CNHs, which involve the introduction of various chemical groups onto the nanohorn surface, exhibit unique infrared spectra reflecting the presence of functional groups and the extent of modification. FT-IR spectroscopy is particularly suitable for probing these functional groups as they exhibit characteristic vibrational modes in the infrared region.[58]

In an FT-IR analysis of functionalized CNHs, a sample containing dispersed nanohorns or a thin film is typically prepared and exposed to an infrared beam. The FT-IR instrument then measures the absorbance or transmittance of infrared radiation across a range of wavelengths. The resulting spectrum provides a distinctive fingerprint of the functional groups present in the sample, based on the characteristic vibrations of chemical bonds, Figure 26.

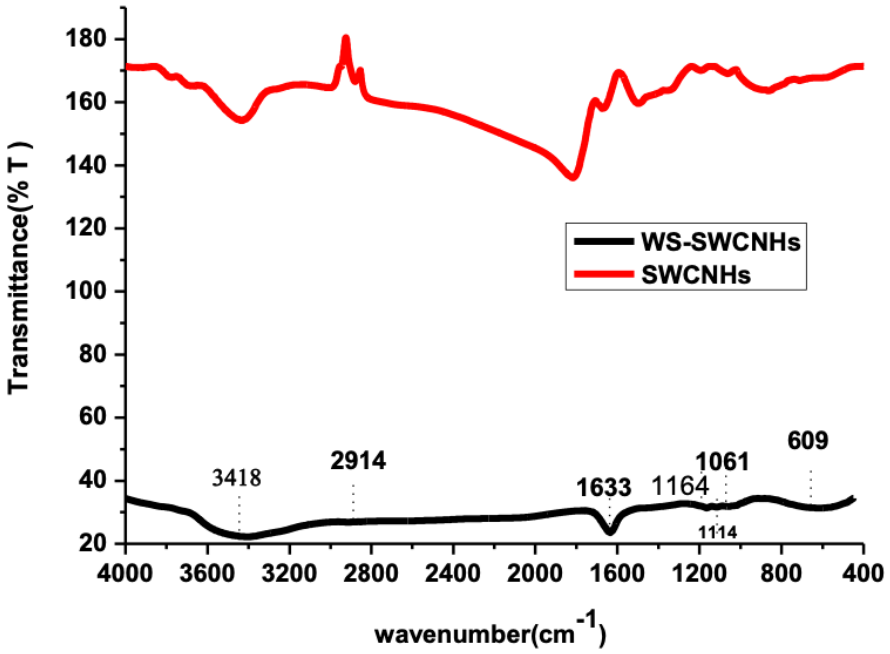

Figure 26: example of FT-IR spectrum on pristine SWCNH and water-soluble (WS) SWCNH derivative [58,59]

1.4 Aim of the thesis

The purpose of this thesis work is to synthesize and characterize specifically derivatives of carbon nanostructures that could be used in the future as fillers in composite materials and examine their characteristics considering potential uses

in the biomedical field. The goal is to synthesize derivatives of SWCNH (f-SWCNH), MWCNT (f-MWCNT) and rGO (f-rGO) with distinct functional groups to assess the impact of functionalization on the behavior of nanostructures, specifically their water dispersibility.

The generated nanocomposite materials will be used in futures as scaffolds to study proliferation and differentiation of different cell lines, in particular related to the central nervous system. The functional groups' characteristics specifically, their electrostatic charge, could regulate not just the solubility of the nanostructures but also their impact on adhesion, mechanical qualities, cell development, and differentiation. For instance, it is not completely ruled out that surface charge may affect the nanostructure's toxicity, growth, and cellular differentiation. Appearance is mostly dependent on the state of aggregation and interactions with proteins and cell membranes. Considering this, further research will expand the investigation to include other carbon nanostructures derivatives.

2 Results and discussion

2.1 General strategy for the functionalization of carbon nanostructures

Pristine carbon nanostructures are subjected to strong aggregation because of extensive Van der Waals attraction and π-π stacking between sp^2 hybridized carbon surfaces. This behavior limits the possibility of using these materials in the field of biology and exploiting properties such as high surface area.

Chemically modifying the CNS involves the introduction of functional groups which can establish electrostatic repulsive interactions between the CNS and/or attractive interactions with the solvent, such as hydrogen bonding or dipole interactions.

The presence of one or both factors limit the aggregation tendency of the nanostructure and promotes its dispersibility. To obtain water-soluble CNS derivatives, the CNS were functionalized with benzensulfonate (S), methylsulfonylbenzene (MeS), N-(p-aminobenzoyl)glycine (G) and trimethylbenzenammonium (N) groups by Tour reaction, Figure 27, starting from the following aniline precursors: sodium sulfanilate dihydrate, 4-(methylsulfonyl) aniline, aminohippuric acid and 4-amino-N, N, N-trimethylbenzenammonium iodide, respectively.

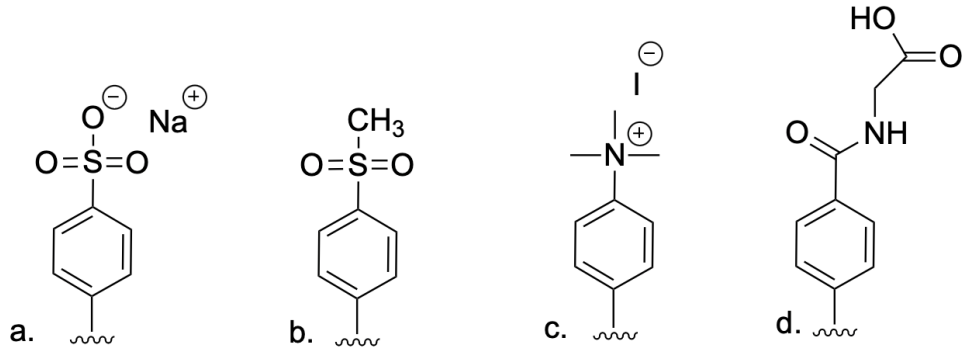

Figure 27: functional groups grafted on the carbon nanostructures. (a)-benzensulfonate, (b)-methylsulfonylonbenzene, (c) -trimethylbenzenammonium and (d)-N-(p-aminobenzoyl) glycine

The reactions were performed in water, for derivatives functionalized with benzensulfonate, N-benzoylglycine and trimethylbenzenammonium, and in 1-cyclohexyl-2-pyrrolidone (CHP) for derivatives functionalized with methylsulfonibenzene.

Other derivatives of CNS bearing benzene sulfonate groups have been previously synthesized in the research group.[60] Among the advantages of this functional group, good solubility in water of the aniline precursor and its simple manipulation can be mentioned. The stability of the negative charge is one of the factors that makes benzensulfonate interesting for this work of thesis.

Considering the remarkable fact of the acidity of benzenesulfonic acid (pKa = -6.65), the benzenesulfonate group retains its deprotonated form over the wide pH range and especially under physiological conditions (pH = 7.53-7.45).[61]

Data collected in previous research demonstrate that the benzene sulfonate group promotes the disentanglement of MWCNT and CNH agglomerates, making the nanostructure dispersible in water in the form of almost individual particles.[62]

With the prospect of using carbon nanostructures as fillers in composite scaffolds for cell growth, they were decorated with both neutral and charged groups. In fact, several studies have shown that the type and charge density on the surface of nanotubes can influence the material's interaction with cells.[63]

In recent years, introducing positive charge onto the surface of the scaffold for cell growth has become increasingly interesting, especially for applications in the field of neurons. In fact, several studies have demonstrated that when neurons grow in the presence of positive charges, longer axons with more complex branching are observed. As has been reported for the benzene sulfonate group, it is important that the positively charged derivatives are also stable in biological media and maintain their charge under physiological pH conditions.

Therefore, it was chosen to functionalize MWCNT and SWCNH with the quaternary ammonium group that was previously used in the research group: trimethylbenzammonium.[14]

While the other anilines are commercially available, the aniline precursor (4-N, N, N- trimethylbenzenammonium iodide), N, N-dimethylbenzene-1,4-diamine was obtained through the following multistep synthesis.

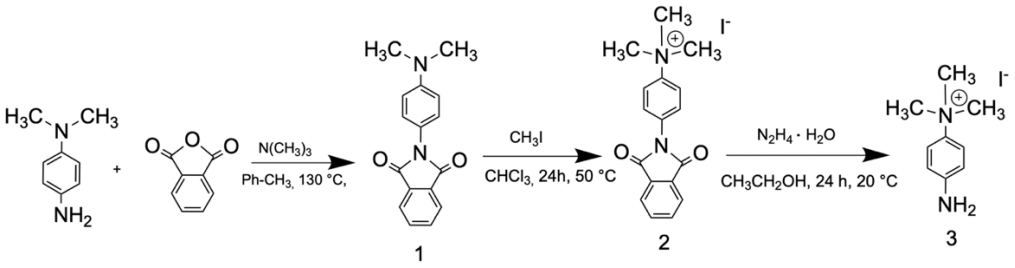

Figure 28: reaction scheme of the synthesis of 4-N, N, N- trimethylbenzenammonium iodide with reagents and conditions

The reaction scheme is shown in Figure 28. The first step (1) involves protecting the primary amine with phthalic anhydride via nucleophilic attack of nitrogen on the carbonyl carbon to form an amide bond. Therefore, methyl iodide can react selectively with the tertiary amine to form a quaternary ammonium salt (2) and finally, phthalic anhydride was removed by reduction of with hydrazine, thereby liberating the primary amine (3).

2.2 Approaches for the characterization of functionalized carbon nanostructures

To study the properties of f-MWCNT, f-rGO and f-SWCNH derivatives, a series of characterizations commonly used in the field of carbon nanostructures were performed.

Since these are not molecules but materials that are heterogeneous in shape, structure and size, evaluating the results can be complex and often requires a comparative approach.

In this work, the following characterizations were performed: TGA analysis to study thermal degradation, water dispersion measurement, UV-Vis-NIR absorption spectroscopy, DLS experiment to estimate the size of the aggregates as well as their distribution, Zeta potential measurements, FT-IR spectroscopy, and Raman spectroscopy.

TGA analyses were performed on solid samples in nitrogen atmosphere to obtain the mass loss percentage and decomposition properties of the nanostructure, especially the organic component associated with it, avoiding contributions related to material oxidation.

All other characterizations were performed in solutions to obtain aqueous extracts of the synthetic derivatives. The meaning of “extract” stays for an aqueous dispersion containing the soluble portion of each derivative, obtained by a specific procedure based on sonication, centrifugation and filtration processes.

To obtain comparable results in the thesis and previous work, which was carried out with the same procedure, the only precaution applied was the use of different centrifugation speed values for f-SWCNH, f-MWCNT and f-rGO, based on their tendency to stay dispersed in water (see sections 3.2.10, 3.2.11, 3.2.12).

Therefore, results can be compared among derivatives obtained from the same CNS but not between derivatives of different CNS.

For each derivative, a known amount of extract was placed in a TGA pan and it was evaporated using the instrument at controlled temperature, and the mass of the dry product was measured and used to calculate the concentration of the extract in mg/mL.

This concentration value was defined as the "dispersibility" of the carbon nanostructure derivative in water since the concept of solubility for molecular systems cannot be strictly applied.

UV-Vis-NIR spectroscopy is a technique that can provide information on the aggregation state of nanostructured derivatives.[64]

In this study, the “operating absorbance” is defined as the value of absorbance at 1000 nm of solutions obtained by diluting each extract in different concentration depending on the type of CNS derivative. Indeed, the absorbance at 1000 nm is expected to arise only from the nanostructure, without contributions from the introduced functional groups. Unlike molecular systems in dilute solutions, a linear dependence of absorbance on concentration cannot be strictly assumed for nanostructures.[64] Therefore, UV Vis-NIR spectroscopy was not used to determine

the absolute concentration of CNS derivatives, but only to compare the dispersion of CNS derivatives with different functionalizations.

CNS are characterized by a shape that is significantly different from a spherical one. As a result, DLS measurements cannot provide the hydrodynamic radius of individual nanostructures and the Stokes-Einstein equation cannot be rigorously applied.

However, if the CNH, rGO and CNT aggregates are considered, they can be compared to an overall spherical structure. Therefore, DLS analysis can be used to roughly estimate the mean hydrodynamic diameter of f- CNS aggregates.

The values obtained for the different derivatives allow to compare the size of the aggregates and their distribution in the dispersion at list among different derivatives of the same CNS.

The polydispersion index (PdI), related to measurements of the average hydrodynamic diameter, is a value that helps estimate the heterogeneity of the sample in terms of recorded hydrodynamic diameter. Polydispersity can be due to the size distribution of aggregates in the sample or agglomeration of the sample during analysis.

Zeta potential (ZP) measurement provides a surface potential that can reveal the nature of the surface charge (positive or negative) of the f-CNS. This hypothesis is based on the fact that the charge component of the sliding plane is similar to the charge component of the f-CNS surface.[45]

Raman spectroscopy is a powerful analytical tool widely used for characterizing carbon nanostructures and their derivatives. Here's an overview of its application in this field. Raman spectroscopy is based on inelastic scattering of light, known as Raman scattering. Raman spectroscopy is non-destructive, making it ideal for analyzing delicate nanostructures. It provides detailed information about the molecular composition and structure. High spatial resolution allows for the analysis of individual nanostructures.[51]

Raman spectroscopy is a critical technique for the analysis and characterization of carbon nanostructures and their derivatives, offering insights into their structural

and electronic properties and aiding in the development of applications in nanotechnology and materials science.[47]

FT-IR spectroscopy is another valuable analytical technique used to study carbon nanostructures and their derivatives, such as graphene, carbon nanotubes, and graphene. IR spectroscopy provides information about the vibrational modes of molecules, which can be used to understand their chemical composition, bonding, and structural properties.

IR spectroscopy complements Raman spectroscopy, as some vibrational modes that are IR active may be Raman inactive and vice versa. This complementary nature provides a more comprehensive understanding of the material.

Recent advancements in FT-IR spectroscopy, such as Fourier-transform infrared (FTIR) spectroscopy and near-field infrared spectroscopy, have enhanced its sensitivity and spatial resolution. These advancements allow for better characterization of carbon nanostructures at the nanoscale.

FT-IR spectroscopy is a valuable tool for the study and application of carbon nanostructures and their derivatives, providing essential insights into their chemical composition and functionalization.

2.3 Synthesis and characterization of single wall carbon nanohorns derivatives

Before proceeding with the Tour reaction, pristine SWCNH provided by Carbonium s.r.l. company were subjected to a thermogravimetric analysis that showed a loss of mass of 6.2 %, between 150 – 400 °C, probably due to a relevant amount of impurities. After considering washing procedures based on different solvents (deionized water, diethyl ether, methanol, dichloromethane and alkaline water), acetone was found to give the best results (details reported in the experimental part).

Indeed, TGA analysis, show a decrease of mass loss percentage from 6.2 % to 4.2 % after washing with acetone, Figure 29. Probably the organic and carbonaceous

impurities were more soluble in acetone than in the other solvents. Therefore, all pristine SWCNH was washed with acetone before functionalization.

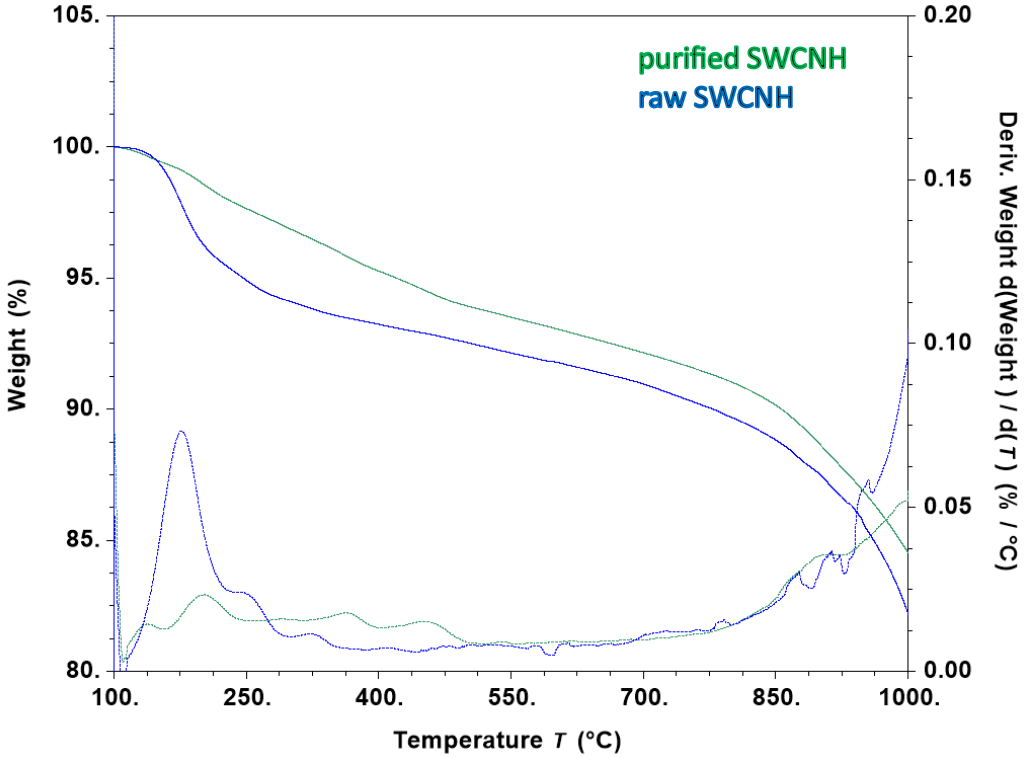

Figure 29: comparison between thermograms of SWCNH before and after washing with acetone

SWCNH were functionalized with the four functional groups discussed above and shown in Figure 27, to obtain the following derivatives: SWCNH-S, SWCNH-N, SWCNH-MeS and SWCNH-G.

The functionalization was achieved through a Tour reaction strategy, using a molar ratio of 1:1:1 between SWCNH (moles of carbon), each aniline and isopentylnitrite. All the reaction schemes are reported in Figure 30.

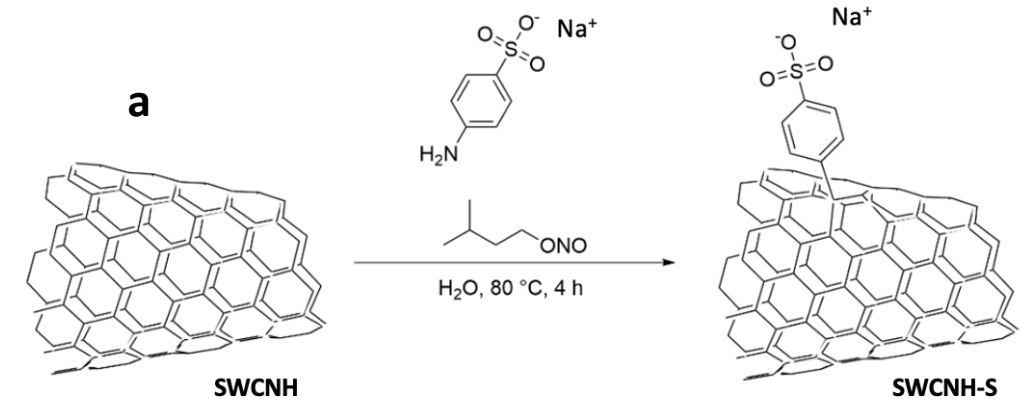
a
Na+
ONO
H2O, 80 °C, 4 h
SWCNH
SWCNH-S

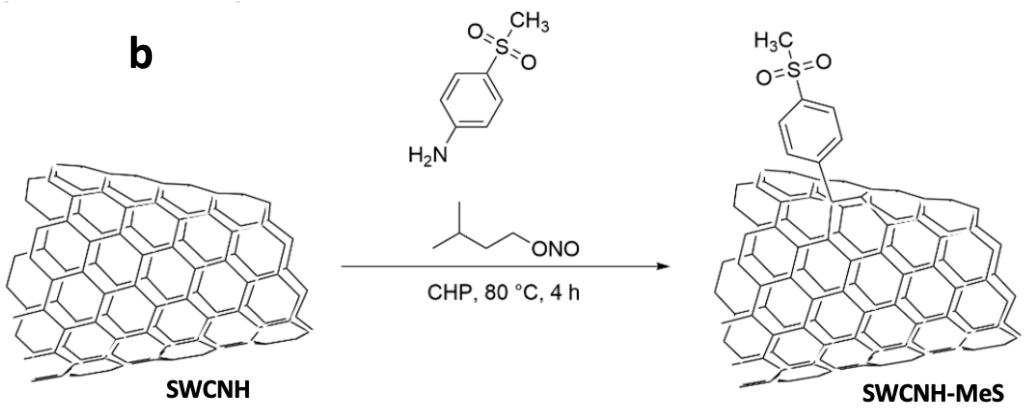
b
CH3
ONO
CHP, 80 °C, 4 h
SWCNH
SWCNH-MeS

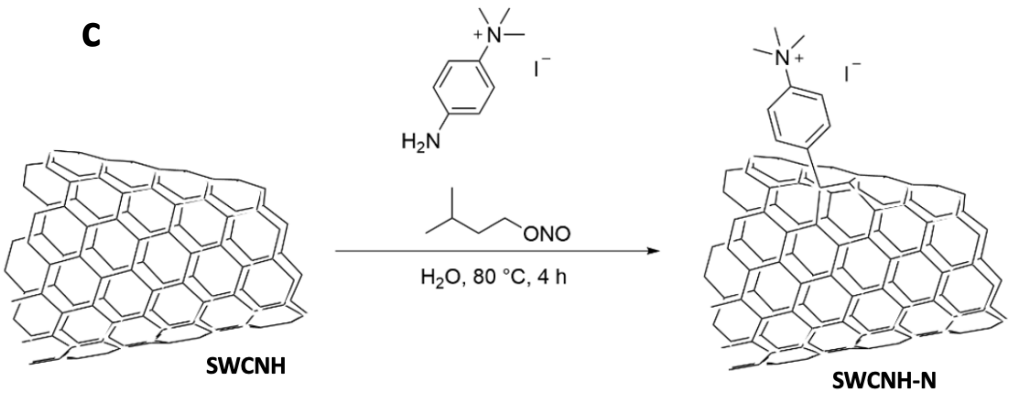
c
I−
ONO
H2O, 80 °C, 4 h
SWCNH
SWCNH-N

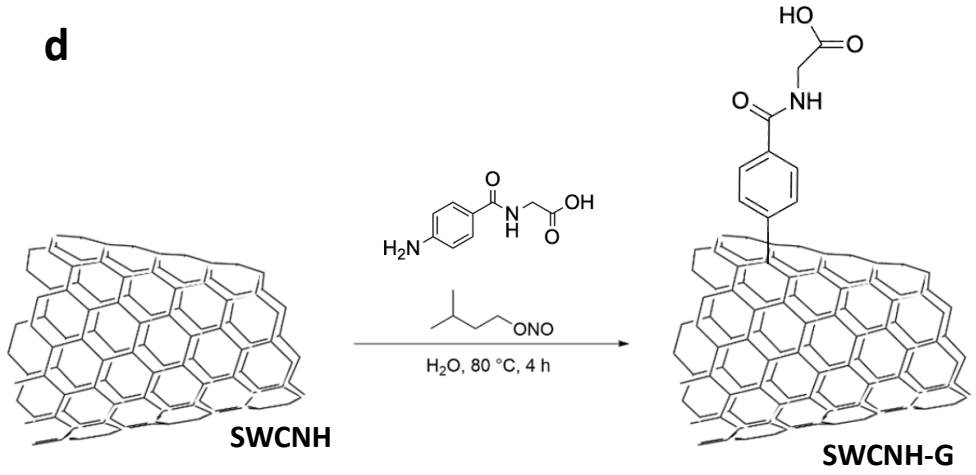

Figure 30: Tour reaction schemes synthesis of SWCNH derivatives

Thermogravimetric analysis in inert atmosphere was performed on SWCNH derivatives.

In Figure 31 thermograms for all functionalized SWCNH are shown, overlayed with that for purified pristine SWCNH.

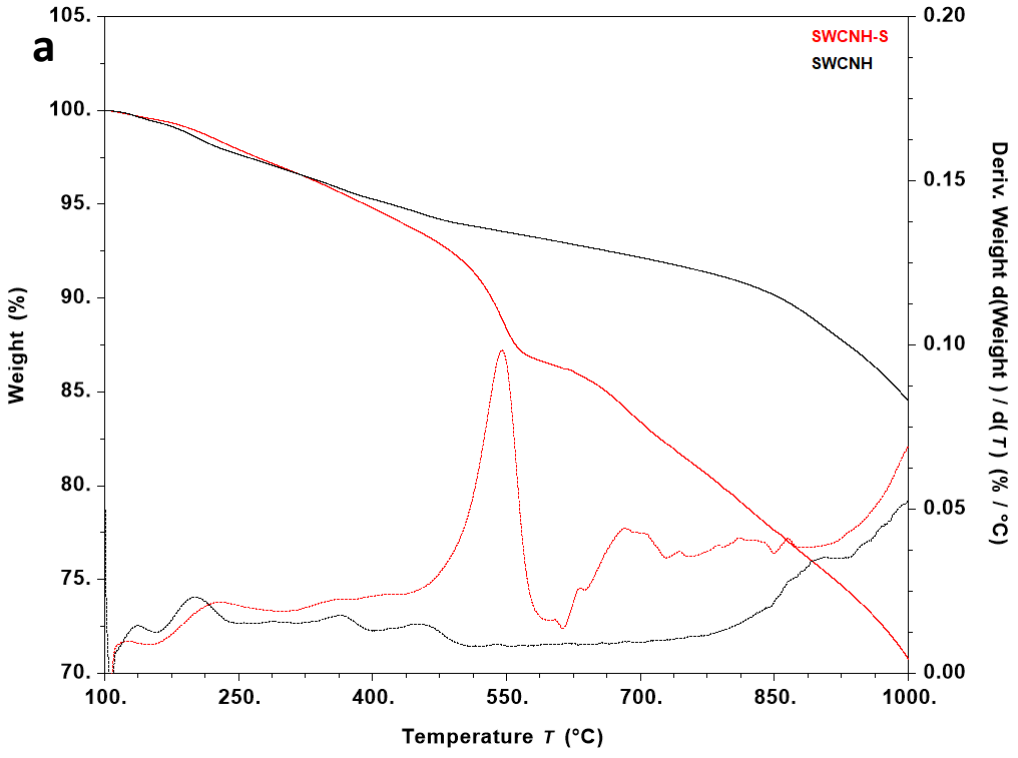

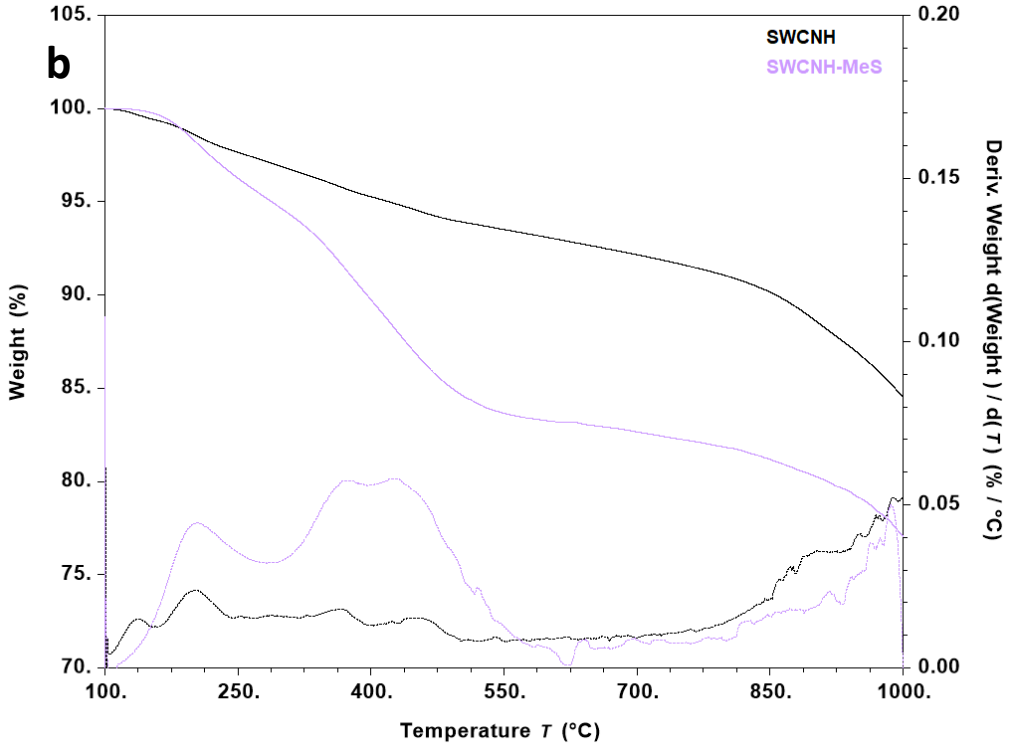
b
SWCNH
SWCNH-MeS
Weight (%)
Deriv. Weight d(Weight) / d(T) (% / °C)
Temperature T (°C)
105.
100.
95.
90.
85.
80.
75.
70.
0.20
0.15
0.10
0.05
0.00
100.
250.
400.
550.
700.
850.
1000.

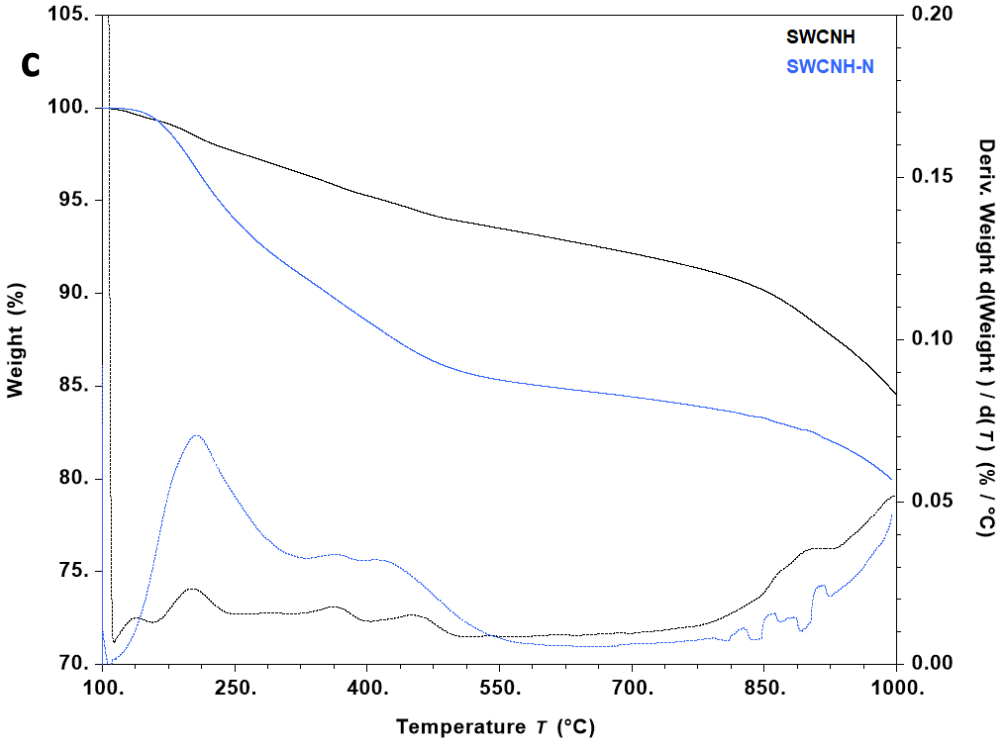
c
SWCNH
SWCNH-N
Weight (%)
Deriv. Weight d(Weight) / d(T) (% / °C)
Temperature T (°C)
105.
100.
95.
90.
85.
80.
75.
70.
0.20
0.15
0.10
0.05
0.00
100.
250.
400.
550.
700.
850.
1000.

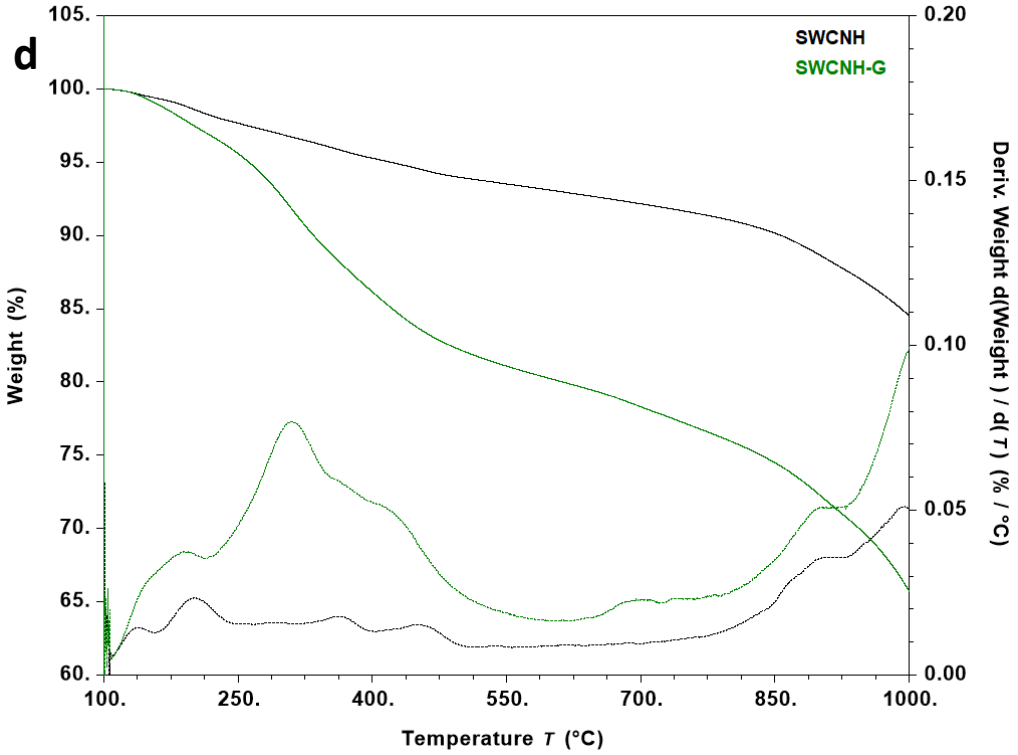

Figure 31: thermograms overlays of SWCNH derivatives and pristine SWCNH

For all SWCNH derivatives a weight loss step due to the presence of the organic moiety between can be observed between 150 and 610 °C, while SWCNH only show a slight and continuous degradation in the same temperature range, accounting for overall 6.5 %.

Therefore, the mass loss percentage due to the organic component alone was calculated subtracting the contribution of the pristine carbon nanostructure. In Table 1 the corrected values of the mass loss percentage are reported. From those values, FD for each derivative was calculated by using Equation 2, Equation 3 and Equation 4.

Derivative	Loss of mass [%]	FD [%]
SWCNH-S	5.5	1.2
SWCNH-MeS	10.1	1.5
SWCNH-N	6.9	1.5
SWCNH-G	12.7	1.8

Table 1: TGA measurements results for SWCNH derivatives

By analyzing the thermograms in Figure 31 is observed that all the functionalized SWCNH exhibited a degradation profile divided into multiple mass losses between 150 °C and 610 °C. However, it is impossible to determine exactly which degradation phenomena occurred during the analysis.

By comparing the mass loss percentages, a gradual increase is observed in the following order: SWCNH-S, SWCNH-N, SWCNH-MeS, and SWCNH-G.

This can be explained by the hypothesis that the functionalization efficiency increases slightly depending on the nature of the functional group with the following trend: benzensulfonate, trimethylbenzenammonium and methylsulfonibenzene, and N-(p-aminobenzoyl) glycine. In Table 2 values of water dispersibility and operative absorbance for all the f-SWCNH are reported.

Derivative	Dispersibility in water [mg/mL]	Operative absorbance
SWCNH-S	1.46	0.47
SWCNH-N	0.75	0.30
SWCNH-G	1.64	0.46

Table 2: water dispersibility and operative absorbance of SWCNH derivatives

Like all carbon-based nanostructures, SWCNH do not disperse easily in water due to the hydrophobic nature of their surface. However, the dispersibility values reported in Table 2 demonstrate that functionalization significantly promoted the water solubility of SWCNH.

Values for SWCNH-MeS are not reported in Table 2, because the extract was not stable in water, even after low centrifugation speeds, so it was excluded.

The functionalization of SWCNH with benzensulfonate and N-(p-aminobenzoyl) glycine groups results in higher dispersion values of than those obtained with trimethylbenzenammonium.

Despite the high degree of functionalization, the concentration obtained for SWCNH-N is much lower than that of SWCNH-S and SWCNH-G. It can be hypothesized that the trimethylbenzenammonium group does not significantly favor the dispersibility of CNS in water due to the type of interaction it can establish with it. The dispersion values of f-SWCNH are in agreement with their operative absorbance, Table 2. In Table 3 DLS and ZP data of SWCNH derivatives are reported. As explained above, the values of SWCNH-MeS are missing due to the low stability in water.

Derivative	Hydrodynamic diameter [nm]	PdI	ZP [mV]
SWCNH-S	118.7 ± 1.9	0.208 ± 0.014	-34.2 ± 1.1
SWCNH-N	241.5 ± 5.0	0.315 ± 0.043	+30.8 ± 0.4
SWCNH-G	122.4 ± 0.5	0.146 ± 0.010	-34.1 ± 0.6

Table 3: DLS and ZP data of SWCNH derivatives

Considering that the average hydrodynamic diameter of SWCNH aggregates in water is about 110 nm,[65] it can be said that functionalization with benzensulfonate and N-(p-aminobenzoyl) glycine groups promotes disaggregation more effectively than the functionalization with trimethylbenzenammonium. It is important to note that without functionalization it is practically impossible to obtain an aqueous solution of nanohorns.

The PdI values indicate that the size of aggregates in solution is quite uniform for all SWCNH derivatives.

The Zeta potential is considered an index of dispersion stability. The absolute value of ZP is used as an index of the degree of electrostatic repulsion between particles adjacent and similarly charged particles in the dispersion medium. Typically, a colloidal dispersion is considered stable if it exhibits an absolute value ZP > 30 mV. A ZP below 15 mV represents the onset of interparticle agglomeration, while values above 30 mV indicate that there is sufficient mutual repulsion to maintain colloidal stability.[66]

In this case, the extracts under consideration are not a simple colloidal dispersion; therefore, the ZP values cannot be interpreted absolutely, but must always be combined with other characterizations.

Taking into account the Zeta potential values obtained and all the properties discussed previously, suspension of SWCNH-S, SWCNH-G and SWCNH-N can be all considered stable in water.

Finally, the Zeta potential of SWCNH-S and SWCNH-N solutions matches the expected surface charge sign according to the functional group. The negative Zeta potential of SWCNH-G is also expected due to the deprotonation of the carboxylic group.

By analyzing all the characterizations performed on f-SWCNH, we can confirm that the Tour reaction can give water-dispersible derivatives with good stability.

It appears that the presence of negative charge on the surface of the SWCNH facilitates the solubility of the nanostructure and that functionalization of charged groups is responsible for a more concentrated dispersion.

Finally, it can be said that, despite the size of the aggregates, functionalization allows the establishment of repulsive interactions between charged f-SWCNH and attractive interactions between f-SWCNH and water, thanks to which carbon nanohorns can be dispersed in water. These three derivatives are hence promising candidates for the preparation of water-based scaffolds such as hydrogels and alginate, and they were further characterized through Raman and FT-IR spectroscopy.

Raman spectra of SWCNH-S, SWCNH-N and SWCNH-G are reported in Figure 32.

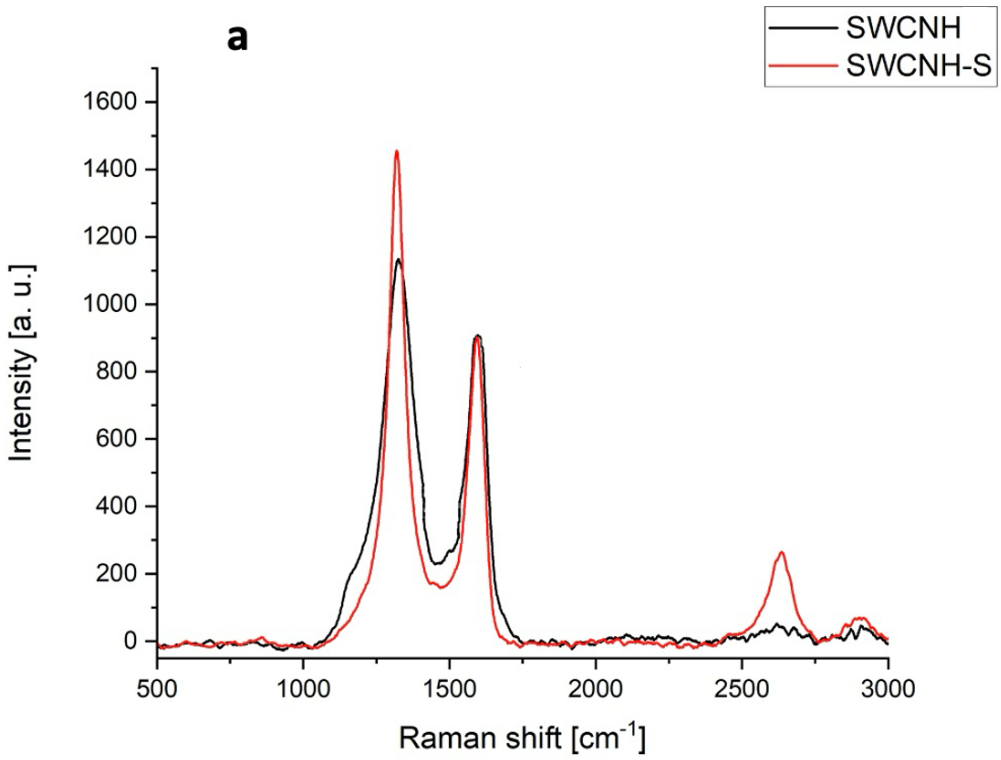

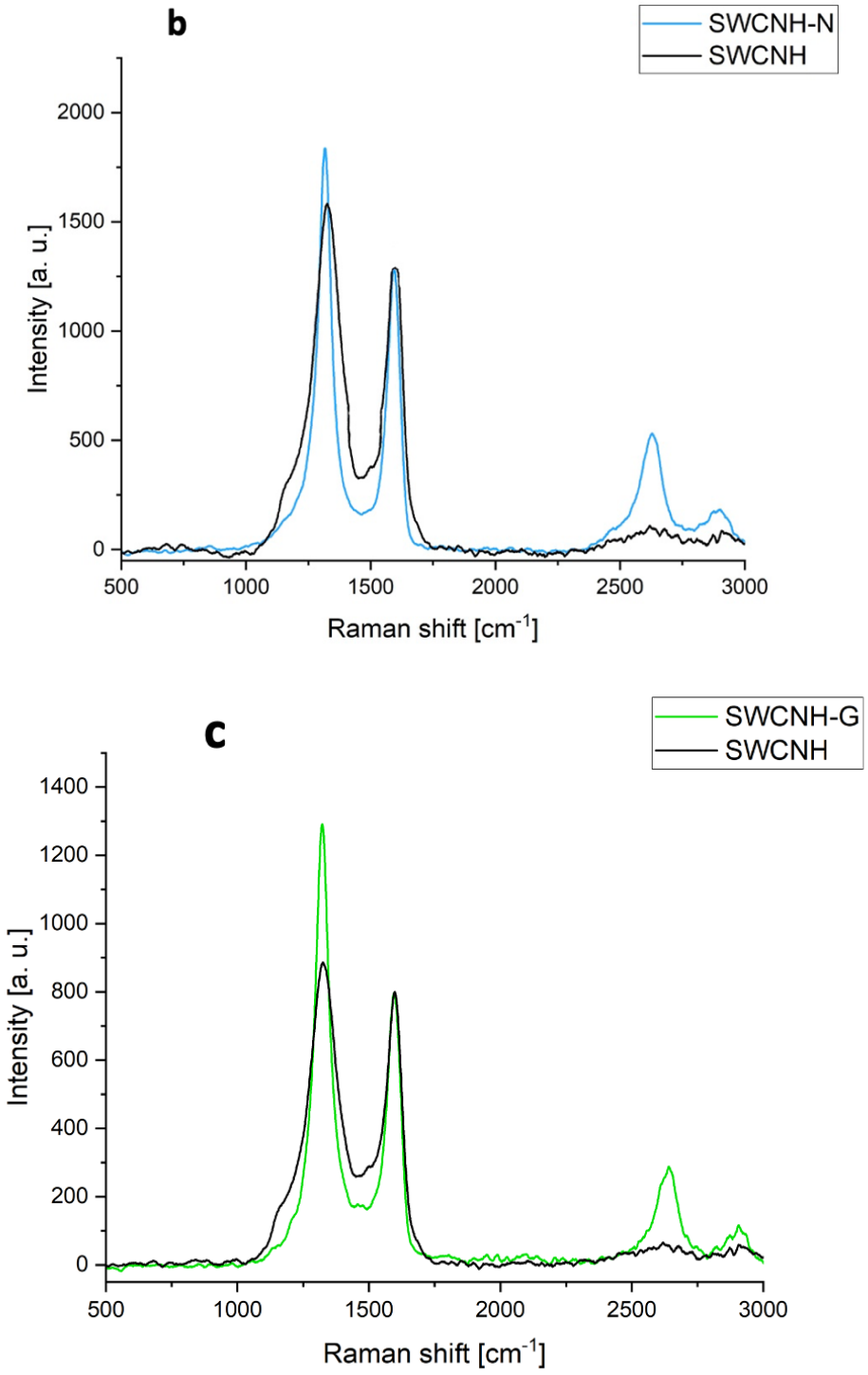

Figure 32: (a) SWCNH-S, (b) SWCNH-N, (c) SWCNH-G Raman spectra, compared to purified pristine SWCNH. Spectra normalized for the intensity of the G band.

CNS	I_D/I_G
SWCNH	1.15
SWCNH-S	1.56
SWCNH-N	1.44
SWCNH-G	1.41

Table 4: D/G band ratio of purified pristine SWCNH and SWCNH derivatives

Raman spectrum of each f-SWCNH is overlayed on that of purified pristine SWCNH and normalized on the intensity of the G band.

The I_D/I_G ratios (see section 1.3.5) are reported on Table 4: D/G band ratio of purified pristine SWCNH and SWCNH derivatives. By comparing the pristine SWCNH I_D/I_G ratio with that of SWCNH derivatives some differences are detected. In particular, the I_D/I_G ratio of SWCNH-S is the one that differs most of all from the I_D/I_G value of pristine SWCNH. The I_D/I_G ratios of SWCNH-N and SWCNH-G are very close to each other, and they differ although less markedly from the I_D/I_G value of pristine SWCNH. This is further confirmation that the pristine SWCNH structure was altered by covalent functionalization.

FT-IR spectra of the most water-dispersible SWCNH derivatives: SWCNH-S, SWCNH-N and SWCNH-G are reported in Figure 33, Figure 34 and Figure 35 respectively.

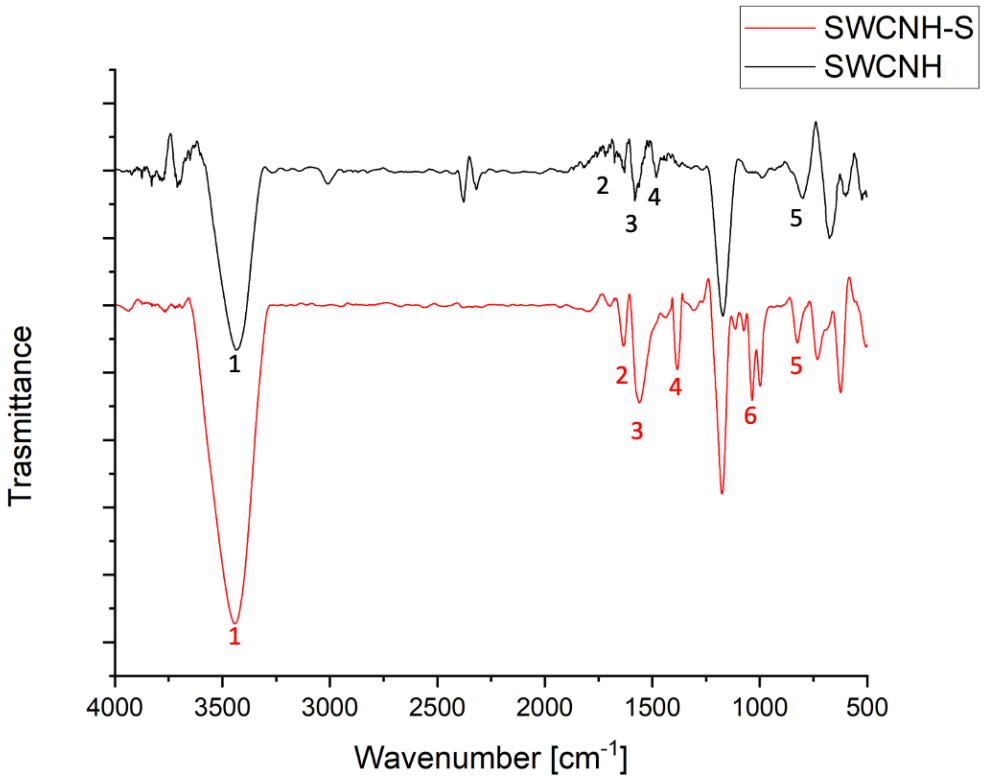

Figure 33: FT-IR spectrum of SWCNH-S

N°	Assignment	SWCNH [cm^{-1}]	SWCNH-S [cm^{-1}]
1	OH stretching	3448	3431
2	COO^- stretching	1638	1628
3	C=C stretching of SWCNH backbone	1561	1580
4	OH bending	1381	1479
5	C=C bending	1033	1045
6	S=O stretching	-	1136

Table 5: FT-IR peaks assignment for SWCNH and SWCNH-S

FT-IR spectroscopy showed the presence of the sulfonated group on the surface of SWCNH-S. With reference to Figure 33, the only different signal between the

SWCNH-S and pristine SWCNH spectra is the one peak number 6 at 1136 cm^{-1} that can be assigned to the benzensulfonate group though the location of the peak is slightly at lower wavenumber than usual (1380-1415 cm^{-1}).[67] The signal assignment is shown on Table 5. The signals present in both pristine SWCNH and SWCNH-S spectra belong to the carbon nanohorns chemical structure. The peaks number 1 at 3448 cm^{-1}, number 2 at 1638 cm^{-1} in Figure 33 represent the O-H and the COO^- stretching due to the possible presence of carboxylate groups generated on the SWCNH from the synthesis process by the manufacturer. The peak number 3 at 1561 cm^{-1} refers to the C=C stretching of SWCNH backbone. These three peaks belong to both SWCNH and SWCNH-S spectra as the peaks number 4 and 5.

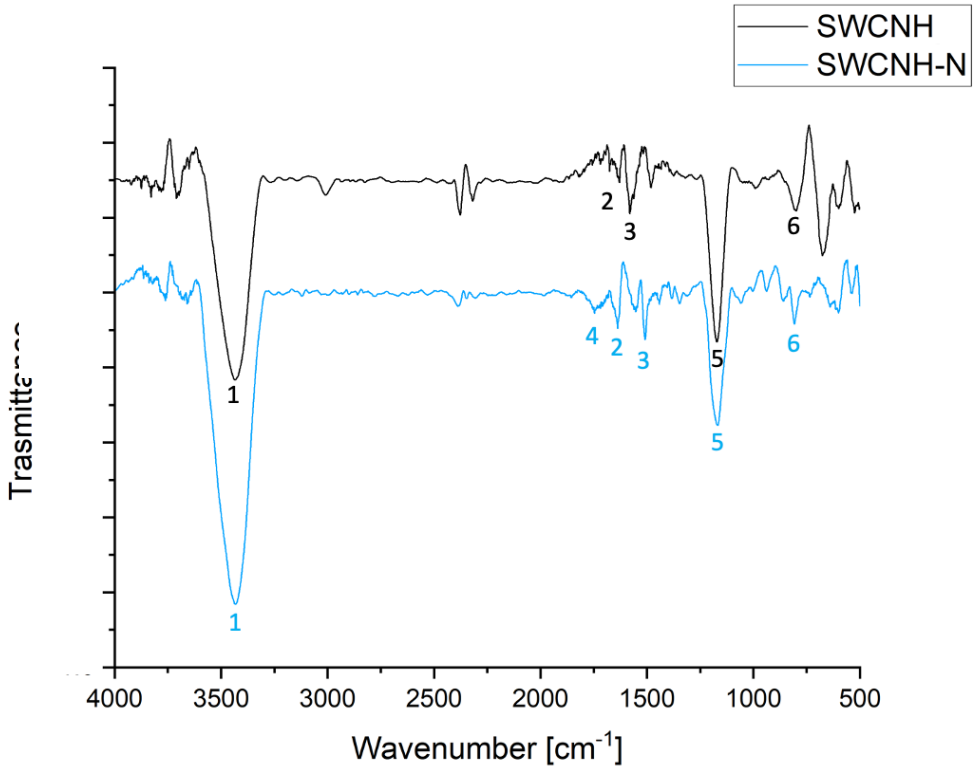

Figure 34: FT-IR spectrum of SWCNH-N

N°	Assignment	SWCNH [cm^{-1}]	SWCNH-N [cm^{-1}]
1	OH stretching	3448	3428
2	C=C stretching of SWCNH backbone	1638	1637
3	COO^- stretching	1561	1553
4	C-O stretching	-	1650
5	C=C bending	1033	804
6	C-H stretching	2378	2387

Table 6: FT-IR peaks assignment for SWCNH and SWCNH-N

FT-IR spectroscopy didn't allow to show differences between the two spectra reported in Figure 34.

Therefore, it is realistic to think that the nanostructure produces a noisy signal and some scattering which does not allow the signals of the functional group to be detected in a clear way. All the peaks of pristine SWCNH and SWCNH-N share the same wavenumber values reported on Table 6.

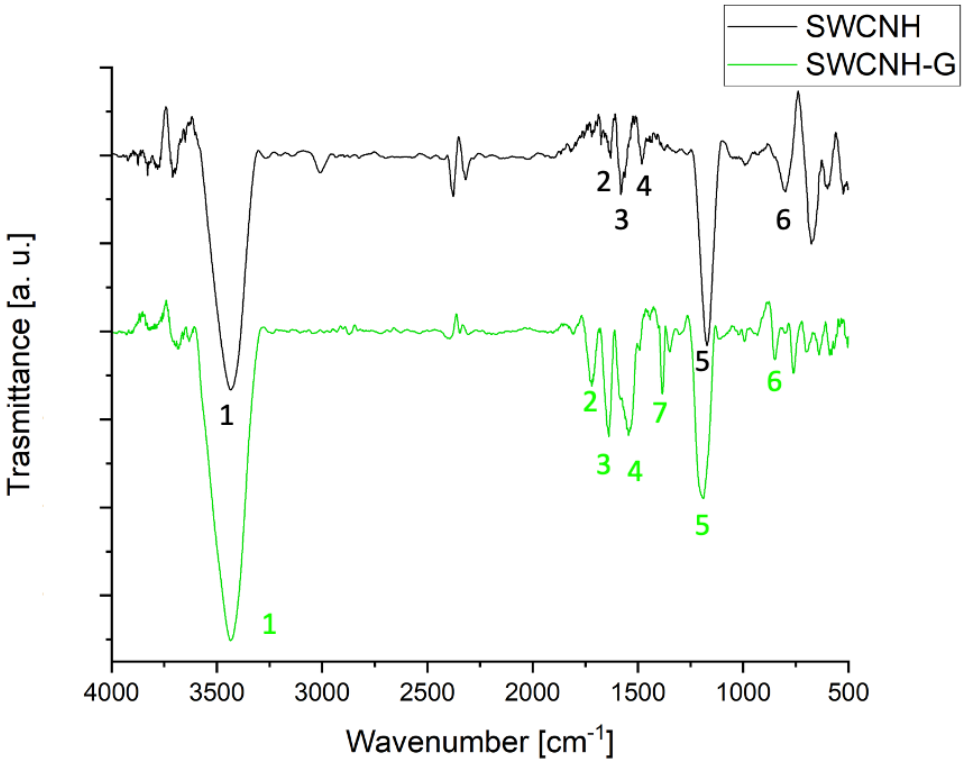

Figure 35: FT-IR spectrum of SWCNH-G

N°	Assignment	SWCNH [cm^{-1}]	SWCNH-G [cm^{-1}]
1	OH stretching	3448	3468
2	C=C stretching of SWCNH backbone	1638	-
2	C=O glycine stretching	-	1717
3	C=O amide stretching	-	1640
4	C-N amide stretching	-	1540
5	C-O stretching	1176	1186
6	C=C bending	1033	845
7	OH bending	-	1385

Table 7: FT-IR peaks assignment for SWCNHp and SWCNH-G

FT-IR spectroscopy in Figure 35 showed the presence of the peak number 2 of the C=O stretching of glycine group of the aminohippuric acid (1717 cm^{-1}). The peaks number 3 and 4 refer respectively to C=O (1640 cm^{-1}) and C-N (1540 cm^{-1}) amide stretching, the types of functional group present in the N-(p-aminobenzoyl) glycine.

2.4 Synthesis and characterization of multi-walled carbon nanotubes derivatives

In this thesis work the MWCNT-G derivative was synthesized, bearing functional group d (Figure 27).

MWCNT functionalization followed the Tour reaction approach with a molar ratio of 1:1:1 of MWCNT, aminohippuric acid (G) and isopentylnitrite used. The reaction scheme is reported in Figure 36.

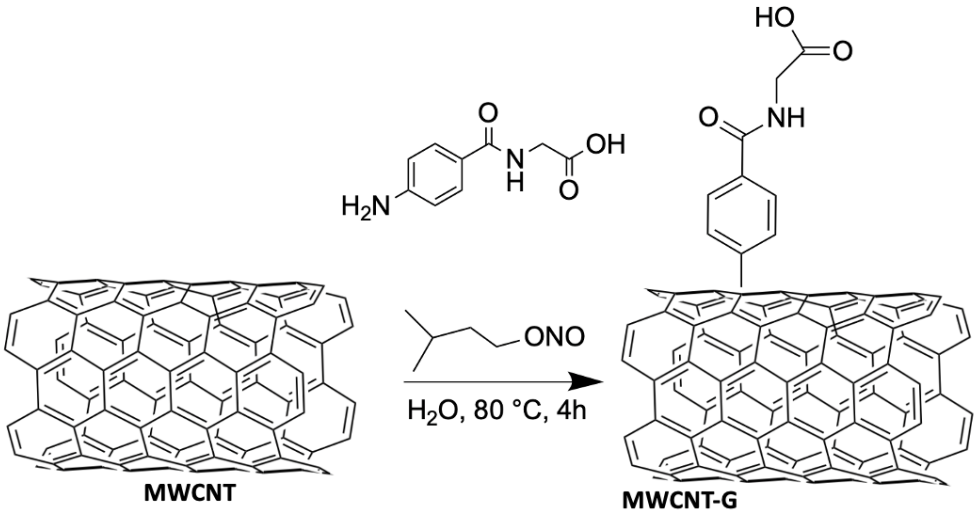

Figure 36: Tour reaction scheme synthesis of MWCNT-G

In Figure 37 the thermogram overlay of pristine MWCNT curve with the functionalized one is represented.

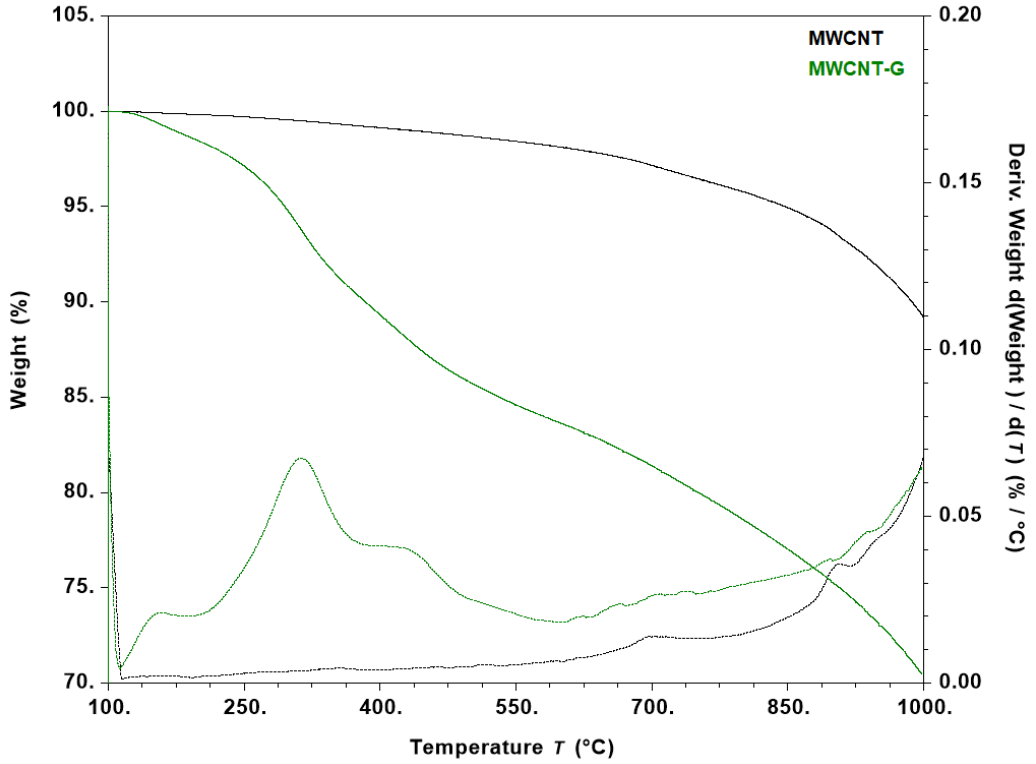

Figure 37: thermogram overlay of MWCNT-G and pristine MWCNT

Thermogravimetric analysis in inert atmosphere was performed on MWCNT-G and the results are reported in Table 8. The mass loss and the functionalization degree percentage were calculated in the temperature range between 150-610 °C, as for SWCNH derivatives.

Derivative	Loss of mass [%]	FD [%]
MWCNT-G	14.2	1.4

Table 8: TGA measure results of MWCNHT-G

The decomposition profile of pristine MWCNT shows a mass loss of 1.9 % in the temperature range from 150 to 610 °C, while a relevant decomposition starts from 700 °C onwards.

In the thermogram of MWCNT-G on Figure 37, an important mass loss is observed in the temperature range from 150 to 610 °C, due to both the introduced organic functionality and the pristine nanostructure. Therefore, to calculate the mass loss percentage compared to the organic component alone, the component already present in the pristine carbon nanostructure was subtracted. In Table 8 the corrected value of the mass loss percentage is reported.

In Figure 37 is observed that the functionalized MWCNT exhibited a degradation profile divided into multiple mass losses between 150 °C and 610 °C. However, it is impossible to determine exactly which degradation phenomena occurred during the analysis.

The degree of functionalization was calculated by using Equation 2, Equation 3 and Equation 4.

The calculated functionalization degrees of f-MWCNT previously synthesized are: 0.7 % for MWCNT-S, 0.8 % for MWCNT-MeS and 0.54 % for MWCNT-N.[60] By comparing the functionalization degree of MWCNT-G with the ones of f-MWCNT synthesized in the previous work [60] it seems that MWCNT-G are more functionalized than the other MWCNT derivatives, with a functionalization degree of 1.4 %. In Table 9 the f-MWCNT value of water dispersibility and operative absorbance are reported.

Derivative	Dispersibility in water [mg/mL]	Operative absorbance
MWCNT-G	0.66	0.09

Table 9: water dispersibility and operative absorbance of MWCNT-G

Similar to all carbon-based nanostructures, multi-walled carbon nanotubes do not disperse easily in water due to the hydrophobic nature of their surface. However, the dispersity values reported in Table 9 demonstrate that the functionalization significantly promotes the solubility of MWCNT.

The functionalization of MWCNT with N-(p-aminobenzoyl) glycine group leads to a dispersion value, 0.66 mg/mL, higher than MWCNT-MeS (0.36 mg/mL) and lower than MWCNT-S (1.56 mg/mL) and MWCNT-N (1.44 mg/mL), as obtained in the previous work.[60]

It can be hypothesized that the N-(p-aminobenzoyl) glycine group provides a lower dispersibility due to a slightly weaker interaction with water since the carboxyl group is not completely deprotonated. In Table 10 the ZP value of -33.4 mV is shown, in agreement with the presence of a negatively charged group.

Derivative	Hydrodynamic diameter [nm]	PdI	ZP [mV]
MWCNT-G	153.7 ± 5.4	0.305 ± 0.019	-33.4 ± 0.6

Table 10: DLS and ZP data of MWCNT-G

Considering the hydrodynamic diameter value of MWCNT-G in water shown in Table 10, it is slightly higher than those of MWCNT-S (144.0 nm, MWCNT-MeS (132.5 nm) and MWCNT-N (139.9 nm).[60]

It can be said that functionalization with benzensulfonate and N-(p-aminobenzoyl) glycine groups promotes the formation of a higher hydrodynamic sphere related to the higher steric encumbrance.

Also for this derivative a Raman spectrum was registered, Figure 38.

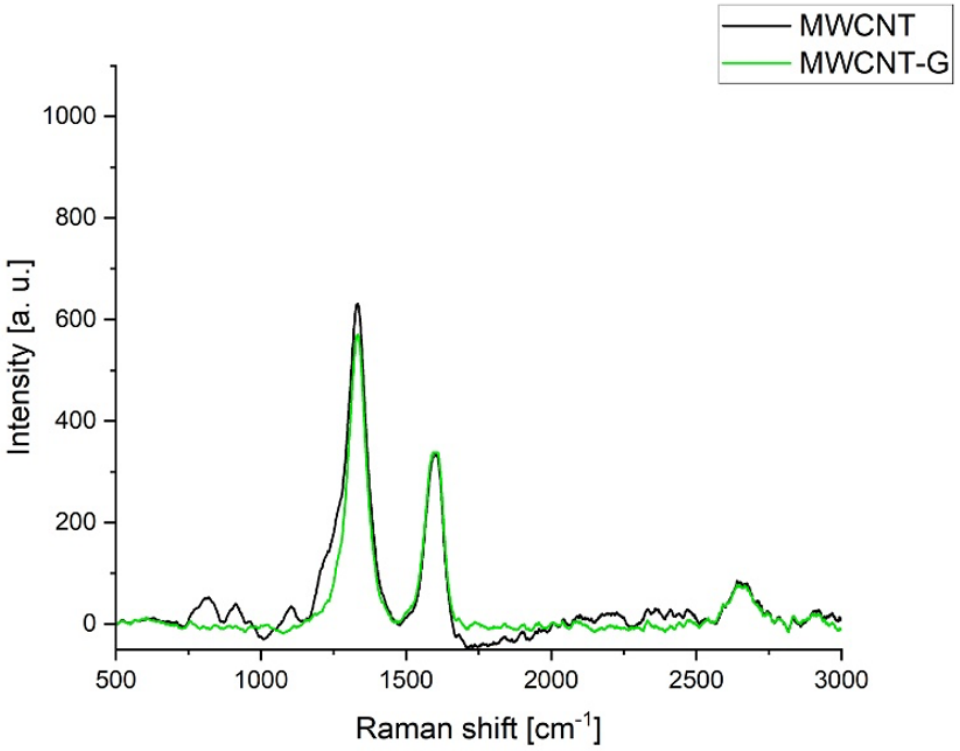

Figure 38: MWCN-G Raman spectrum, 50 mW

CNS	I_D/I_G
MWCNT	1.26
MWCNT-G	1.20

Table 11: D-band and G-band ratio of pristine MWCNT and MWCNT-G

Raman spectrum of f-MWCNT is overlayed on that of pristine MWCNT and normalized on the intensity of the G band.

The D and G bands ratios on Table 11 were calculated considering the average D and G bands ratios from three measures in different points of the sample to get a more reliable data. By comparing the pristine MWCNT I_D/I_G ratio with that of MWCNT derivative, not a huge difference is detected. Starting from this observation, it is possible to put forward the hypothesis that the pristine carbon nanostructure was not subjected to a heavy modification upon functionalization.

For further information about the functionalized carbon nanostructure FT-IR spectrum Figure 39 was registered.

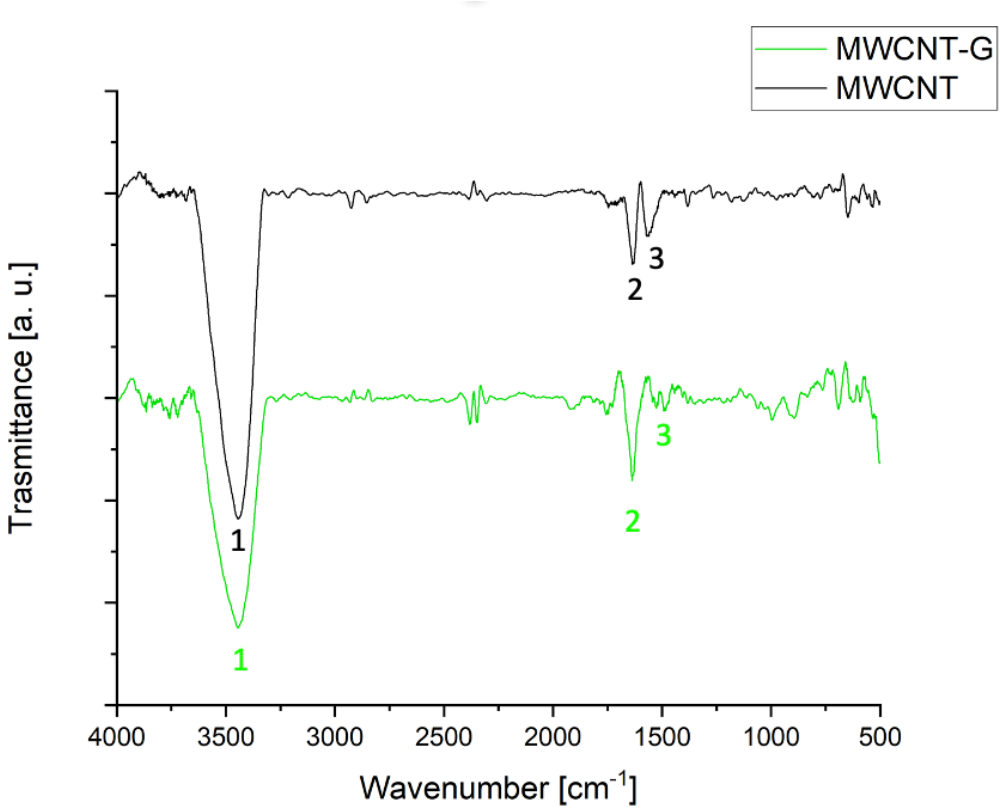

Figure 39: FT-IT spectrum of MWCNT and MWCNT-G

N°	Assignment	MWCNT [cm^{-1}]	MWCNT-G [cm^{-1}]
1	OH stretching	3450	3444
2	C=C stretching of MWCNT backbone	1631	-
2	C-N bending of amide	-	1638
3	C=C bending	-	992

Table 12: FT-IR peaks assignment for MWCNT and MWCNT-G

FT-IR spectroscopy showed the presence of the amide group bending. The intensity of the peak 2 in the MWCNT-G spectrum is slightly higher than the one of the same peak on the pristine MWCNT. This little difference can be explained with the presence of the amide group bending (1650-1580 cm^{-1}) on the MWCNT-G nanostructure. This result could agree with the previous Raman spectroscopy result, confirming that the covalent functionalization performed doesn't change substantially the nanostructure infrared properties. The peak 1 refers to the OH stretching due to the possible presence of carboxylate groups generated on the MWCNT from the synthesis process by the manufacturer. The peak 3 represents the C=C stretching of MWCNT backbone.

2.5 Synthesis and characterization of reduced graphene oxide derivatives

Also rGO was functionalized via Tour reaction to obtain derivatives rGO-S, rGO-N, rGO-MeS and rGO-G bearing the functional groups a, b, c, d (Figure 27) respectively, starting from the corresponding aniline precursors as described above, with 1:0.5:1 molar ratios between rGO, aniline and isopentylnitrite.

All the reaction schemes are reported in Figure 40.

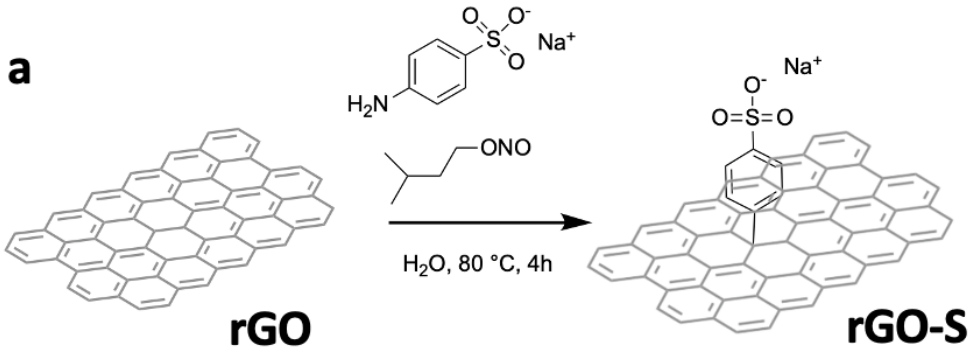

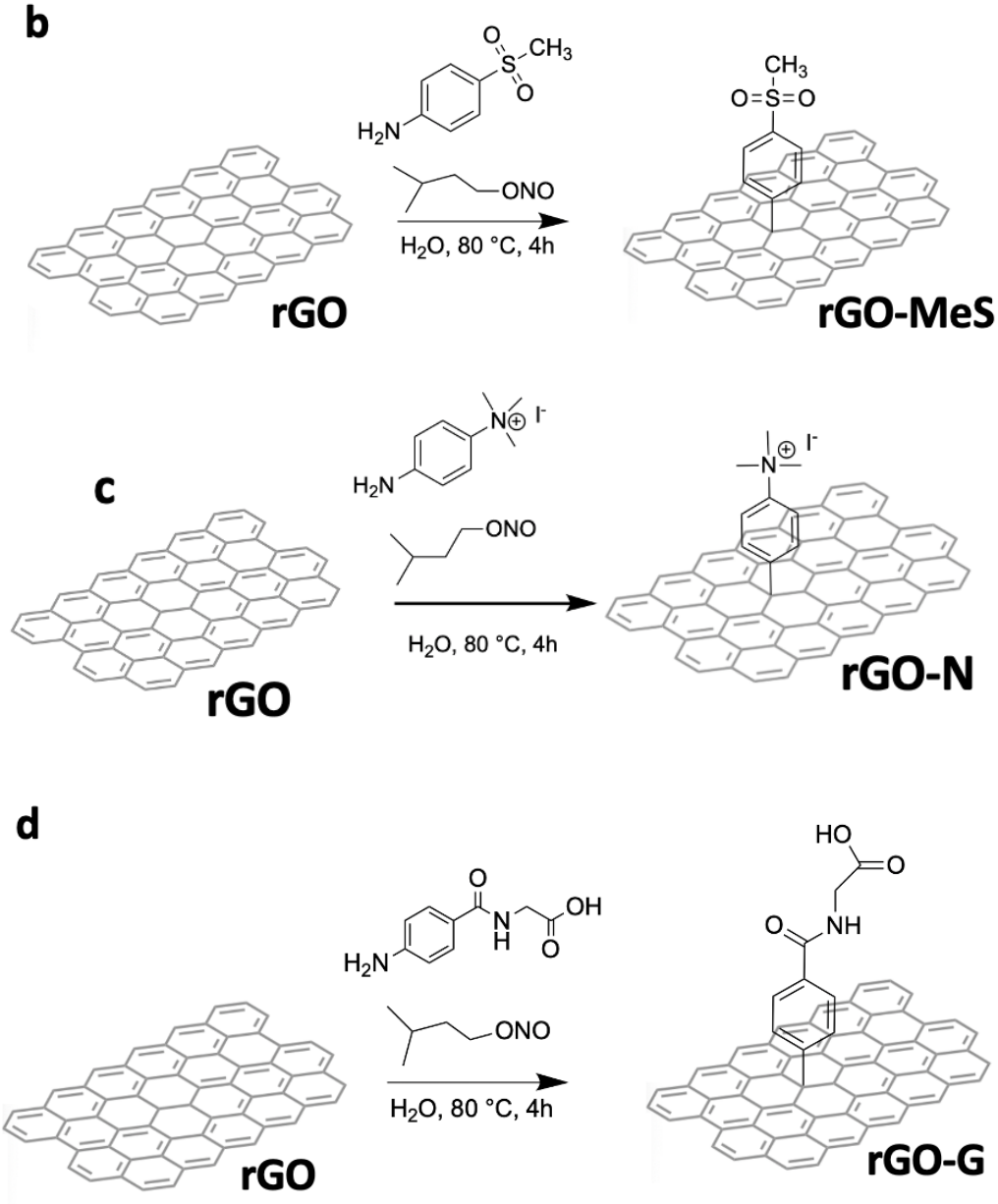

Figure 40: Tour reaction schemes synthesis of rGO derivatives

In Figure 41 all functionalized rGO thermograms are shown. Each thermogram represents the overlay of pristine rGO curve with the functionalized one.

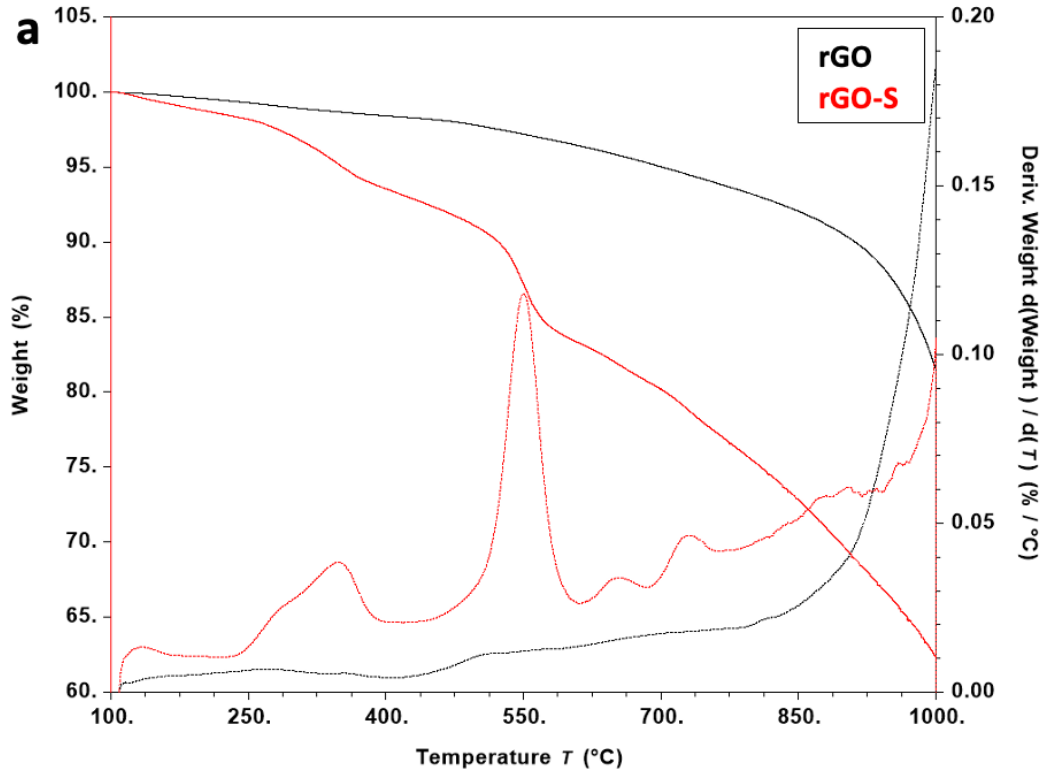
a
rGO
rGO-S
Weight (%)
Deriv. Weight d(Weight) / d(T) (% / °C)
Temperature T (°C)
105.
100.
95.
90.
85.
80.
75.
70.
65.
60.
0.20
0.15
0.10
0.05
0.00
100.
250.
400.
550.
700.
850.
1000.

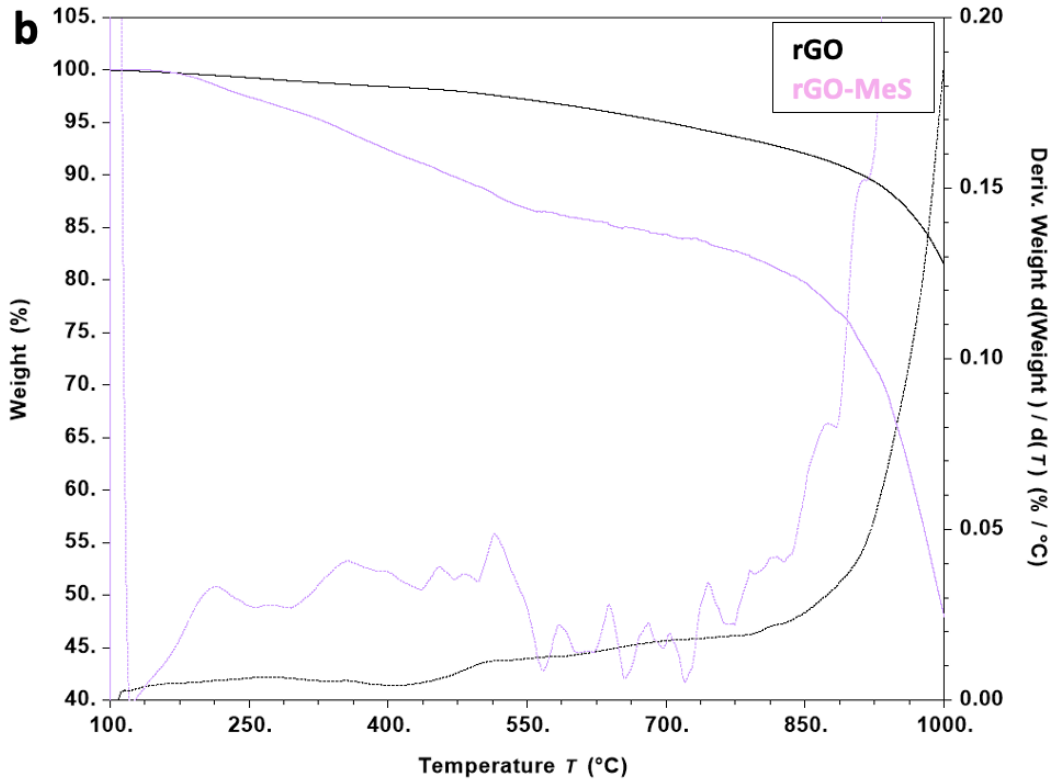
b
rGO
rGO-MeS
Weight (%)
Deriv. Weight d(Weight) / d(T) (% / °C)
Temperature T (°C)
105.
100.
95.
90.
85.
80.
75.
70.
65.
60.
55.
50.
45.
40.
0.20
0.15
0.10
0.05
0.00
100.
250.
400.
550.
700.
850.
1000.

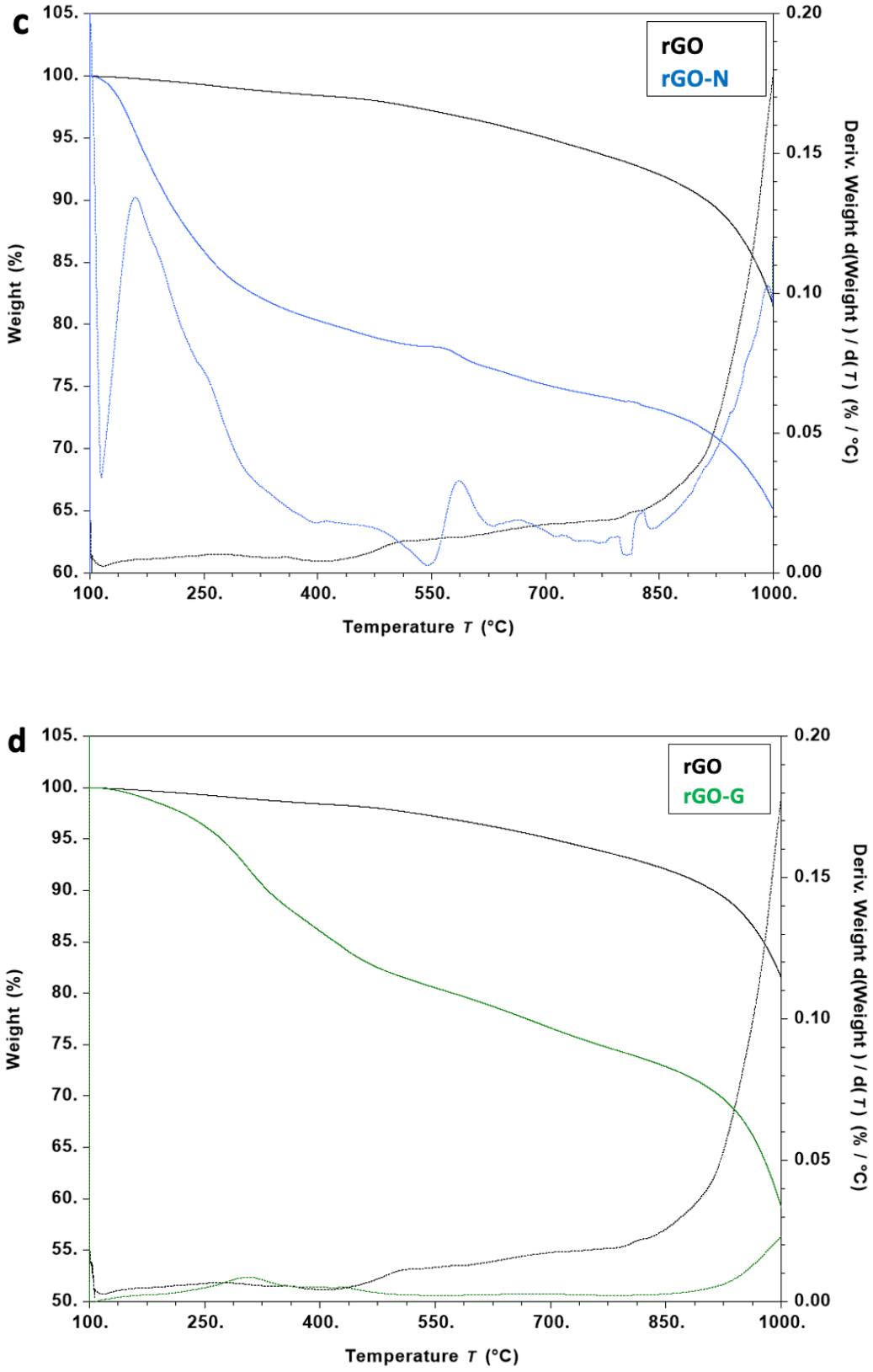

Figure 41: thermograms overlays of rGO derivatives and pristine rGO

Thermogravimetric analysis in inert atmosphere was performed on rGO derivatives and reported in Table 13. TGA analysis results are reported. The mass loss and the functionalization degree percentage were calculated in the temperature range between 150-610 °C for all rGO derivatives.

Derivative	Loss of mass [%]	FD [%]
rGO-S	11.7	1.4
rGO-MeS	10.7	1.3
rGO-N	16.6	2.3
rGO-G	16.6	1.9

Table 13: TGA measures results of rGO derivatives

The decomposition profile of pristine rGO shows a mass loss of 3.4 % in the temperature range from 150 to 610 °C.

In all the thermograms of f-rGO, mass loss is observed in the same temperature range (150–610 °C), due to both the introduced organic functionality and the pristine nanostructure. Therefore, to calculate the mass loss percentage compared to the organic component alone, it is necessary to subtract the component already present in the pristine carbon nanostructure. In Table 13 the corrected values of the mass loss percentage are reported.

By analyzing the thermograms in Figure 41 all the functionalized rGO exhibited a decomposition characteristic divided into multiple mass losses in the range from 150 °C to 610 °C. However, it was not possible to determine exactly which degradation phenomena occurred during the analysis.

Comparing the percentage of mass loss, a gradual increase was observed in the following order: rGO-MeS, rGO-S, rGO-N, and rGO-G. From this, FD values were calculated according to Equation 2, Equation 3 and Equation 4.

It can be suggested that the functionalization efficiency increases slightly depending on the nature of the functional group with the following trend:

methylsulfonibenzene, benzensulfonate, N-(p-aminobenzoyl) glycine and trimethylbenzenammonium.

In Table 14 all the f-rGO values of water dispersibility and operative absorbance are reported.

Derivative	Dispersibility in water [mg/mL]	Operative absorbance
rGO-S	0.690	0.42
rGO-MeS	0.117	0.03
rGO-N	0.313	0.28
rGO-G	0.202	0.05

Table 14: water dispersibility and operative absorbance of rGO derivatives

Like all carbon-based nanostructures, rGO are not readly dispersible in water due to the hydrophobic nature of their surfaces. However, the dispersibility values shown in Table 14 demonstrated that functionalization significantly enhanced the water solubility of rGO.

Functionalization of rGO with benzensulfonate and trimethylbenzenammonium groups resulted in higher dispersibility values than those obtained with N-(p-aminobenzoyl) glycine and methylsulfonylbenzene. This trend is opposite respect that of f-SWCNH, where the N-(p-aminobenzoyl) glycine group can significantly increase the dispersibility in water. This observation may be partly explained with the different relative FD of derivatives. Moreover, due the presence of oxygen-based (but maybe also N-based) functional groups in the graphene material, part of the glycine functional groups may have been grafted to the CNS through different bonds (with respect to the expected product of the Tour reaction), less effective in providing dispersibility.

Conditions applied to obtain f-rGO extract (see section 2.2) allowed to obtain a stable dispersion also with -MeS functional group.

Derivative	Hydrodynamic diameter [nm]	PdI	ZP [mV]
rGO-S	350.5 ± 4.2	0.294 ± 0.025	-40.2 ± 0.6
rGO-MeS	2427.8 ± 261.8	0.255 ± 0.098	-20.9 ± 0.1
rGO-N	1545.0 ± 113.6	0.372 ± 0.099	32.1 ± 0.3
rGO-G	1055.0 ± 75.6	0.493 ± 0.074	-25.8 ± 1.5

Table 15: DLS and ZP data of rGO derivatives

Considering the hydrodynamic diameter of the rGO aggregates obtained in water, it can be noticed that functionalization with benzensulfonate promotes disaggregation much more effectively than the functionalization with the other groups, which is consistent with the trend of dispersibility. It is important to note that without functionalization it is practically impossible to obtain an aqueous graphene solution.

The PdI values indicate that the size of aggregates in solution is quite uniform for all rGO derivatives.

In this case, the extracts under consideration cannot be considered as a simple colloidal dispersion; therefore, the ZP values cannot be interpreted in absolute terms, but must always be combined with other properties.

Considering the obtained the Zeta potential values and all the properties discussed previously, rGO-S can be considered stable in water, while the other three rGO derivatives tend to aggregate more.

The absolute values of Zeta potential also confirm similar trends between the different derivatives. Furthermore, the signs are consistent with the electrostatic charge of the functional groups.

Due to the presence of precipitates at the bottom of the vial of rGO derivatives after only one day after the synthesis, it was decided to monitor the hydrodynamic diameter of the fraction remaining in the dispersion for 96 h with 4 intervals of 24 h. Here, in Figure 42 the hydrodynamic diameter trend of each rGO derivative is shown.

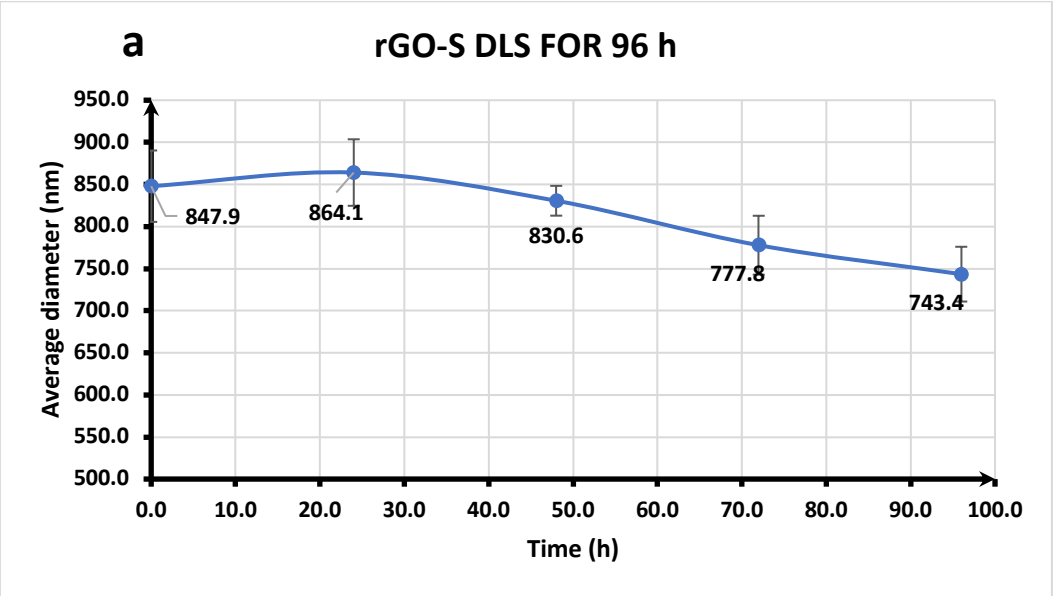

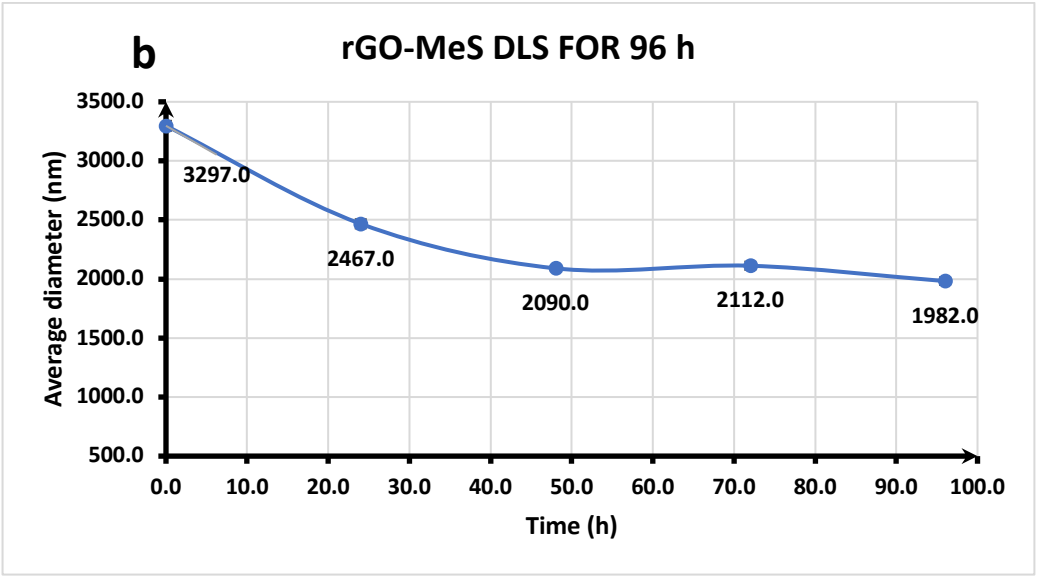

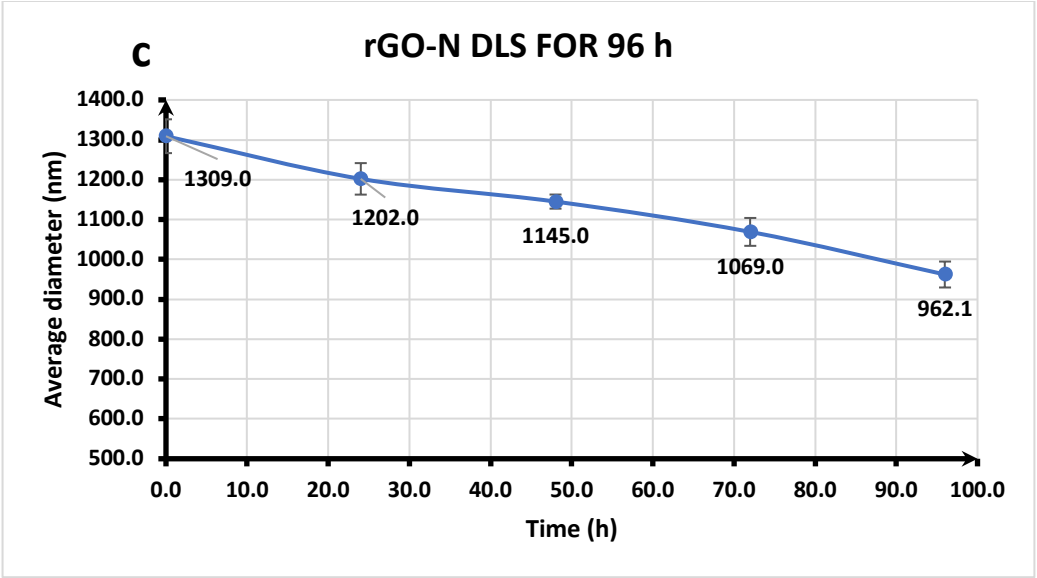

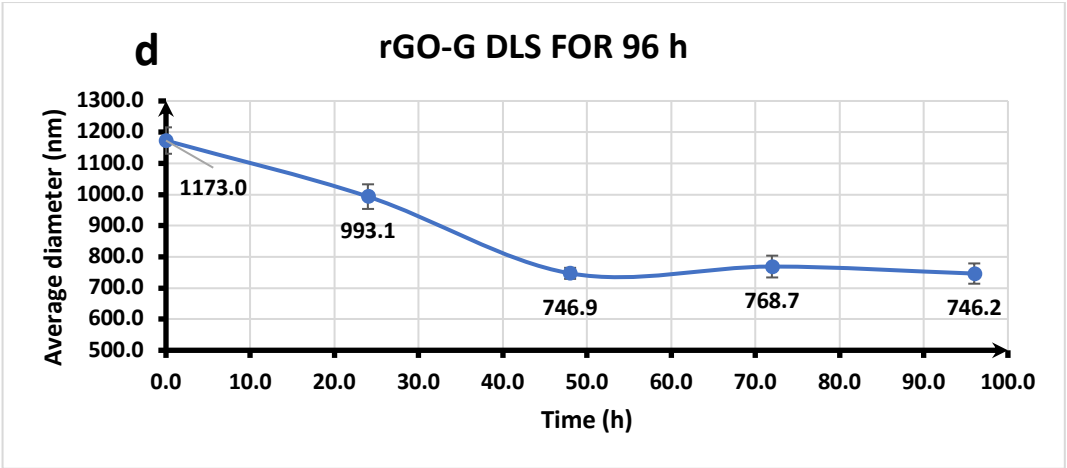

Figure 42: DLS monitoring for 96 h of (a) rGO-S, (b) rGO-MeS, (c) rGO-N and (d) rGO-G

By analyzing the characterizations performed on f-rGO, we can confirm that the Tour reaction can give water-dispersible derivatives with no long-lasting stability over time. In all rGO derivatives a variation of the hydrodynamic diameter is observed, a consistent decrease occurs for all rGO derivatives except for rGO-S. Maybe, the functionalization is not sufficient to enhance the water dispersibility of pristine rGO, indeed the vials containing the dispersions of rGO derivatives in water showed a black precipitate after only one day from the synthesis. The precipitate was most likely composed of the heaviest aggregates of f-rGO. Probably, the variation of the average hydrodynamic diameter can be associated with this phenomenon.

Among the four rGO derivatives synthesized, the rGO-S had the higher dispersibility value, this feature is crucial for the use of f-CNS with water-based scaffolds such as hydrogels and alginate, so only the rGO-S was subjected to further analysis: Raman and FT-IR spectroscopy.

The Raman spectrum of the most promising derivative (rGO-S) was registered and reported in Figure 43 overlapped with pristine rGO Raman spectrum.

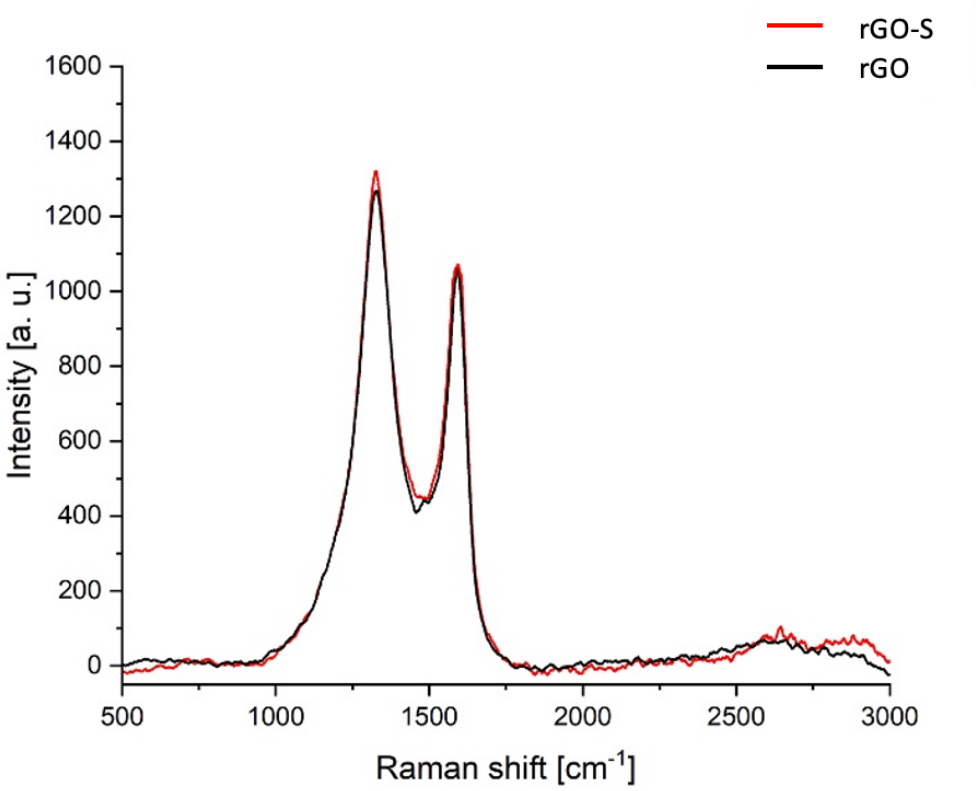

Figure 43: rGO-S and pristine rGO Raman spectra overlap, 50 mW

CNS	I_D/I_G
rGO	1.07
rGO-S	1.10

Table 16: D-band and G-band ratio of pristine rGO and rGO-S

Raman spectrum of f-rGO is overlayed on that of pristine rGO and normalized on the intensity of the G band.

The D and G bands ratios on Table 16 were calculated considering the average D and G bands ratios from three measures in different points of the sample to get a more reliable data. By comparing the pristine rGO I_D/I_G ratio with that of rGO derivative not a huge difference is detected. Starting from this observation, it is possible to put forward the hypothesis that the pristine carbon nanostructure of

single-layer graphene powder was not subjected to a heavy modification after the functionalization.

For further information about the functionalized carbon nanostructures FT-IR spectrum of the most soluble derivative, rGO-S was registered, Figure 44.

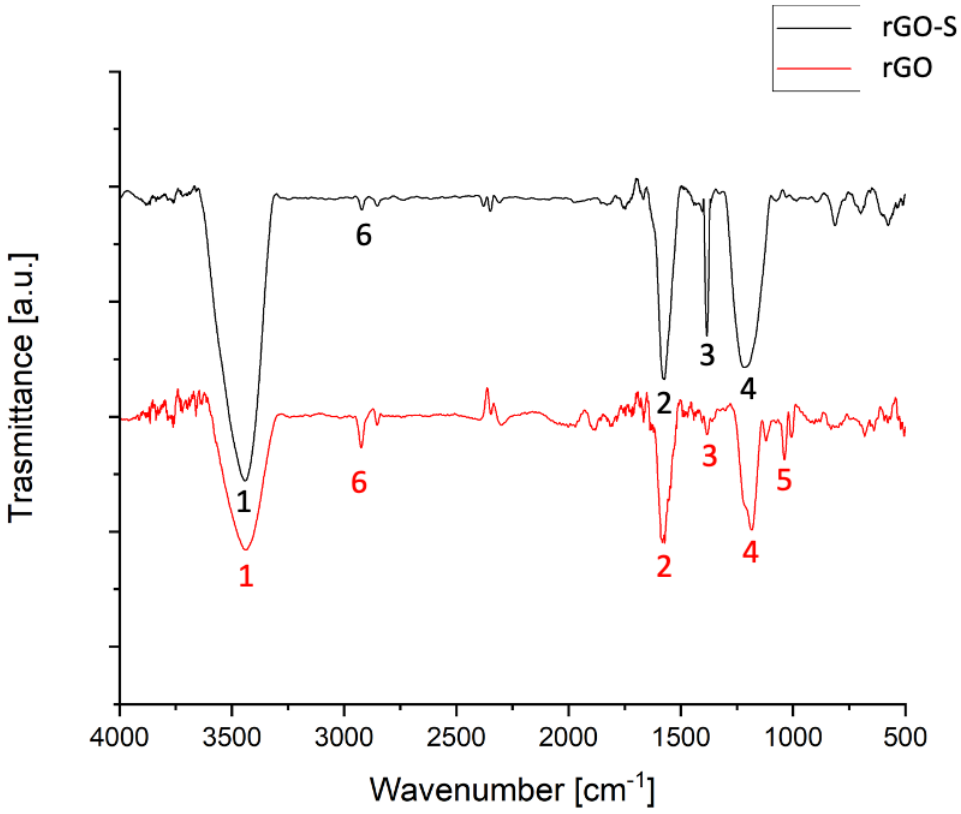

Figure 44: FT-IR spectrum of rGO and rGO-S

N°	Assignment	rGO [cm^{-1}]	rGO-S [cm^{-1}]
1	OH stretching	3441	3434
2	C=C stretching of rGO backbone	1571	1582
3	C-H bending	1382	1383
4	C-O stretching	1219	1180
5	S=O stretching	-	1040
6	C-H stretching	2919	2923

Table 17: FT-IR peaks assignment for rGO and rGO-S

FT-IR spectroscopy allowed to distinguish the peak number 5 on the rGO-S spectrum in Figure 44. This peak is related to the S=O stretching (1040 cm^{-1}) of the sulfonated group.

For the other peaks the spectra of pristine rGO and rGO-S are very similar, so the covalent functionalization doesn't affect heavy the infrared properties of the nanostructure. The peak number 1 represents the O-H stretching of the oxygenated groups on the surface of the rGO, residues from manufacturing. The peaks number 2 and 4 are respectively the stretching of rGO C=C backbone (1571 cm^{-1}) and the C-O stretching (1219 cm^{-1}). The peaks number 3 and 6 represent respectively the C-H bending (1382 cm^{-1}) and the C-H stretching (2919 cm^{-1}) probably caused by the chemical reduction by the manufacturer.

2.6 Conclusions and perspectives

In this paper, SWCNH, MWCNT and rGO were functionalized with benzenesulfonate, methylsulfonylbenzene, N-(p-aminobenzoyl) glycine and trimethylbenzene ammonium groups.

Notably, the functionalization of SWCNH, MWCNT and rGO with N-(p-aminobenzoyl) glycine and all the functionalizations of pristine rGO were carried out for the first time in the research group.

Studies performed on the resulting f-CNS demonstrated that functionalization of the nanostructures by the Tour reaction rendered them water dispersible.

For both SWCNH and rGO, the benzenesulfonate group was found to promote higher dispersibility in water, while the methylsulfonylbenzene is the worst group regard the enhancement of water dispersibility. The trimethylbenzeneammonium group can enhance the dispersibility better than N-(p-aminobenzoyl) glycine group for rGO, while for SWCNH an opposite trend is found.

Considering the dispersibility of f-MWCNT with N-(p-aminobenzoyl) glycine group, its value is higher than the dispersibility data for MWCNT-MeS and lower than MWCNT-S and MWCNT-N obtained in the previous thesis work.[60]

The Zeta potential values obtained are consistent with the charge of the groups attached to the surface to all CNS. The rGO-MeS derivative presents a negative ZP value of -20.9 mV despite the CNS was functionalized with a neutral group. This can be explained starting from the consideration that the pristine rGO presents carboxyl and hydroxyl groups on its surface which deprotonate in water environment lowering in this way the ZP value.

By examining the Raman spectra, for all the most water dispersible f-CNS the I_D/I_G ratio is close to that of pristine CNS, so it is possible to deduce that the functionalization doesn't heavily modify the CNS surface, but it is enough to make it dispersible in water maintaining its electrical properties.

The FT-IR spectra of f-CNS confirm the presence of ammino, carboxyl, functional groups and they are not present in the FT-IR of pristine CNS, so this is further confirmation that the functionalization performed with Tour reaction was

successful. The functionalization of CNTs represents an important step towards the goal of dispersing CNTs in hydrogels designed for biomedical applications related to tissue engineering.[5]

f-CNS can be incorporated into biobased hydrogels composed of natural polymers such as chitosan, alginate, gelatin, and hyaluronic acid or of synthetic molecules such as self-assembling peptides. Different methodologies could be investigated to design nanocomposite materials that can mimic as much as possible natural tissues, such as electrospinning and 3D printing.

Moreover, the effect of the introduction of the CNS on the properties of the hydrogels could be investigated through rheological tests and conductivity measurements. Finally, nanocomposite hydrogels may be tested for their ability to promote cell proliferation and differentiation, as well as possible cytotoxicity.

3 Experimental part

3.1 Solvents and reagents

Solvent	CAS	MM [g ·mol^{-1}]	d [g·mL^{-1}] 25 °C	b. p. [°C]	Company
Methanol	67-56-1	32.04	0.7910	64.70	Sigma-Aldrich
Chloroform	67-66-3	119.38	1.4760	60.50-61.50	Sigma-Aldrich
Ethanol	64-17-5	46.07	0.79	78.02	Merck
DMSO	68-12-2	78.13	1.10	189.02	Sigma-Aldrich
DMF	68-12-2	73.09	0.944	153.01	Sigma-Aldrich
CHP	6837-24-7	167.25	1.007	284.00	TCI

Table 18: information about solvents

Reagent	CAS	MM [g ·mol^{-1}]	d [g·mL^{-1}] 25 °C	Company
Sodium sulfanilate dihydrate	6106-22-5	231.2	0.170	Sigma-Aldrich
4-methylsulfonylanilin	5470-49-5	171.22	1.0	TCI
Isopentyl nitrite	110-46-3	117.15	0.872	Sigma-Aldrich
Methyl iodide	74-88-4	141.94	2.28	Sigma-Aldrich
Triethylamine	121-44-8	101.19	0.726	Sigma-Aldrich
Phthalic anhydride	85-44-9	148.12	1.53	Sigma-Aldrich
Hydrazine monohydrate	7803-57-8	50.06	1.032	Sigma-Aldrich
Triethylamine	121-44-8	101.19	0.726	Sigma-Aldrich
N,N-dimethylbenzene-1,4-diammina	99-98-9	136.19	/	Sigma-Aldrich
Methyl iodide	74-88-4	141.94	2.28	Sigma-Aldrich
N-Cyclohexyl-2-pyrrolidone	6837-24-7	167.25	1.007	Sigma-Aldrich

Table 19: reagents information

SWCNH were purchased from Carbonium s.r.l (Padua, Italy; production year 2023) and present a dahlia-type shape with a diameter of 60-120 nm.

rGO was purchased from ACS Material company (Pasadena, California, USA, production year 2023) and presents from 1 to 5 atoms layer of graphene oxide nanosheets.

MWCNT were purchased from ACS Material company (Pasadena, California, USA, production year 2023) and present an outer diameter of 8-15 nm, an inner diameter of 3-5 nm and a length from 0.5 to 2 nm.

3.2 Instruments and analytic procedures

3.2.1 Thin Layer Chromatography (TCL)

TLC analyzes were conducted on TLC silica gel 60 F254. The stains were observed using a UV lamp at 254 nm.

3.2.2 Nuclear Magnetic Resonance (NMR)

The ^{1}H-NMR spectra were acquired with the Bruker AC-300 instrument, operating at 300 MHz. Spectra were processed using the software MestReNova.

3.2.3 Tip sonication

The nanostructures were dispersed in the solvent by sonication a tip using the Misonix 3000 sonicator with titanium tip. The sonication was conducted at power level 2.0 (4-6 W) alternating ON and OFF periods, each lasting 3 s, regardless of time of sonication required by the procedure.

3.2.4 Bath sonication

The bath sonicator used is the Bandelin SONOREX filled with water distilled (power 320 W, RF frequency 35 kHz).

3.2.5 Centrifugation

Centrifugations were conducted with an MR23i centrifuge (Thermo SCIENTIFIC). The duration of each centrifugation cycle for f-MWCNTs and f-SWCNH was 10 min, at 5000 rpm and 10000 rpm, respectively.

3.2.6 Thermogravimetric Analysis (TGA)

The thermogravimetric measurements were conducted using TGA Q5000IR (TA Instruments). Analyses of functionalized CNSs were performed in nitrogen atmosphere with an initial isotherm at 100 °C for 10 min, to remove any residual traces of solvent, followed by a ramp temperature of 10 °C/min up to 1000 °C. The thermograms have been processed using TA Instruments software, TRIOS.

3.2.7 Dynamic Light Scattering (DLS)

DLS measurements were conducted using Zetasizer Nano S (Malvern Instruments). The analyses were conducted at room temperature, in MilliQ water, using low-volume cuvettes in plastic with a reduced optical path. The final data for each sample was derived from the average of three measurements, each of which involves 11 runs. The data were processed with the Zetasizer software.

3.2.8 Zeta Potential (ZP)

Zeta Potential measurements were conducted using Zetasizer Nano S (Malvern Instruments). The analyses were carried out at room temperature, in a solution of 0.2 mM NaCl and MilliQ water, using the appropriate cell. The final data for each sample is obtained from the average of three measurements, each of which involves 40 runs. The data were processed with Zetasizer software.

3.2.9 UV-Vis-NIR spectroscopy

UV-Vis-NIR spectra were acquired between 280 nm and 1400 nm using the Varian Cary 5000 spectrophotometer. The measurements were conducted at room temperature in MilliQ water. The analyzes were conducted in quartz cuvettes with

an optical path of 1 cm, at a scanning speed of 300 nm/min and with a bandwidth of 2 nm. The spectra were processed using Origin 2018 software.

3.2.10 Preparation of f-SWCNH dispersions

5 mg of f-SWCNH were dispersed in 2.5 mL of MilliQ water by treatment with tip sonicator for 1 min. The mixture was centrifuged at 10,000 rpm for 10 minutes and the supernatant was then recovered and filtered on cotton.

To conduct DLS, ZP and UV-Vis-NIR analysis the following samples were prepared:

• 100 µL of dispersion was added to 1.0 mL of MilliQ in water a plastic cuvette for DLS analysis.

• 100 µL of dispersion was added to 700 µL of MilliQ water and a 160 µL of a 1 mg/mL NaCl solution in a cell for analysis Zeta Potential.

• 30 µL of dispersion was added to 2.97 mL of MilliQ in water a quartz cuvette for UV-Vis-NIR analysis.

• 1.0 mL of dispersion was evaporated on a TGA pan, following the drop-casting technique, and analyzed by TGA a 100 °C in air.

• For each synthesized derivative, a TGA measurement was conducted in inert atmosphere on a small amount of dry nanostructure (1-2 mg).

3.2.11 Preparation of f-MWCNT dispersions

5 mg of f-MWCNT were dispersed in 2.5 mL of MilliQ water by treatment with tip sonicator for 1 min. The mixture was centrifuged at 5,000 rpm for 10 minutes and the supernatant was then recovered and filtered on cotton.

To conduct DLS, ZP and UV-Vis-NIR analysis the following samples were prepared:

• 100 µL of dispersion was added to 1.0 mL of MilliQ in water a plastic cuvette for DLS analysis.

• 100 µL of dispersion was added to 700 µL of MilliQ water and a 160 µL of a 1 mg/mL NaCl solution in a cell for analysis Zeta Potential.

• 30 µL of dispersion was added to 2.97 mL of MilliQ in water a quartz cuvette for UV-Vis-NIR analysis.

• 1.0 mL of dispersion was evaporated on a TGA pan, following the drop-casting technique, and analyzed by TGA a 100 °C in air.

• For each synthesized derivative, a TGA measurement was conducted in inert atmosphere on a small amount of dry nanostructure (1-2 mg).

3.2.12 Preparation of f-rGO dispersions

5 mg of f-rGO were dispersed in 2.5 mL of MilliQ water by treatment with tip sonicator for 1 min. The mixture was centrifuged at 2,000 rpm for 10 minutes and the supernatant was then recovered and filtered on cotton.

To conduct DLS, ZP and UV-Vis-NIR analysis the following samples were prepared:

• 100 µL of dispersion was added to 1.0 mL of MilliQ in water a plastic cuvette for DLS analysis.

• 100 µL of dispersion was added to 700 µL of MilliQ water and a 160 µL of a 1 mg/mL NaCl solution in a cell for analysis Zeta Potential.

• 100 µL of dispersion was added to 2.90 mL of MilliQ in water a quartz cuvette for UV-Vis-NIR analysis.

• 1.0 mL of dispersion was evaporated on a TGA pan, following the drop-casting technique, and analyzed by TGA a 100 °C in air.

• For each synthesized derivative, a TGA measurement was conducted in inert atmosphere on a small amount of dry nanostructure (1-2 mg).

3.2.12 Calculation of the dispersibility of nanostructures in water

To establish the quantity of nanostructure dissolved in the dispersion (see above), 1 mL of this is dried on a TGA pan using the technique of drop casting. A TGA measurement is then carried out setting an isotherm at 100 °C to remove any traces of solvent and determine the mass of dry CNS. Relating this value to analyzed volume, the dispersibility of the nanostructure is obtained.

3.2.13 Filtrations

The vacuum filtration operations were carried out using glass filter holders 47 mm Millipore from Merck. Isopore polycarbonate filters were used (pore size 0.1 μm, filter code VCTP04700).

3.2.14 SWCNH washing method

Raw pristine SWCNH (50 mg) were dispersed in the sonication bath in 25 mL of acetone, then the dispersion was filtered under vacuum with an isopore polycarbonate filter 0.1 μm and the SWCNH that remained on the filter were sonicated in 25 mL of acetone in the ultrasonic bath for 10 minutes. This procedure was repeated 2 times and the resulting purified SWCNH were then used for the functionalization reactions.

3.2.15 Raman instrument

In this work the instrument used was Renishaw Raman Microscope Model InVia equipped as 3 wavelengths (532, 633 and 785 nm), CCD detector and a LEICA optical microscope, model DM 2500 M and MS20 encoded motorized stage platform 100 nm. The laser wavelength used for all pristine CNS and CNS derivatives was 633.0 nm.

3.3 Synthesis and characterizations

3.3.1 Steps of the synthesis of 4-amino-N, N, N-trimethylbenzene ammonium iodide [69]

Step 1 – Synthesis of 2-(4-(dimethylamino) phenyl) isoindoline-1,3-dione (1)

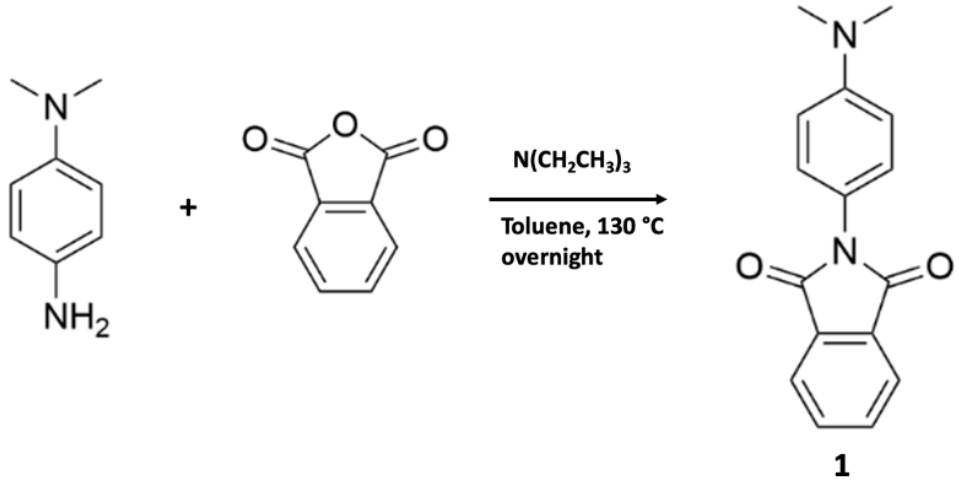

Figure 45: first step of the synthesis of 4-amino-N, N, N-trimethylbenzene ammonium iodide

Reagent	MM [g ·mol^{-1}]	d [g·mL^{-1}] 25 °C	Mass [g]	Volume [mL]	Moles [mmol]
Toluene	92.14	0.8650	/	100.0	/
Triethylamine	101.19	0.726	1.45	2.0	14.35
Phthalic anhydride	148.12	1.53	8.73	/	58.94
N, N-dimethylbenzene-1,4-diamine	136.19	/	4.02	/	29.52

Table 20: reagents and relative quantities for the first step of the synthesis of -amino-N, N, N-trimethylbenzene ammonium iodide

N, N-dimethylbenzene-1,4-diamine (4.02 g, 29.52 mmol), phthalic anhydride (8.73 g, 58.94 mmol) and triethylamine (2.0 mL) were dissolved in toluene (100 mL) in a Dean-Stark apparatus and maintained under magnetic stirring at 130 °C all night long. The mixture was then cooled and some of the solvent comes out removed by rotary evaporator. The formation of a precipitate is observed. It was filtered and washed several times with cold methanol until obtain a dark green solid.

The total mass of the product was of 6.82 g, giving a reaction yield of 86.8 %. ^{1}HNMR spectrum can be seen in the appendix in

Figure 57 (300 MHz, $CDCl_3$).

Step 2 – Synthesis of 4-(1,3-dioxoisoindolin-2-yl)-N, N, trimethylbenzenammonium, iodide (2)

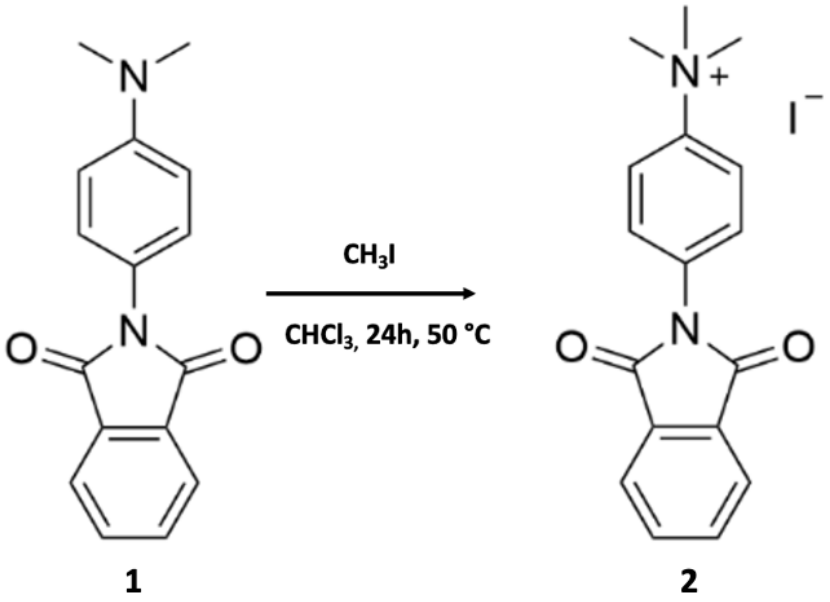

Figure 46: second step of the synthesis of 4-amino-N, N, N-trimethylbenzene ammonium iodide

Reagent	MM [g ·mol^{-1}]	d [g·mL^{-1}] 25 °C	Mass [g]	Volume [mL]	Moles [mmol]
2-(4-(dimethylamino) phenyl) isoindoline-1,3-dione	266.11	/	6.82	/	25.63
Chloroform (solvent)	119.38	1.4760	/	100	/
Methyl iodide	141.94	2.28	15.28	6.7	107.62

Table 21: reagents and relative quantities for the second step of the synthesis of 4-amino-N, N, N-trimethylbenzene ammonium iodide

In a Pyrex tube, 6.7 mL of methyl iodide were added to 6.82 g of 2-(4-(dimethylamino) phenyl) isoindolin 1,3-dione dissolved in 100 mL of chloroform. The mixture was heated for 24 hours at 50 °C. During the reaction precipitates the

product a little at a time. The product was filtered and washed with finely cold chloroform to obtain a light gray solid.

The total mass of the product was of 6.93 g, giving a reaction yield of 66.2 %. ^{1}HNMR spectrum can be seen in the appendix in

Figure *58* (300 MHz, d_6-DMSO).

Step 3 – Synthesis of 4-amino-N, N, N-trimethylbenzene ammonium iodide (3)

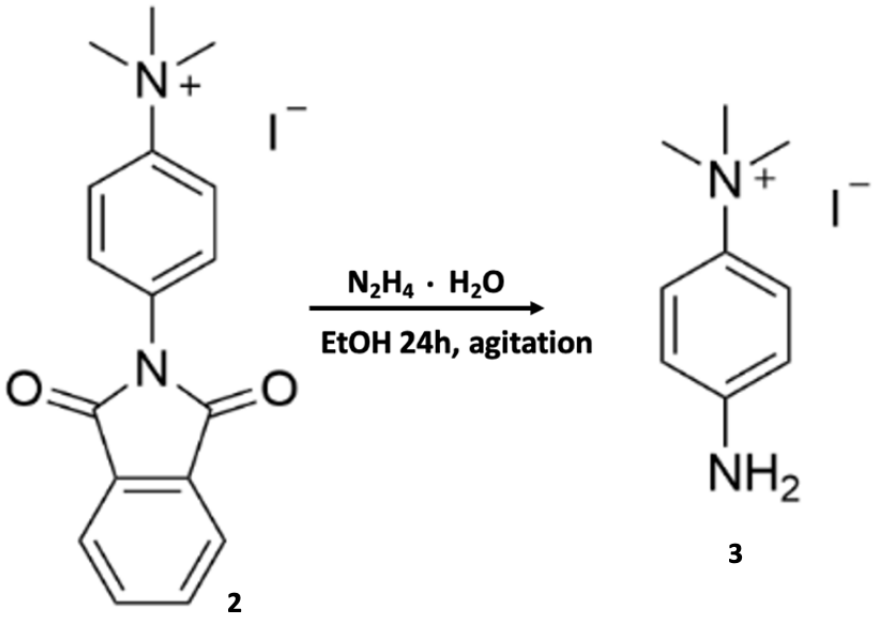

Figure 47: third step of the synthesis of 4-amino-N, N, N-trimethylbenzene ammonium iodide

Reagent	MM [g ·mol^{-1}]	d [g·mL^{-1}] 25 °C	Mass [g]	Volume [mL]	Moles [mmol]
Idrazine monohydrate	50.06	1.032	3.73	3.6	74.51
Ethanol	46.07	0.79	158.00	200	3.43
4-(1,3-dioxoisoindolin-2) -N, N, N-trimethylbenzenammonium iodide	408.24	/	6.00	/	14.70

Table 22: reagents and relative quantities for the third step of the synthesis of 4-amino-N, N, N-trimethylbenzene ammonium iodide

Hydrazine monohydrate (3.6 mL, 74.31 mmol) was added to a 4-(1,3-dioxoisoindolin-2-yl)-N, N, N-trimethylbenzenammonium suspension iodide (6.00

g, 14.70 mmol) in ethanol (200 mL). The mixture was stirred for 24 hours at room temperature and then filtered. The filtrate, containing the

final product was dried using a rotary evaporator. The solid obtained was recrystallized with ethanol and washed with cold EtOH. The product obtained was light purple solid.

The total mass of the product was of 2.62 g, giving a reaction yield of 64.3 %. ^{1}HNMR spectrum can be seen in the appendix in Figure 59 (300 MHz, d_6-DMSO).

3.3.2 Functionalization of SWCNH

Functionalization of SWCNH with benzene sulfonate (SWCNH-S)

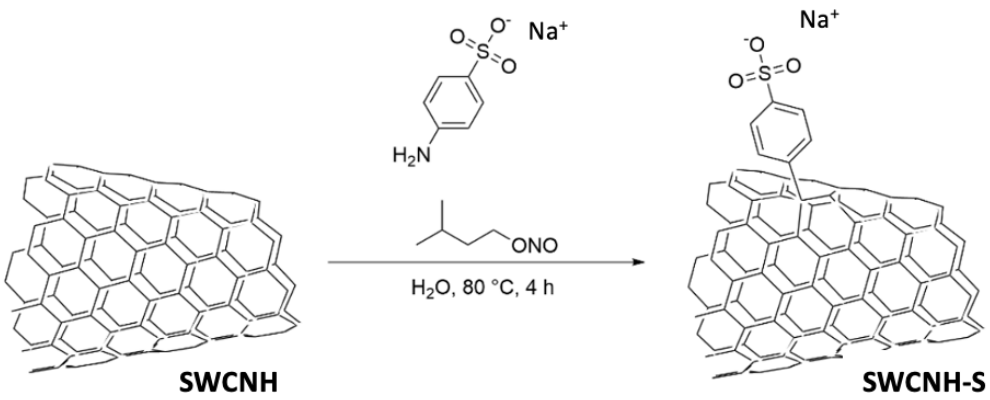

Figure 48: functionalization of SWCNH pristine with benzene sulfonate

Reagent	MM [g ·mol^{-1}]	d [g·mL^{-1}] 25 °C	Mass [mg]	Volume [mL]	Moles [mmol]
SWCNH	12.01	/	31.0	/	2.581
Sodium sulfanilate dihydrate	231.2	/	596.8	/	2.581
Isopenthyl nitrite	117.15	0.872	318.3	0.365	2.717
Methanol (solvent)	32.04	0.791	/	/	/
Milliq water (solvent)	18.01	0.997	/	/	/

Table 23: reagents needed for Tour reaction SWCNH-S

Pristine SWCNH (31.0 mg, 2.581 mmol) were introduced into a double-necked glass flask and sodium sulphanilate dihydrate (596.8 mg, 2.581 mmol) previously dissolved in 6.0 mL of MilliQ water. The mixture was heated to 80 °C in N_2 atmosphere under magnetic stirring. Subsequently isopentyl nitrite (0.365 mL) was added. After 4 hours, the reaction mixture was cooled to room temperature. The product was then recovered by filtration on Millipore PC 0.1 µm filters and it was washed six times with 25 mL of MilliQ water and one time with 25 mL of methanol. After each filtration, the filter was sonicated for 10 minutes in the ultrasonic bath. The functionalized SWCNH were finally removed from the filter by bath sonication in a small amount of methanol, then the dispersion was dried under N_2 flow and heating at the temperature of 30 °C.

Hydrodynamic diameter: 105.6 ± 0.7 nm
Polydispersion index: 0.146 ± 0.006
Zeta potential: -34.2 mV ± 1.1
Absorbance UV-Vis-NIR (1000 nm): 0.468
Dispersibility in water MilliQ: 1.457 mg/mL

Functionalization of SWCNH with methyl sulfonyl benzene (SWCNH-MeS)

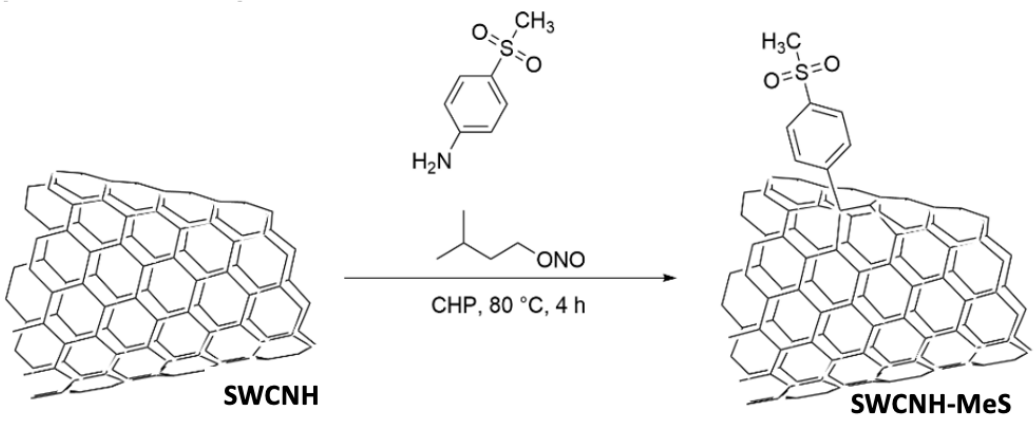

Figure 49: functionalization of SWCNH pristine with methyl sulfonyl benzene

Reagent	MM [g ·mol^{-1}]	d [g·mL^{-1}] 25 °C	Mass [mg]	Volume [mL]	Moles [mmol]
SWCNH	12.01	/	30.0	/	2.498
4-(methylsulfonyl) aniline	171.21	/	427.7	/	2.498
Isopenthyl nitrite	117.15	0.872	292.6	0.353	2.498
Methanol (solvent)	32.04	0.791	/	/	/
CHP (solvent)	167.25	1.007	/	/	/

Table 24: reagents needed for Tour reaction SWCNH-MeS

Pristine SWCNH (30.0 mg, 2.498 mmol) were introduced into a double-necked glass flask and 4-(methylsulfonyl) aniline (427.7 mg, 2.498 mmol) previously dissolved in 15 mL of CHP. The mixture was heated to 80°C in N_2 atmosphere under magnetic stirring. Subsequently isopentyl nitrite (0.353 mL, 2.498 mmol) was added. After 4 hours, the heating was stopped. At once the mixture was cooled to room temperature, the product was recovered by filtration on Durapore PVDF 0.1 µm and then it was washed and filtered six times with 25 mL of MilliQ water and one time with 25 mL of methanol by using Millipore PC 0.1 µm filter. After each filtration, the filter was sonicated for 10 minutes in the ultrasonic bath. The functionalized SWCNH were finally removed from the filter by bath sonication in a small amount of methanol, then the dispersion was dried under N_2 flow and heating at the temperature of 30 °C.

Functionalization of SWCNH with N, N, N-trimethylbenzenamonium (SWCNH-N)

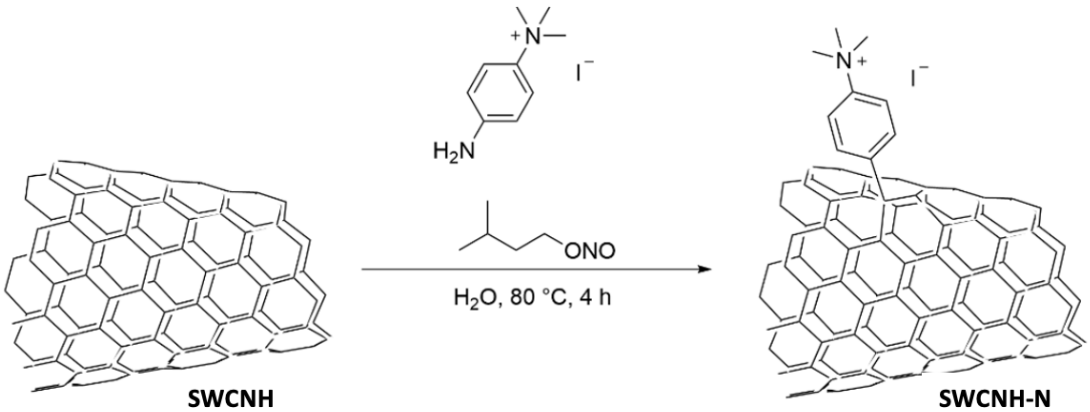

Figure 50: functionalization of SWCNH pristine with N, N, N-trimethylbenzenamonium

Reagent	MM [g ·mol^{-1}]	d [g·mL^{-1}] 25 °C	Mass [mg]	Volume [mL]	Moles [mmol]
SWCNH	12.01	/	30.0	/	2.498
4-amino-N, N, N-trimethylbenzene ammonium iodide	278.14	/	347.5	/	1.249
Isopenthyl nitrite	117.15	0.872	313.9	0.360	2.679
Methanol (solvent)	32.04	0.791	/	/	/
Water MilliQ (solvent)	18.01	0.997	/	/	/

Table 25: reagents needed for Tour reaction SWCNH-N

Pristine SWCNH (30.0 mg, 2.498 mmol of C) were introduced into a double-necked glass flask and 4-amino-N, N, N-trimethylbenzene ammonium iodide (347.5 mg, 1.249 mmol) previously dissolved in 15.0 mL of Milli Q water. The mixture was heated to 80 °C in N_2 atmosphere under magnetic stirring. Isopentyl nitrite (0.360 mL, 2.679 mmol) was subsequently added. After 4 hours, the reaction mixture was cooled to room temperature. The product was recovered by filtration on Millipore filters PC 0.1 µm and washed six times with 25 mL of MilliQ water and one time with 25 mL of MeOH. After each filtration, the filter was sonicated for 10 minutes in the ultrasonic bath. The functionalized SWCNH were finally removed from the filter by bath sonication in a small amount of methanol, then the dispersion was dried under N_2 flow and heating at the temperature of 30 °C.

Hydrodynamic diameter: 241.5 ± 5.0 nm
Polydispersion index: 0.315 ± 0.043
Zeta potential: +30.8 ± 0.4 mV
Absorbance UV-Vis-NIR (1000 nm): 0.298
Dispersibility in water MilliQ: 0.748 mg/mL

Functionalization of SWCNH with N-(p-aminobenzoyl) glycine (SWCNH-G)

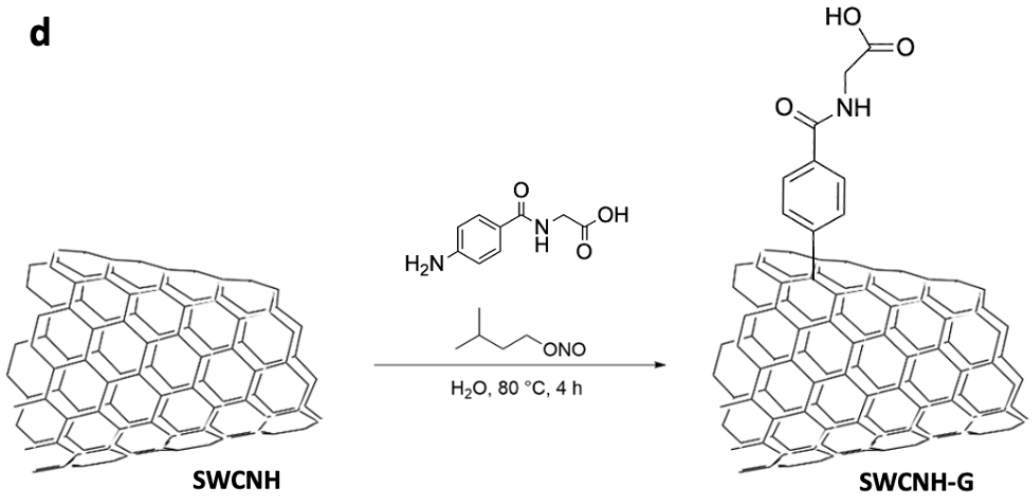

Figure 51: functionalization of SWCNH pristine with N-(p-aminobenzoyl) glycine

Reagent	MM [g ·mol^{-1}]	d [g·mL^{-1}] 25 °C	Mass [mg]	Volume [mL]	Moles [mmol]
SWCNH	12.01	/	30.0	/	2.498
Aminohippuric acid	194.190	/	485.1	/	2.498
Isopenthyl nitrite	117.15	0.872	292.6	0.353	2.498
Methanol (solvent)	32.04	0.791	/	/	/
Water MilliQ (solvent)	18.016	0.997	/	/	/

Table 26: reagents needed for Tour reaction SWCNH-G

Pristine SWCNH (30 mg, 2.498 mmol) were introduced into a double-necked glass flask and aminohippuric acid 458.1 mg, 2.498 mmol) previously dissolved in 35 mL of water. The mixture was heated to 80°C in N_2 atmosphere under magnetic stirring. Subsequently isopentyl nitrite (0.236 mL, 1.67 mmol) was added. After 4 hours, the reaction mixture was cooled to room temperature. The product was recovered by filtration on Millipore type GSWP 0.2 µm filter and washed six times with 25 mL of MilliQ water and one time with 25 mL of MeOH recovering on Millipore type GSWP 0.2 µm filter. After each filtration, the filter was sonicated for 10 minutes in the ultrasonic bath. The functionalized SWCNH were finally removed

from the filter by bath sonication in a small amount of methanol, then the dispersion was dried under N_2 flow and heating at the temperature of 30 °C.

Hydrodynamic diameter: 122.4 ± 0.5 nm
Polydispersion index: 0.146 ± 0.010
Zeta potential: -34.1 ± 0.6 mV
Absorbance UV-Vis-NIR (1000 nm): 0.462
Dispersibility in water MilliQ: 1.638 mg/mL

3.3.3 Functionalization of MWCNT

Functionalization of MWCNT with N-(p-aminobenzoyl) glycine (MWCNT-G)

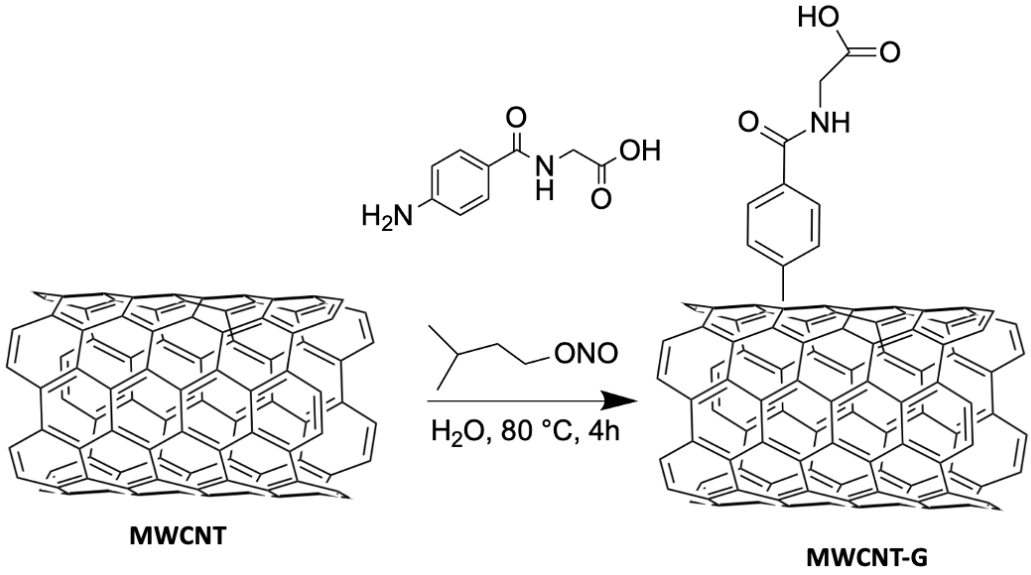

Figure 52: functionalization of MWCNT with N-(p-aminobenzoyl) glycine

Reagent	MM [g ·mol^{-1}]	d [g·mL^{-1}] 25 °C	Mass [mg]	Volume [mL]	Moles [mmol]
MWCNT	12.01	/	51.5	/	4.279
aminohippuric acid	194.190	/	415.5	/	2.139
Isopenthyl nitrite	117.15	0.872	501.3	0.605	4.279
Methanol (solvent)	32.04	0.791	/	/	/
Water MilliQ (solvent)	18.01	0.997	/	/	/

Table 27: reagents needed for Tour reaction MWCNT-G

Pristine MWCNT (51.4 mg, 4.279 mmol of C) were introduced into a double-necked glass flask and aminohippuric acid (415.5 mg, 2.139 mmol) previously dissolved in

20.0 mL of Milli Q water. The mixture was heated to 80 °C in N_2 atmosphere under magnetic stirring. Isopentyl nitrite (0.605 mL, 4.279 mmol) was subsequently added. After 4 hours, the reaction mixture was cooled to room temperature. The product was recovered by filtration on Millipore filters PC 0.1 µm and washed six times with 25 mL of MilliQ water and one time with 25 mL of MeOH. After each filtration, the filter was sonicated for 10 minutes in the ultrasonic bath. The functionalized MWCNT were finally removed from the filter by sonication in a small amount of methanol, then the dispersion was dried under N_2 flow and heating at the temperature of 30 °C.

Hydrodynamic diameter: 153.7 ± 5.4 nm
Polydispersion index: 0.305 ± 0.019
Zeta potential: -33.4 ± 0.6 mV
Absorbance UV-Vis-NIR (1000 nm): 0.088
Dispersibility in water MilliQ: 0.655 mg/mL

3.3.4 Functionalization of rGO

Functionalization of rGO with benzene sulfonate (rGO-S)

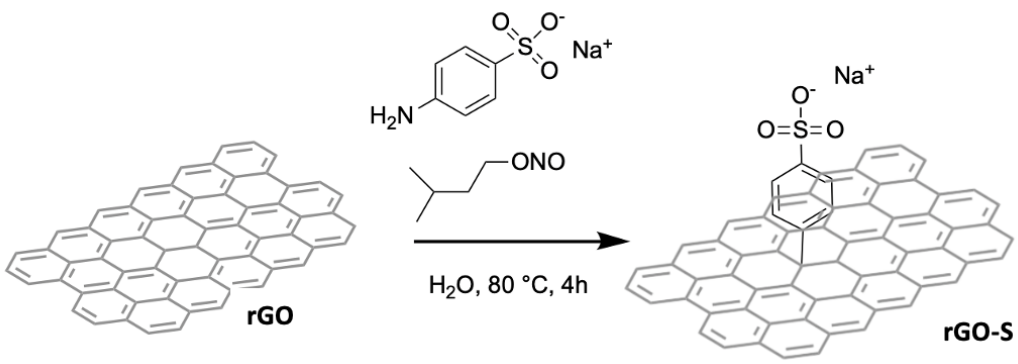

Figure 53: functionalization of rGO with sodium sulphanilate

Reagent	MM [g ·mol^{-1}]	d [g·mL^{-1}] 25 °C	Mass [mg]	Volume [mL]	Moles [mmol]
rGO	12.01	/	30.6	/	2.548
Sodium sulfanilate dihydrate	231.2	/	294.5	/	1.274
Isopenthyl nitrite	117.15	0.872	0.2985	0.360	2.548
Methanol (solvent)	32.04	0.791	/	/	/
Water MilliQ (solvent)	18.01	0.997	/	/	/

Table 28: reagents needed for Tour reaction rGO-S

Pristine rGO (30.6mg, 2.548 mmol of C) were introduced into a double-necked glass flask and sodium sulphanilate dihydrate (294.5 mg, 1.274 mmol) previously dissolved in 20.0 mL of Milli Q water. The mixture was heated to 80 °C in N_2 atmosphere under magnetic stirring. Isopentyl nitrite (0.360 mL, 2.548 mmol) was subsequently added. After 4 hours the reaction mixture was cooled to room temperature. The product was recovered by filtration on Millipore filters PC 0.1 µm and washed six times 25 mL of MilliQ water and one time with 25 mL of MeOH. After each filtration, the filter was sonicated for 10 minutes in the ultrasonic bath. The functionalized rGO was finally removed from the filter by bath sonication in a small amount of methanol, then the dispersion was dried under N_2 flow and heating at the temperature of 30 °C.

Hydrodynamic diameter: 350.5 ± 4.2 nm
Polydispersion index: 0.294 ± 0.025
Zeta potential: -40.2 ± 0.6 mV
Absorbance UV-Vis-NIR (1000 nm): 0.418
Dispersibility in water MilliQ: 0.690 mg/mL

Functionalization of rGO with methyl sulfonyl benzene (rGO-MeS)

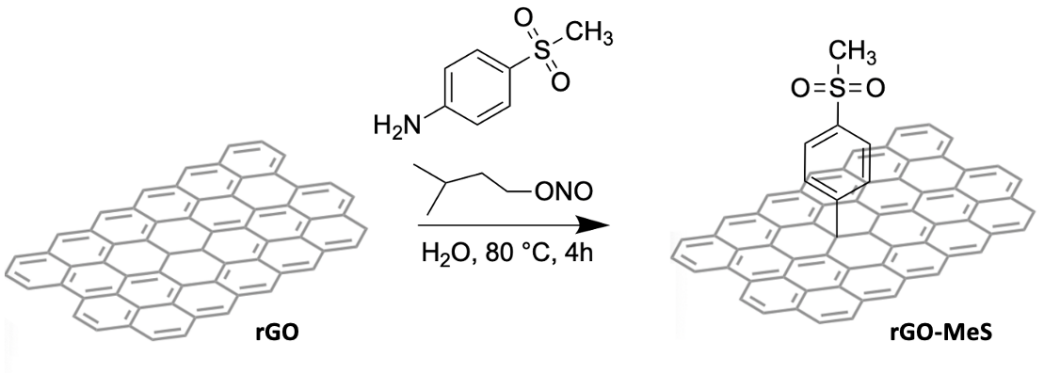

Figure 54: functionalization of rGO pristine with methyl sulfonyl benzene

Reagent	MM [g ·mol^{-1}]	d [g·mL^{-1}] 25 °C	Mass [mg]	Volume [mL]	Moles [mmol]
rGO	12.01	/	30.0	/	2.498
4-(methylsulfonyl) aniline	171.21	/	213.8	/	1.249
Isopenthyl nitrite	117.15	0.872	292.6	0.353	2.498
Methanol (solvent)	32.04	0.791	/	/	/
CHP (solvent)	167.25	1.007	/	/	/

Table 29: reagents needed for Tour reaction rGO-MeS

Pristine rGO (30 mg, 2.498 mmol) were introduced into a double-necked glass flask and 4-(methylsulfonyl) aniline (213.8 mg, 1.249 mmol) previously dissolved in X mL of CHP. The mixture was heated to 80°C in N_2 atmosphere under magnetic stirring. Subsequently isopentyl nitrite (0.353 mL, 2.498 mmol) was added. After 4 hours, the reaction mixture was cooled to room temperature. The product was recovered by filtration on Durapore PVDF 0.1 µm filter and then, after 10 minutes of sonicating bath, the product was washed and filtered six times with 25 mL of MilliQ water and one time with 25 mL of MeOH using Millipore filters PC 0.1 µm After each filtration, the filter was sonicated for 10 minutes in the ultrasonic bath. The functionalized rGO was finally removed from the filter by bath sonication in a small amount of methanol, then the dispersion was dried under N_2 flow and heating at the temperature of 30 °C.

Hydrodynamic diameter: 2427.8 ± 261.8 nm
Polydispersion index: 0.255 ± 0.098
Zeta potential: -20.9 ± 0.1 mV
Absorbance UV-Vis-NIR (1000 nm): 0.033
Dispersibility in water MilliQ: 0.117 mg/mL

Functionalization of rGO with N, N, N-trimethylbenzenamonium (rGO-N)

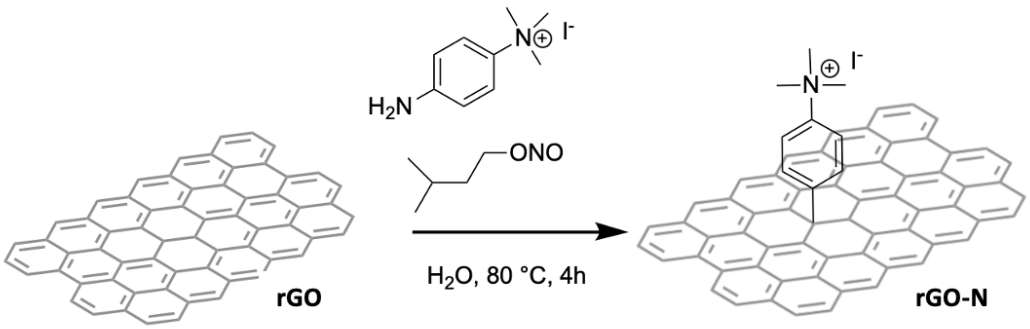

Figure 55: functionalization of rGO with N, N, N-trimethylbenzenamonium

Reagent	MM [g ·mol^{-1}]	d [g·mL^{-1}] 25 °C	Mass [mg]	Volume [mL]	Moles [mmol]
rGO	12.01	/	30.4	/	2.531
N, N, N-trimethylbenzenamo-nium	231.2	/	292.5	/	1.265
Isopenthyl nitrite	117.15	0.872	296.5	0.360	2.531
Methanol (solvent)	32.04	0.791	/	/	/
Water MilliQ (solvent)	18.01	0.997	/	/	/

Table 30: reagents needed for Tour reaction rGO-N

Pristine rGO (30.4 mg, 2.531 mmol of C) were introduced into a double-necked glass flask and N, N, N-trimethylbenzenamonium (352.1 mg, 1.265 mmol) previously dissolved in 15.0 mL of Milli Q water. The mixture was heated to 80 °C in N_2 atmosphere under magnetic stirring. Isopentyl nitrite (0.360mL, 835.4 mmol) was subsequently added. After 4 hours, the reaction mixture was cooled to room temperature. The product was recovered by filtration on Millipore filters PC 0.1 µm

and washed six times with 25 mL of MilliQ water and one time with 25 mL of MeOH. After each filtration, the filter was sonicated for 10 minutes in the ultrasonic bath. The functionalized rGO was finally removed from the filter by bath sonication in a small amount of methanol was added, then the dispersion was dried under N_2 flow and heating at the temperature of 30 °C.

Hydrodynamic diameter: 1545.0 ± 113.6 nm
Polydispersion index: 0.372 ± 0.099
Zeta potential: +32.1 ± 0.3 mV
Absorbance UV-Vis-NIR (1000 nm): 0.276
Dispersibility in water MilliQ: 0.313 mg/mL

Functionalization of rGO with N-(p-aminobenzoyl) glycine (rGO-G)

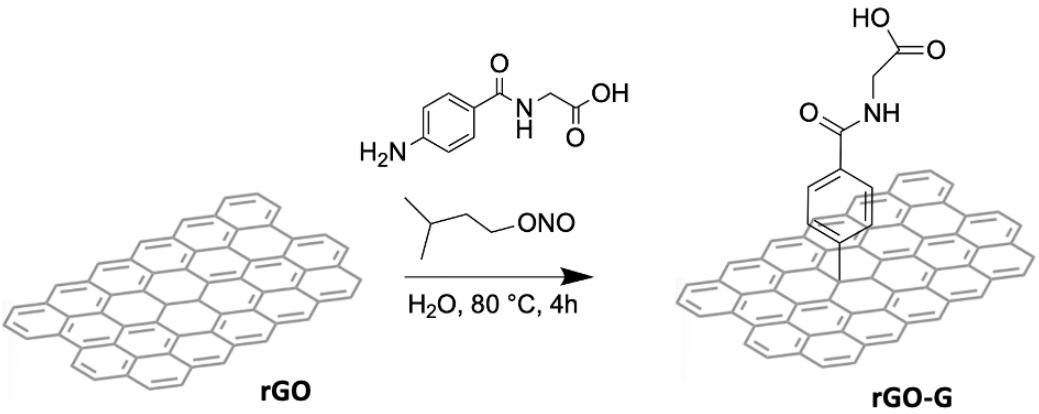

Figure 56: functionalization of rGO with N-(p-aminobenzoyl) glycine

Reagent	MM [g ·mol^{-1}]	d [g·mL^{-1}] 25 °C	Mass [mg]	Volume [mL]	Moles [mmol]
rGO	12.01	/	30.0	/	2.498
aminohippuric acid	194.190	/	242.5	/	1.249
Isopenthyl nitrite	117.15	0.872	292.5	0.353	2.497
Methanol (solvent)	32.04	0.791	/	/	/
Water milliq (solvent)	18.01	0.997	19.94	20.0	1.107

Table 31: reagents needed for Tour reaction rGO-G

Pristine rGO (30.0 mg, 2.497 mmol of C) were introduced into a double-necked glass flask and aminohippuric acid (242.5 mg, 1.249 mmol) previously dissolved in 20.0 mL of Milli Q water. The mixture was heated to 80 °C in N_2 atmosphere under magnetic stirring. Isopentyl nitrite (0.353 mL, 2.497 mmol) was subsequently added. After 4 hours, the reaction mixture was cooled to room temperature. The product was recovered by filtration on Millipore filters PC 0.1 µm and washed six times with 25 mL of MilliQ water and one time with 25 mL of MeOH. After each filtration, the filter was sonicated for 10 minutes in the ultrasonic bath. The functionalized rGO was finally removed from the filter by bath sonication in a small amount of methanol, then the dispersion was dried under N_2 flow and heating at the temperature of 30 °C.

Hydrodynamic diameter: 1055.0 ± 75.6 nm
Polydispersion index: 0.493 ± 0.074
Zeta potential: -25.8 ± 1.5 mV
Absorbance UV-Vis-NIR (1000 nm): 0.050
Dispersibility in water MilliQ: 0.202 mg/mL

References

1. Yu Y, Wang Q, Wang C, Shang L. Living Materials for Regenerative Medicine. *Engineered Regeneration*. 2021;2:96-104. Doi:10.1016/j.engreg.2021.08.003

2. Lee KY, Mooney DJ. Hydrogels for tissue engineering. *Chem Rev*. 2001;101(7):1869-1879. Doi:10.1021/cr000108x

3. El-Sherbiny IM, Yacoub MH. Hydrogel scaffolds for tissue engineering: Progress and challenges. *Glob Cardiol Sci Pract*. 2013;2013(3):38. Doi:10.5339/gcsp.2013.38

4. Khan MUA, Razak SIA, Arjan WS Al, et al. Recent advances in biopolymeric composite materials for tissue engineering and regenerative medicines: A review. *Molecules*. 2021;26(3). Doi:10.3390/molecules26030619

5. Hopley EL, Salmasi S, Kalaskar DM, Seifalian AM. Carbon nanotubes leading the way forward in new generation 3D tissue engineering. *Biotechnol Adv*. 2014;32(5):1000-1014. Doi:10.1016/j.biotechadv.2014.05.003

6. Pina S, Oliveira JM, Reis RL. Natural-based nanocomposites for bone tissue engineering and regenerative medicine: A review. *Advanced Materials*. 2015;27(7):1143-1169. Doi:10.1002/adma.201403354

7. Hu Y, Shenderova OA, Hu Z, Padgett CW, Brenner DW. Carbon nanostructures for advanced composites. *Reports on Progress in Physics*. 2006;69(6):1847-1895. Doi:10.1088/0034-4885/69/6/R05

8. Hale DK. *Review The Physical Properties of Composite Materials*. Vol 11.; 1976.

9. Gaur M, Misra C, Yadav AB, et al. Biomedical applications of carbon nanomaterials: Fullerenes, quantum dots, nanotubes, nanofibers, and graphene. *Materials*. 2021;14(20). Doi:10.3390/ma14205978

10. Sanchez-Garcia MD, Lagaron JM, Hoa S V. Effect of addition of carbon nanofibers and carbon nanotubes on properties of thermoplastic biopolymers. *Compos Sci Technol*. 2010;70(7):1095-1105. Doi:10.1016/j.compscitech.2010.02.015

11. Neves V, Gerondopoulos A, Heister E, et al. Cellular localization, accumulation and trafficking of double-walled carbon nanotubes in human prostate cancer cells. *Nano Res*. 2012;5(4):223-234. Doi:10.1007/s12274-012-0202-9

12. Vicentini N, Gatti T, Salerno M, et al. Effect of different functionalized carbon nanostructures as fillers on the physical properties of biocompatible poly(L-lactic acid) composites. *Mater Chem Phys*. 2018;214:265-276. Doi:10.1016/j.matchemphys.2018.04.042

13. Vicentini N, Gatti T, Salice P, et al. Covalent functionalization enables good dispersion and anisotropic orientation of multi-walled carbon nanotubes in a poly(l-lactic acid) electrospun nanofibrous matrix boosting neuronal differentiation. *Carbon N Y*. 2015;95:725-730. Doi:10.1016/j.carbon.2015.08.094

14. Velasquez Edoardo. *Idrogel Nanocompositi Biocompatibili a Base Di Nanotubi Di per Applicazioni Biomediche*. Master Degree Thesis, University of Padova; 2022.

15. Thakur VK, Thakur MK. Recent advances in green hydrogels from lignin: A review. *Int J Biol Macromol*. 2015;72:834-847. doi:10.1016/j.ijbiomac.2014.09.044

16. Ihara H, Takafuji M, Kuwahara Y. Polymer functionalization by luminescent supramolecular gels. *Polym J*. 2016;48(8):843-853. doi:10.1038/pj.2016.53

17. Slaughter B V., Khurshid SS, Fisher OZ, Khademhosseini A, Peppas NA. Hydrogels in regenerative medicine. *Advanced Materials*. 2009;21(32-33):3307-3329. doi:10.1002/adma.200802106

18. Bratovcic A. Nanocomposite Hydrogels Reinforced by Carbon Nanotubes. *International Journal of Engineering Research and Applications www.ijera.com*. 2020;10:30-41. doi:10.9790/9622-1005043041

19. Drury JL, Mooney DJ. Hydrogels for tissue engineering: Scaffold design variables and applications. *Biomaterials*. 2003;24(24):4337-4351. doi:10.1016/S0142-9612(03)00340-5

20. Yuan X, Zhang X, Sun L, Wei Y, Wei X. Cellular Toxicity and Immunological Effects of Carbon-based Nanomaterials. *Part Fibre Toxicol*. 2019;16(1). doi:10.1186/s12989-019-0299-z

21. Liu H, Zhang L, Yan M, Yu J. Carbon nanostructures in biology and medicine. *J Mater Chem B*. 2017;5(32):6437-6450. doi:10.1039/c7tb00891k

22. Serban BC, Buiu O, Bumbac M, et al. Ternary Oxidized Carbon Nanohorns/TiO2/PVP Nanohybrid as Sensitive Layer for Chemoresistive Humidity Sensor. In: MDPI AG; 2021:12. doi:10.3390/csac2021-10616

23. Zhang Z, Han S, Wang C, Li J, Xu G. Single-walled carbon nanohorns for energy applications. *Nanomaterials*. 2015;5(4):1732-1755. doi:10.3390/nano5041732

24. Karousis N, Suarez-Martinez I, Ewels CP, Tagmatarchis N. Structure, Properties, Functionalization, and Applications of Carbon Nanohorns. *Chem Rev*. 2016;116(8):4850-4883. doi:10.1021/acs.chemrev.5b00611

25. Cioffi C, Campidelli S, Brunetti FG, Meneghetti M, Prato M. Functionalisation of carbon nanohorns. *Chemical Communications*. 2006;(20):2129-2131. doi:10.1039/b601176d

26. Keren LB, Hanein Y. Carbon nanotube based multi electrode arrays for neuronal interfacing: Progress and prospects. *Front Neural Circuits*. 2012;(DEC). doi:10.3389/fncir.2012.00122

27. Ma PC, Siddiqui NA, Marom G, Kim JK. Dispersion and functionalization of carbon nanotubes for polymer-based nanocomposites: A review. *Compos Part A Appl Sci Manuf*. 2010;41(10):1345-1367. doi:10.1016/j.compositesa.2010.07.003

28. Arora N, Sharma NN. Arc discharge synthesis of carbon nanotubes: Comprehensive review. *Diam Relat Mater*. 2014;50:135-150. doi:10.1016/j.diamond.2014.10.001

29. Tasis D, Tagmatarchis N, Bianco A, Prato M. Chemistry of carbon nanotubes. *Chem Rev*. 2006;106(3):1105-1136. doi:10.1021/cr050569o

30. Niyogi S, Hamon MA, Hu H, et al. Chemistry of single-walled carbon nanotubes. *Acc Chem Res*. 2002;35(12):1105-1113. doi:10.1021/ar010155r

31. Chen Z, Thiel W, Hirsch A. Reactivity of the convex and concave surfaces of single-walled carbon nanotubes (SWCNTs) towards addition reactions: Dependence on the carbon-atom pyramidalization. *ChemPhysChem*. 2003;4(1):93-97. doi:10.1002/cphc.200390015

32. Reali Dimitri. Grafene: Sintesi, proprietà e applicazioni. Master Degree Thesis, University of Bologna; 2013.

33. Balandin AA, Ghosh S, Bao W, et al. Superior thermal conductivity of single-layer graphene. *Nano Lett*. 2008;8(3):902-907. doi:10.1021/nl0731872

34. Changgu Lee XW, JWKJH. Measurement of the Elastic Properties and Intrinsic Strength of Monolayer Graphene. *Science (1979)*. 2008;321(5887):382-385. doi:10.1126/science.1156211

35. Huang X, Yin Z, Wu S, et al. Graphene-based materials: Synthesis, characterization, properties, and applications. *Small*. 2011;7(14):1876-1902. doi:10.1002/smll.201002009

36. Bellet P, Gasparotto M, Pressi S, et al. Graphene-based scaffolds for regenerative medicine. *Nanomaterials*. 2021;11(2):1-41. doi:10.3390/nano11020404

37. Wick P, Louw-Gaume AE, Kucki M, et al. Classification framework for graphene-based materials. *Angewandte Chemie - International Edition*. 2014;53(30):7714-7718. doi:10.1002/anie.201403335

38. Roy-Mayhew JD, Aksay IA. Graphene materials and their use in dye-sensitized solar cells. *Chem Rev*. 2014;114(12):6323-6348. doi:10.1021/cr400412a

39. Dyke CA, Tour JM. Overcoming the Insolubility of Carbon Nanotubes Through High Degrees of Sidewall Functionalization. *Chemistry - A European Journal*. 2004;10(4):812-817. doi:10.1002/chem.200305534

40. Stephenson JJ, Sadana AK, Higginbotham AL, Tour JM. Highly functionalized and soluble multiwalled carbon nanotubes by reductive alkylation and arylation: The billups reaction. *Chemistry of Materials*. 2006;18(19):4658-4661. doi:10.1021/cm060832h

41. Salice P, Fabris E, Sartorio C, et al. An insight into the functionalisation of carbon nanotubes by diazonium chemistry: Towards a controlled decoration. *Carbon N Y*. 2014;74:73-82. doi:10.1016/j.carbon.2014.02.084

42. Lipińska ME, Rebelo SLH, Pereira MFR, Gomes JANF, Freire C, Figueiredo JL. New insights into the functionalization of multi-walled carbon nanotubes with aniline derivatives. *Carbon N Y*. 2012;50(9):3280-3294. doi:10.1016/j.carbon.2011.12.018

43. Azami T, Kasuya D, Yuge R, et al. Large-scale production of single-wall carbon nanohorns with high purity. *Journal of Physical Chemistry C*. 2008;112(5):1330-1334. doi:10.1021/jp076365o

44. Alafogianni P, Dassios K, Farmaki S, Antiohos SK, Matikas TE, Barkoula NM. On the efficiency of UV-vis spectroscopy in assessing the dispersion quality in sonicated aqueous suspensions of carbon nanotubes. *Colloids Surf A Physicochem Eng Asp*. 2016;495:118-124. doi:10.1016/j.colsurfa.2016.01.053

45. Bhattacharjee S. DLS and zeta potential - What they are and what they are not? *Journal of Controlled Release*. 2016;235:337-351. doi:10.1016/j.jconrel.2016.06.017

46. Shin US, Knowles JC, Kim HW. Positive charge-doping on carbon nanotube walls and anion-directed tunable dispersion of the derivatives. *Bull Korean Chem Soc*. 2011;32(5):1635-1639. doi:10.5012/bkcs.2011.32.5.1635

47. Orlando A, Franceschini F, Muscas C, et al. A comprehensive review on Raman spectroscopy applications. *Chemosensors*. 2021;9(9). doi:10.3390/chemosensors9090262

48. Moore BD, Stevenson L, Watt A, et al. Rapid and ultra-sensitive determination of enzyme activities using surface-enhanced resonance Raman scattering. *Nat Biotechnol*. 2004;22(9):1133-1138. doi:10.1038/nbt1003

49. Tiziana Cioffi Chiarmo Maurizio Fermeglia C, Chiarmo Maurizio Prato S. *UNIVERSITÀ DEGLI STUDI DI TRIESTE Sede Amministrativa Del Dottorato Di Ricerca XX CICLO DEL DOTTORATO DI RICERCA IN NANOTECNOLOGIE Functionalization and Application of Carbon Nanohorns and Carbon Onions Dottorando Coordinatore Del Collegio Dei Docenti*.

50. *The Raman Spectroscopy of Graphene and the Determination of Layer Thickness*.

51. Fisher Scientific T. *Characterizing Graphene with Raman Spectroscopy*.; 2019.

52. Kędzierski K, Rytel K, Barszcz B, Majchrzycki Ł. Single-Wall Carbon Nanohorn Langmuir-Schaefer Films. *Langmuir*. 2023;39(34):12124-12131. doi:10.1021/acs.langmuir.3c01396

53. Dendisová M, Jeništová A, Parchaňská-Kokaislová A, Matějka P, Prokopec V, Švecová M. The use of infrared spectroscopic techniques to characterize

nanomaterials and nanostructures: A review. *Anal Chim Acta*. 2018;1031:1-14. doi:10.1016/j.aca.2018.05.046

54. Di Laurea T. *UNIVERSITÁ DEGLI STUDI DI PADOVA FACOLTÁ DI SCIENZE MM.FF.NN. CORSO DI LAUREA SPECIALISTICA IN CHIMICA Synthesis and Characterization of Single Wall Carbon Nanotubes-Pyrene Derivatives*.; 2009.

55. Caccamo MT, Mavilia G, Magazù S. Thermal investigations on carbon nanotubes by spectroscopic techniques. *Applied Sciences (Switzerland)*. 2020;10(22):1-11. doi:10.3390/app10228159

56. Sarode VB, Patil RD, Chaudhari GE. Characterization of functionalized multi-walled carbon nanotubes. *Mater Today Proc*. Published online July 2023. doi:10.1016/j.matpr.2023.06.288

57. Alussail FA. *Synthesis and Characterization of Reduced Graphene Oxide Films*.; 2015.

58. Yan L, Niu X, Wen Z, Li X, Li X, Sun W. Application of single-walled carbon nanohorn modified electrode for the direct electrochemistry of myoglobin. *Int J Electrochem Sci*. 2016;11(11):8972-8980. doi:10.20964/2016.11.02

59. Kumar D, Singh K, Verma V, Bhatti HS. *INVESTIGATION OF PRISTINE AND FUNCTIONALIZED SINGLE-WALLED CARBON NANOHORNS FOR PHOSPHOR APPLICATIONS*. Vol 9.

60. Brun Maria Linda. Studio di materiali a base di nanostrutture di carbonio per applicazioni biomediche. Master Degree Thesis. University of Padova; 2023.

61. Crumrine DS; SJM; HRVTJOOC 1986, 5013 5015. *The Journal Of Organic Chemistry*. Vol 51. Academic; 1986.

62. The Role of Renal System in Acid (docx) - Course Sidekick. Karatina University. 2024. Accessed April 24, 2024. https://www.coursesidekick.com/medicine/6621497

63. Firme CP, Bandaru PR. Toxicity issues in the application of carbon nanotubes to biological systems. *Nanomedicine*. 2010;6(2):245-256. doi:10.1016/j.nano.2009.07.003

64. Yang B, Ren L, Li L, Tao X, Shi Y, Zheng Y. The characterization of the concentration of the single-walled carbon nanotubes in aqueous

dispersion by UV-Vis-NIR absorption spectroscopy. doi:10.1039/c3an01129a

65. Valentini F, Ciambella E, Boaretto A, et al. Sensor Properties of Pristine and Functionalized Carbon Nanohorns. *Electroanalysis*. 2016;28(10):2489-2499. doi:10.1002/elan.201501171

66. Agresti F, Barison S, Famengo A, et al. Surface oxidation of single wall carbon nanohorns for the production of surfactant free water-based colloids. *J Colloid Interface Sci*. 2018;514:528-533. doi:10.1016/j.jcis.2017.12.058

67. Le GTT, Lerkprasertkun P, Sano N, Wu KCW, Charinpanitkul T. Carbon nanohorns with surface functionalized by plasma treatment and their applications in drug delivery systems. *Journal of Science: Advanced Materials and Devices*. 2023;8(3). doi:10.1016/j.jsamd.2023.100616

68. Mendoza DJ, Hossain L, Browne C, Raghuwanshi VS, Simon GP, Garnier G. Controlling the transparency and rheology of nanocellulose gels with the extent of carboxylation. *Carbohydr Polym*. 2020;245. doi:10.1016/j.carbpol.2020.116566

69. Hadad C, Ke X, Carraro M, et al. Positive graphene by chemical design: Tuning supramolecular strategies for functional surfaces. *Chemical Communications*. 2014;50(7):885-887. doi:10.1039/C3CC47056C

Appendix

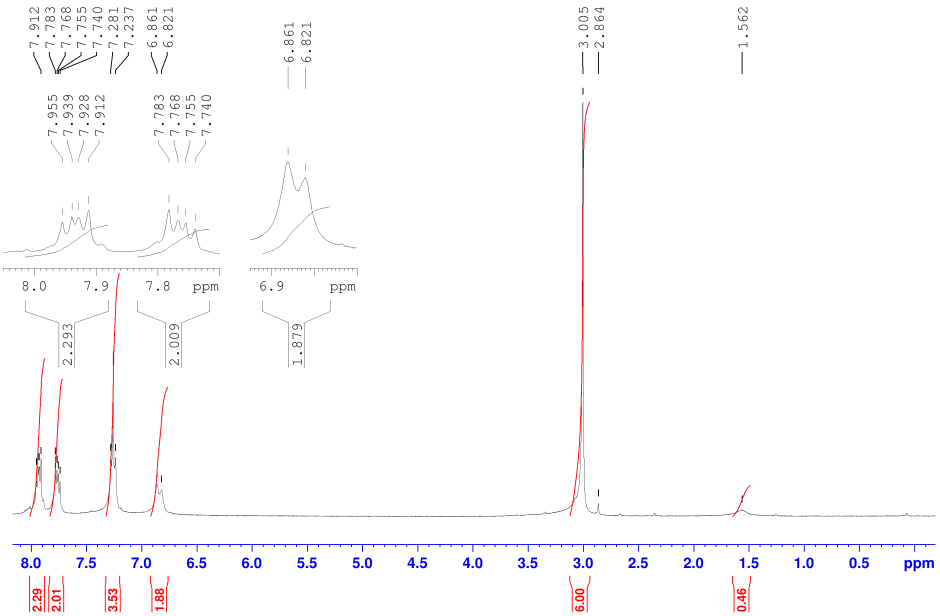

Figure 57: ^{1}HNMR spectrum of 2-(4-(dimethylamino) phenyl) isoindoline-1,3-dione, 300 MHz, $CDCl_3$

δ (ppm)	Multiplet type	Integrals	Comments
1.562	s	0.46	water
3.005	s	6.00	6H
6.821-6.861	d	1.879	2H
7.26	s	/	Solvent peak ($CDCl_3$)
7.740-7.783	m	2.009	2H
7.912-7.955	m	2.293	2H

Table 32: peaks and integral information of ^{1}HNMR spectrum of 2-(4-(dimethylamino) phenyl) isoindoline-1,3-dione

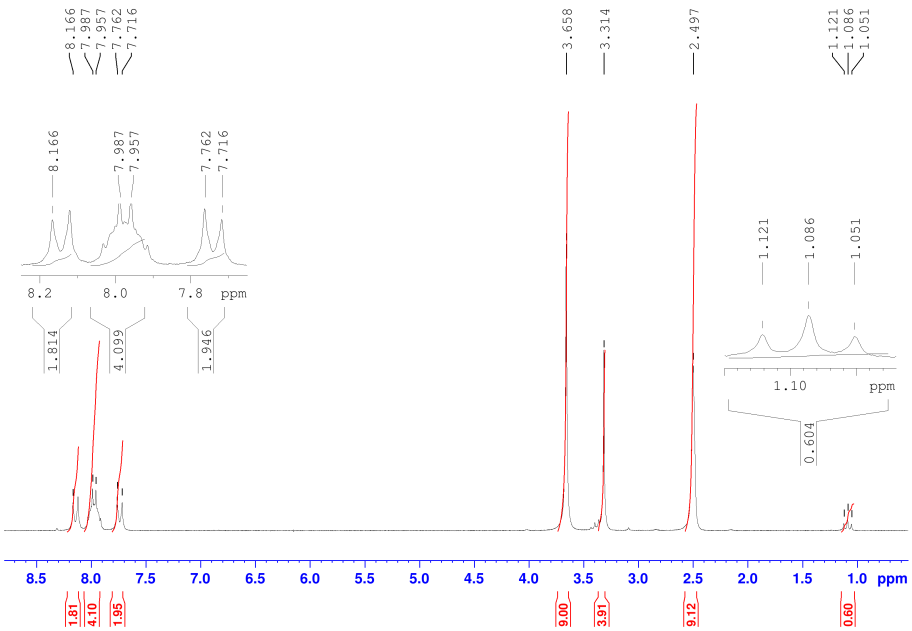

Figure 58: [1]HNMR spectrum of 4-(1,3-dioxoisoindolin-2-yl)-N, N, N-trimethylbenzeneaminiumiodide, 300 MHz, d_6-DMSO

δ (ppm)	Multiplet type	Integrals	Comments
1.051-1.121	t	0.604	Ethanol
2.497	s	9.12	Solvent peak (d_6-DMSO)
3.314	s	3.91	water
3.658	s	9.00	9H
7.716-7.762	d	1.95	2H
7.957-7.987	m	4.10	4H
8.166	d	1.81	2H

Table 33: peaks and integrals information of [1]HNMR spectrum of 4-(1,3-dioxoisoindolin-2-yl)-N, N, N-trimethylbenzeneaminiumiodide

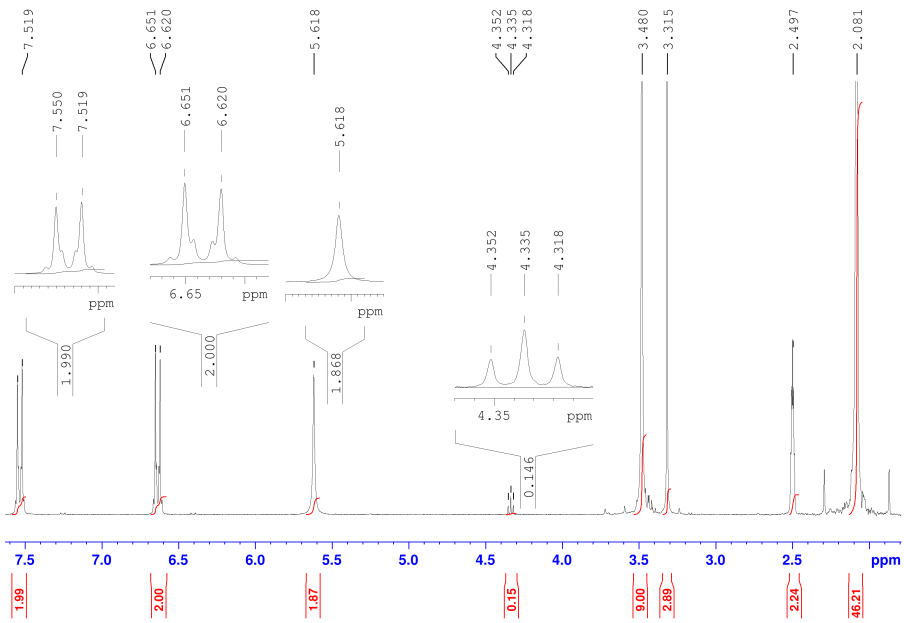

Figure 59: [1]HNMR spectrum of 4-amino-N, N, N-trimethylbenzeneammoniumiodide, 300 MHz, d_6-DMSO

δ (ppm)	Multiplet type	Integrals	Comments
2.081	s	46.21	Acetone
2.497	s	2.24	Solvent peak (d_6-DMSO)
3.315	s	2.89	Water
3.480	s	9.00	9H
4.318-4.352	t	0.15	Coupling of -OH with -CH_2 of the ethanol
5.618	s	1.87	2H
6.620-6.651	d	2.00	2H
7.519-7.550	d	1.99	2H

Table 34: peaks and integrals information of [1]HNMR spectrum of 4-amino-N, N, N-trimethylbenzeneammoniumiodide

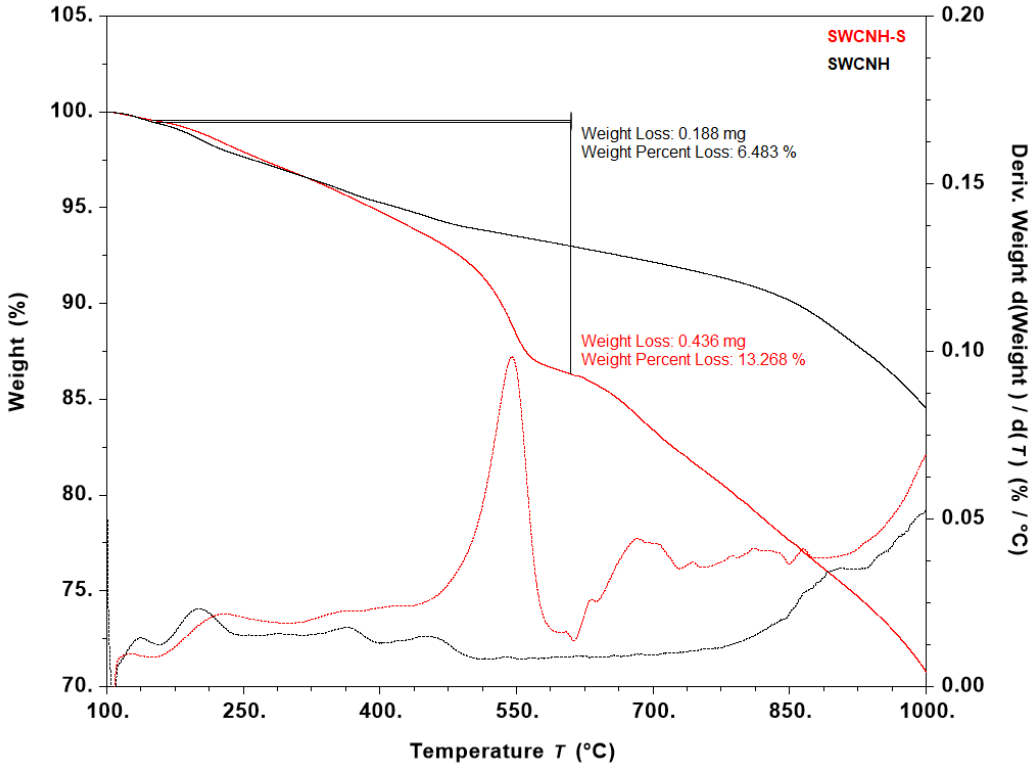

Figure 60: TGA overlap of SWCNH and SWCNH-S in N_2 atmosphere with the relative weight loss percentages

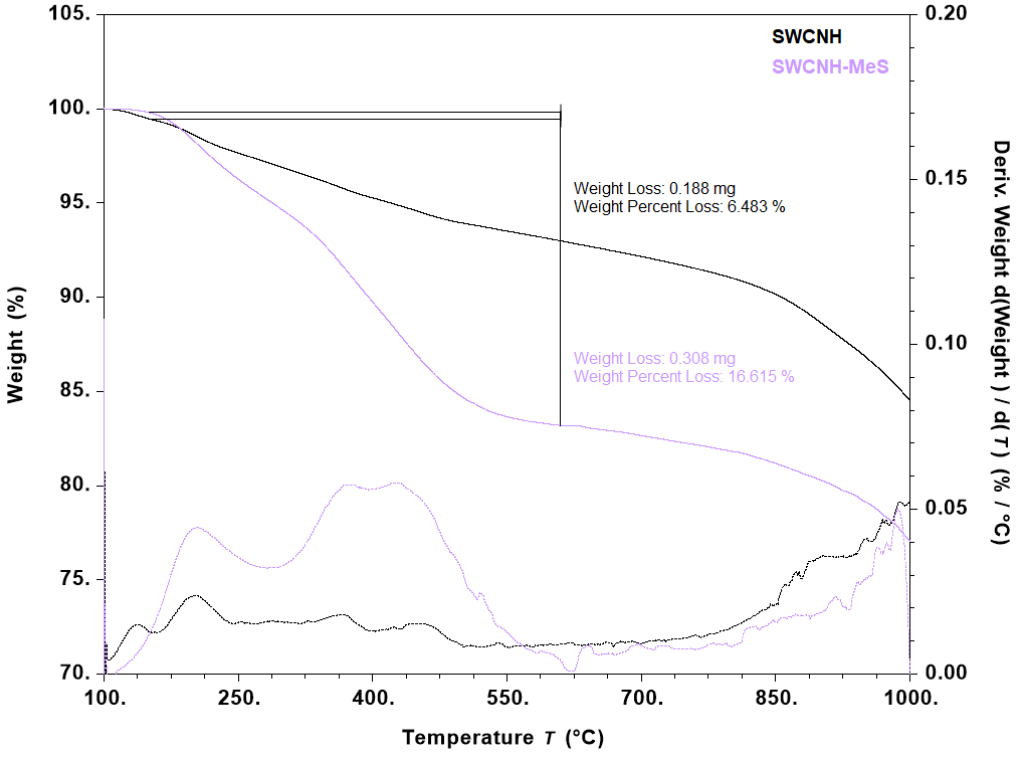

Figure 61: TGA overlap of SWCNH and SWCNH-MeS in N_2 atmosphere with the relative weight loss percentages

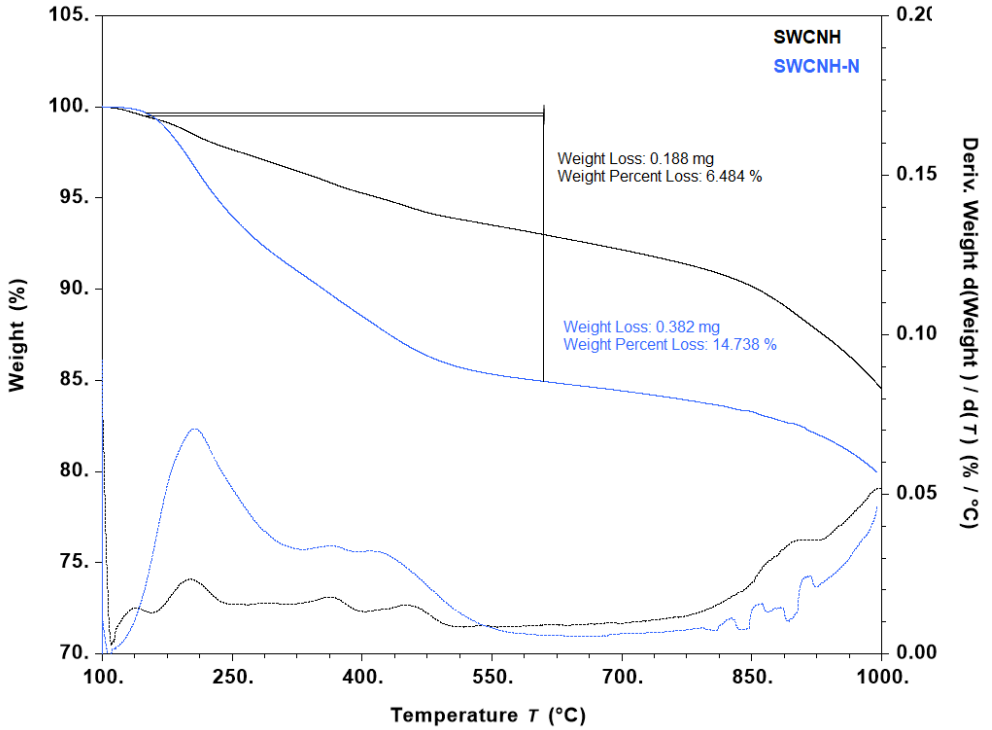

Figure 62: TGA overlap of SWCNH and SWCNH-N in N_2 atmosphere with the relative weight loss percentages

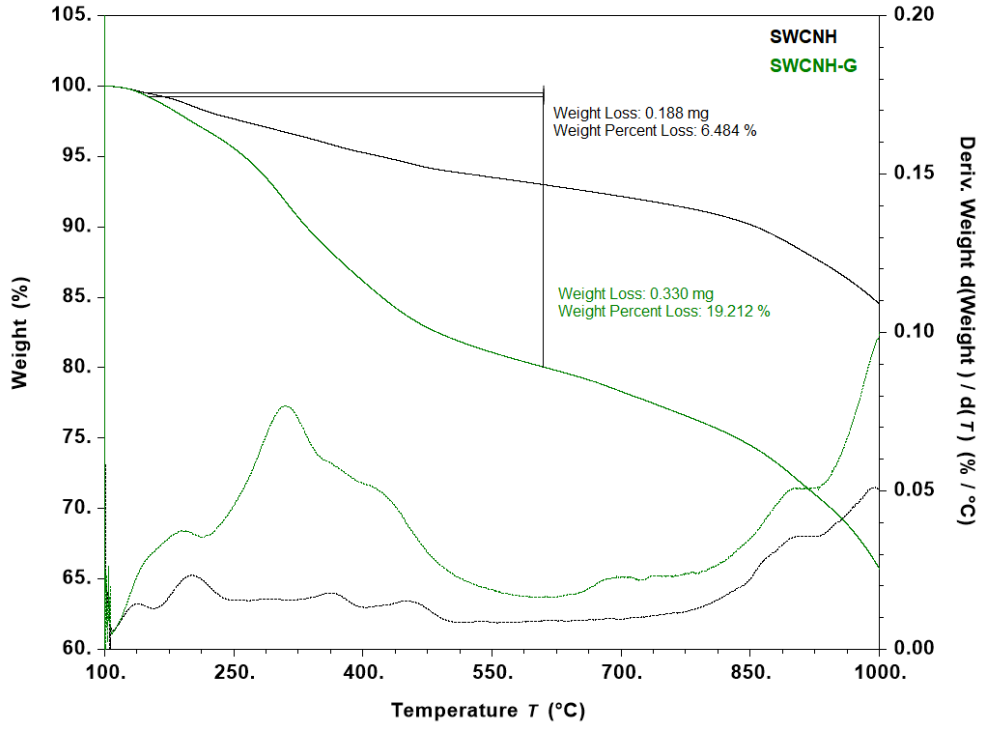

Figure 63: TGA overlap of SWCNH and SWCNH-G in N_2 atmosphere with the relative weight loss percentages

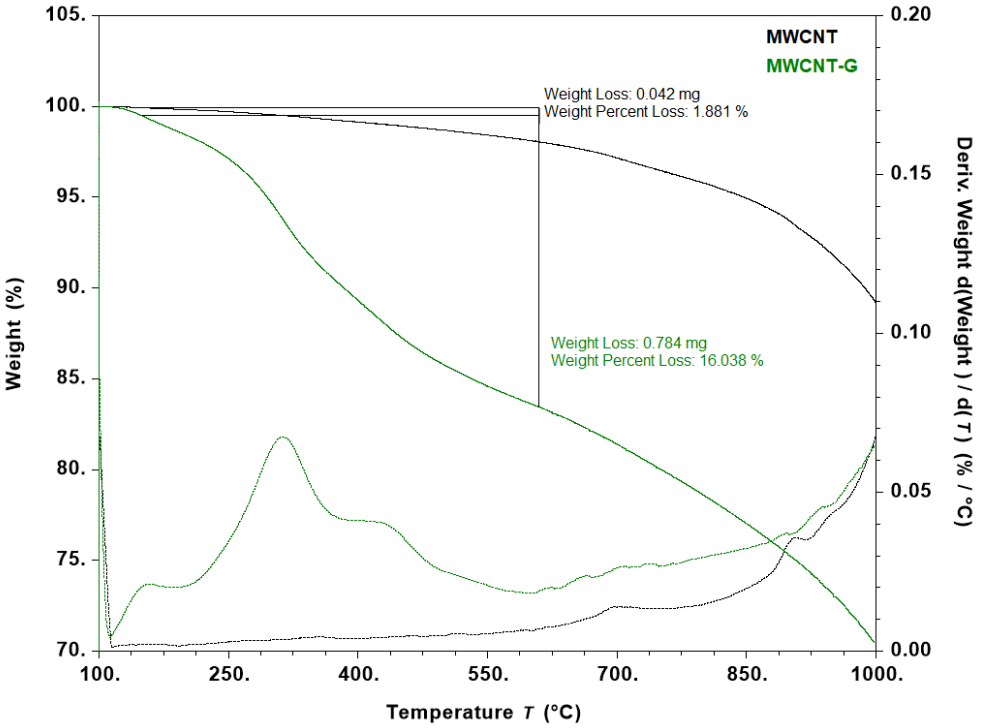

Figure 64: TGA overlap of MWCNT and MWCNT-G in N_2 atmosphere with the relative weight loss percentages

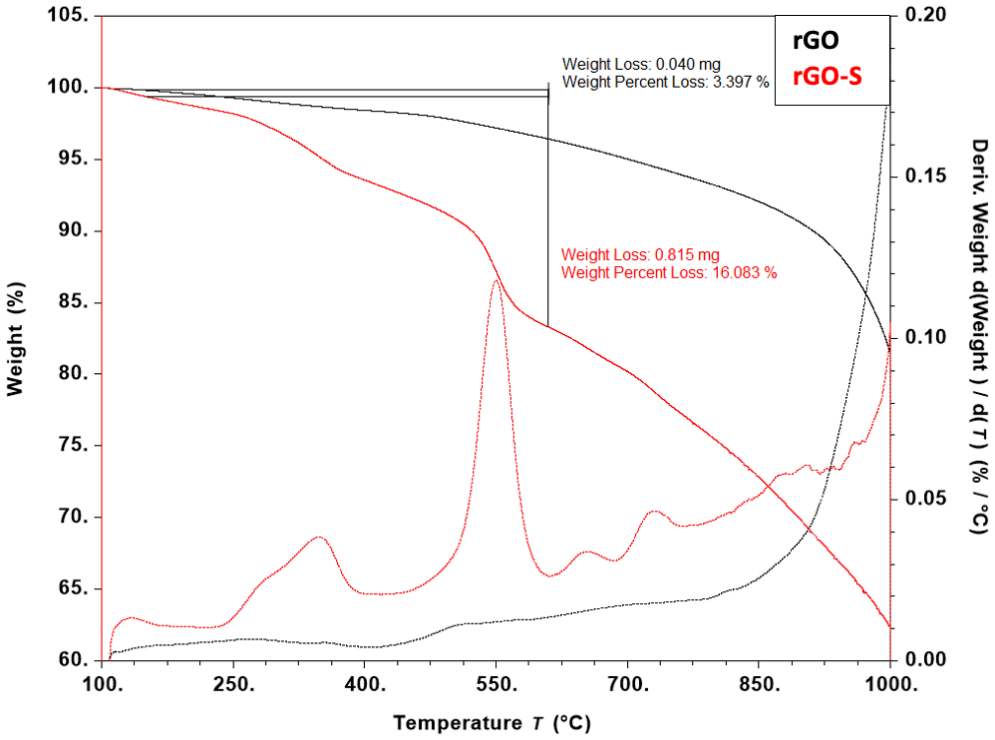

Figure 65: TGA overlap of rGO and rGO-S in N_2 atmosphere with the relative weight loss percentages

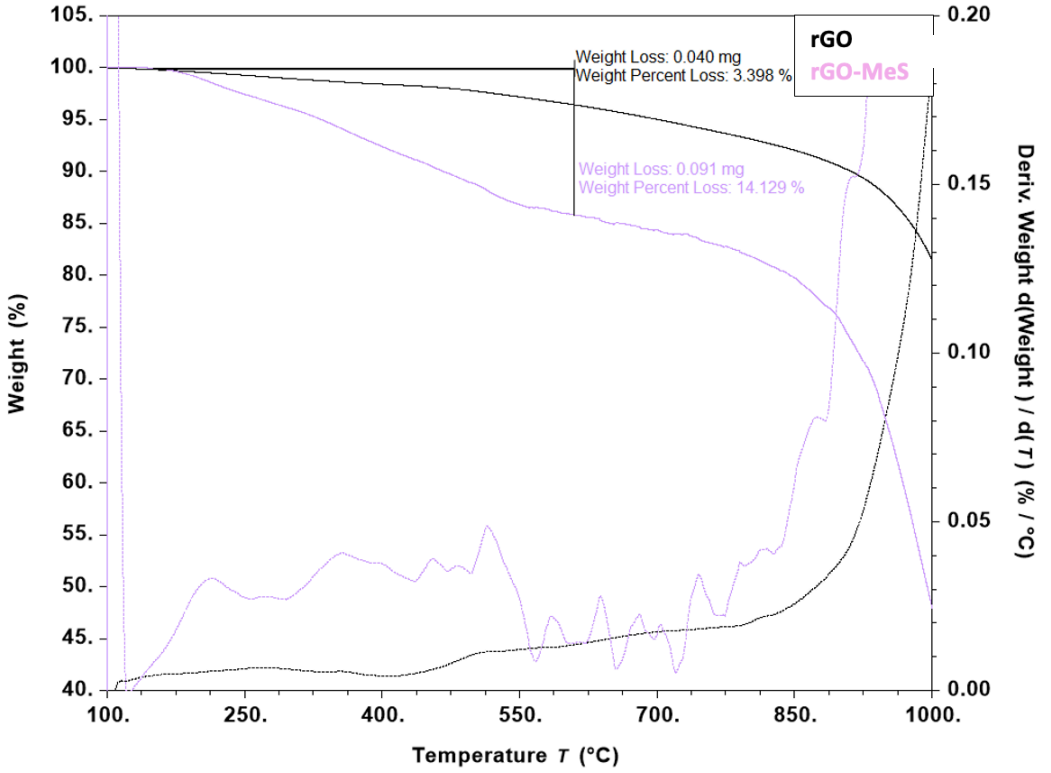

Figure 66: TGA overlap of rGO and rGO-MeS in N_2 atmosphere with the relative weight loss percentages

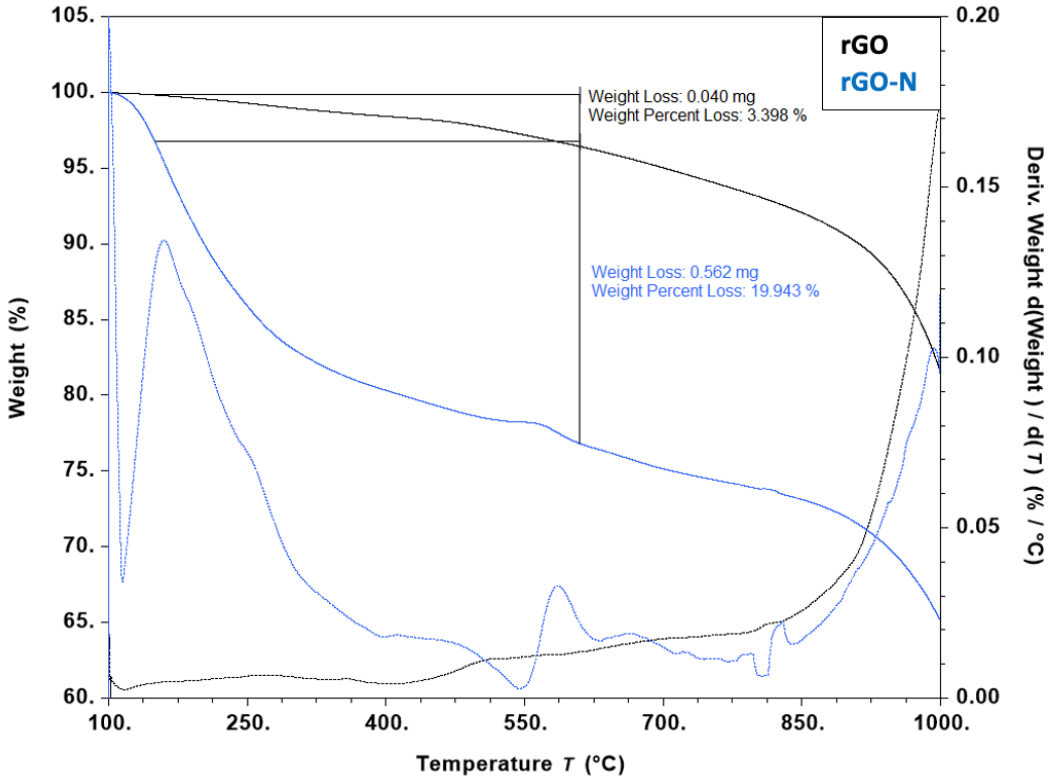

Figure 67: TGA overlap of rGO and rGO-N in N_2 atmosphere with the relative weight loss percentages

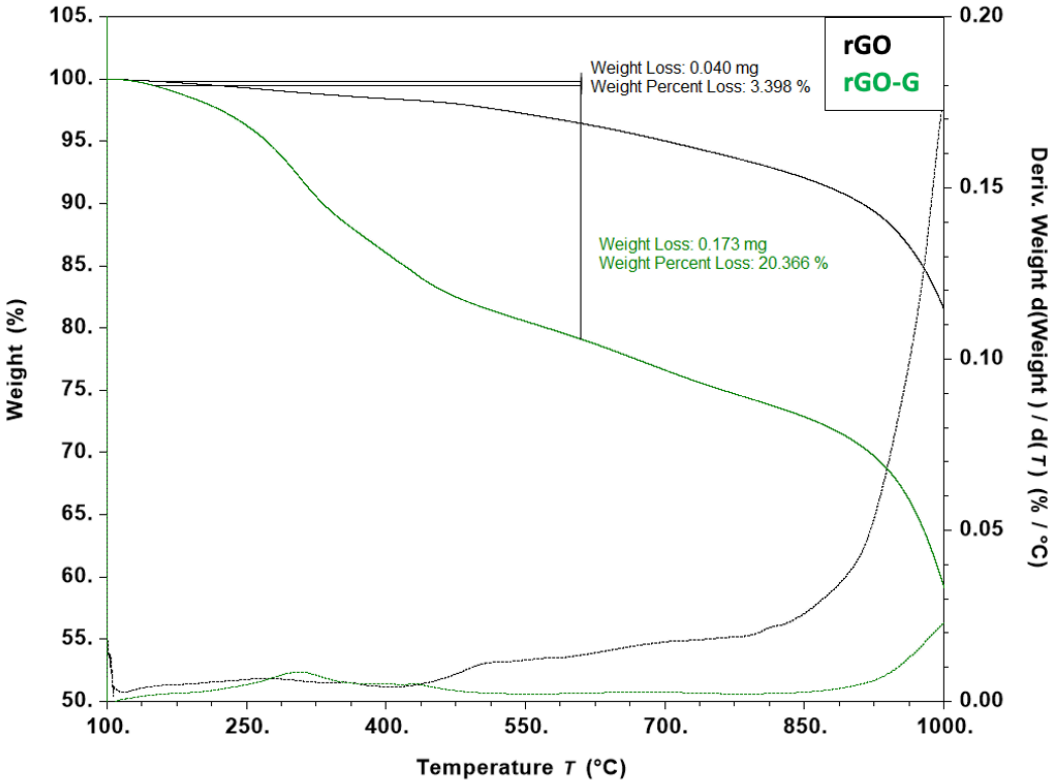

Figure 68: TGA overlap of rGO and rGO-G in N_2 atmosphere with the relative weight loss percentages

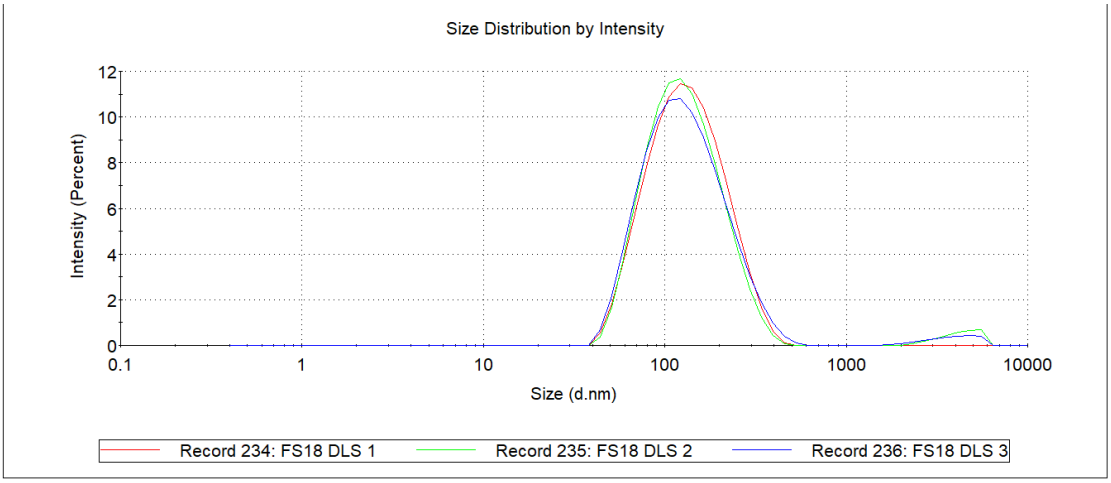

Figure 69: DLS measures of SWCNH-S in H_2O

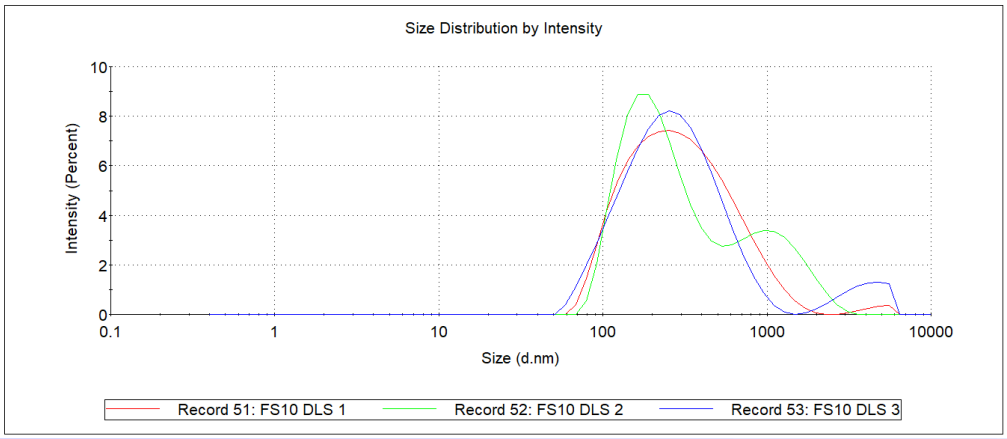

[Figure 70: DLS measures of SWCNH-N in H_2O

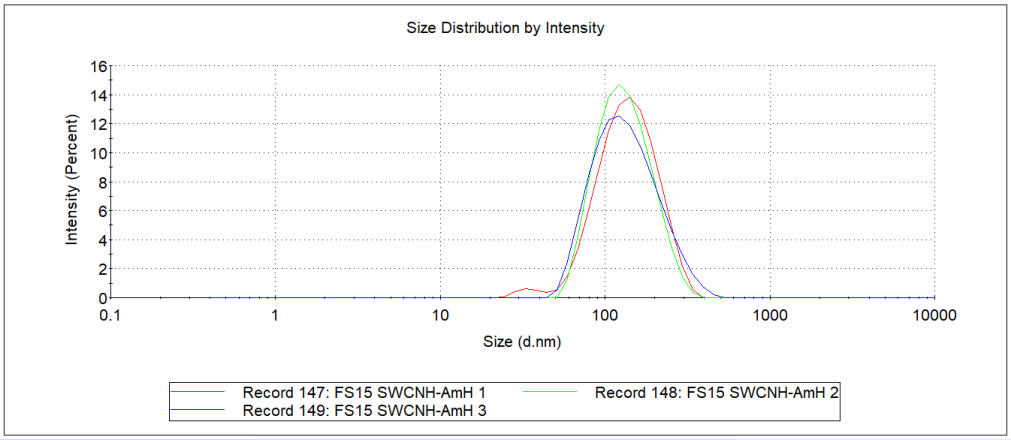

Figure 71: DLS measures of SWCNH-G in H_2O

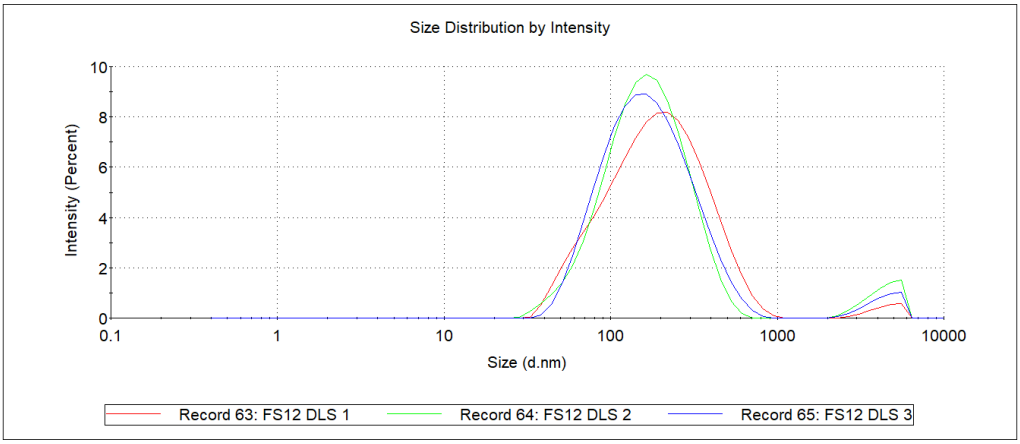

Figure 72: DLS measures of MWCNT-G in H_2O

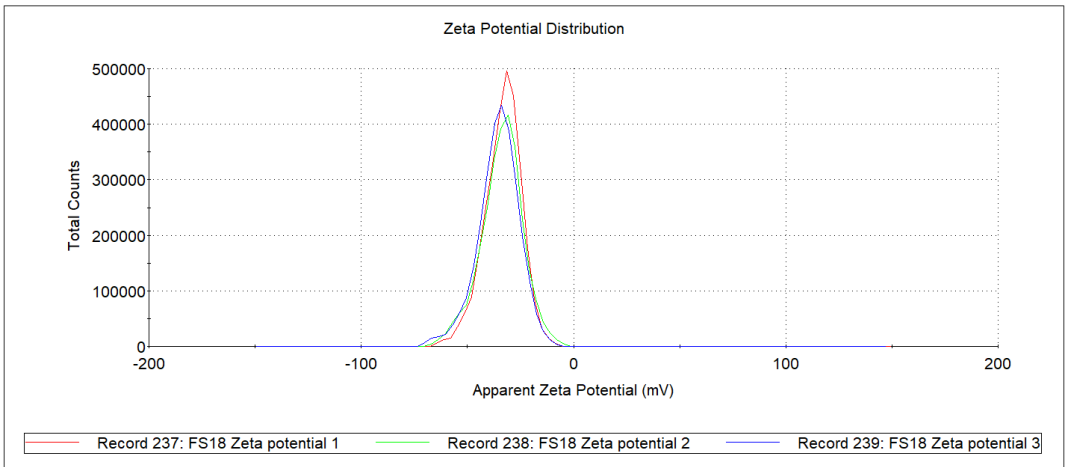

Figure 73: Zeta Potential measures of SWCNH-S in H_2O

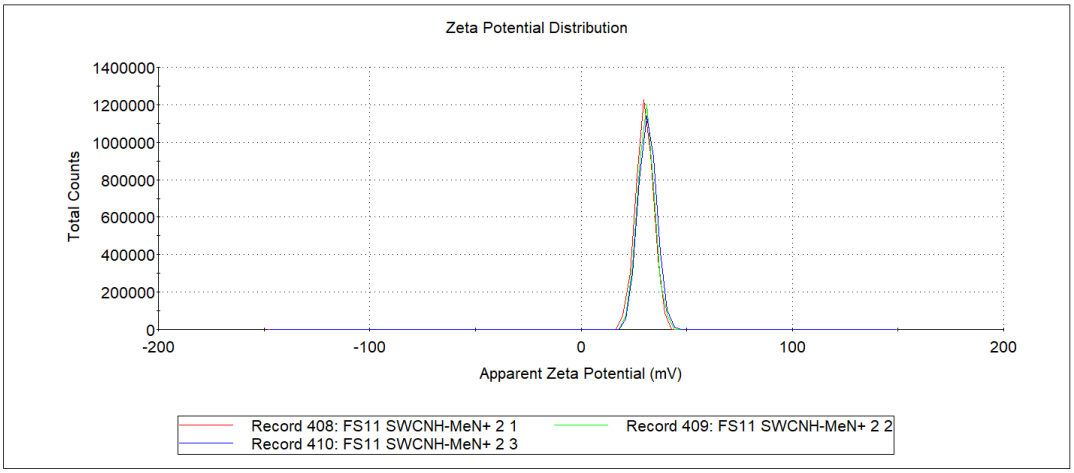

Figure 74: Zeta Potential measures of SWCNH-N in H_2O

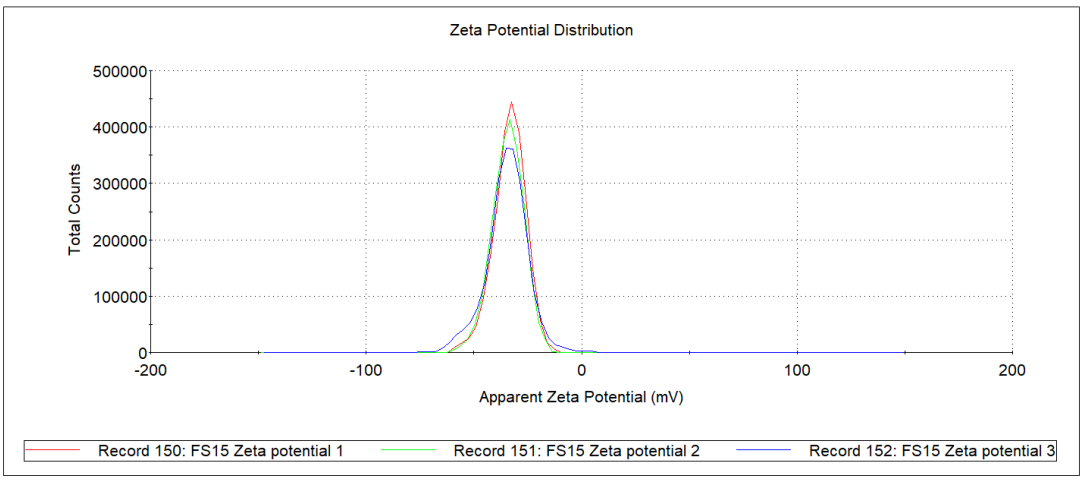

Figure 75: Zeta Potential measures of SWCNH-G in H_2O

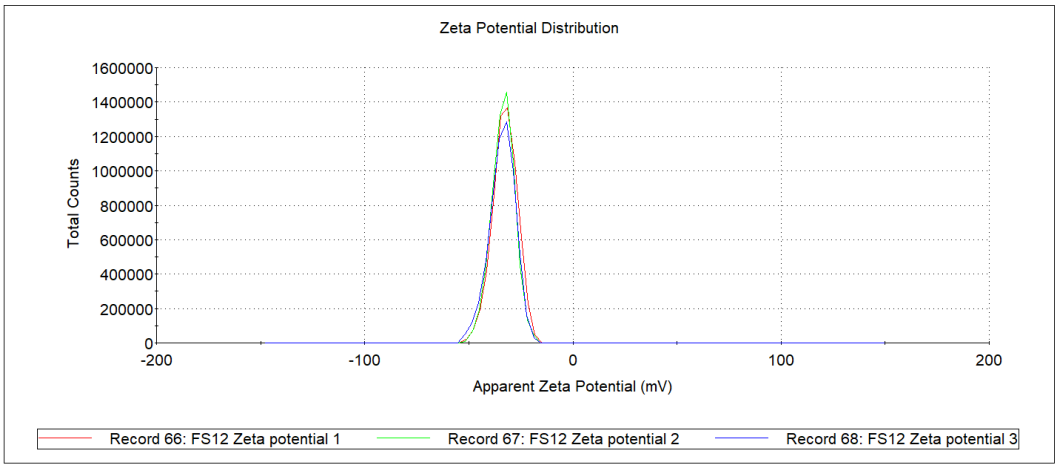

Figure 76: Zeta Potential measures of MWCNT-G in H_2O

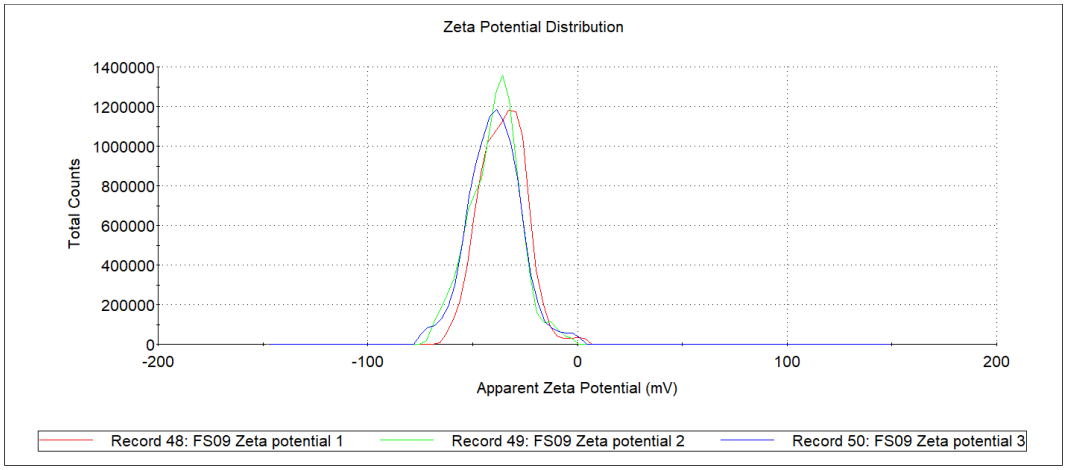

Figure 77: Zeta Potential measures of rGO-S in H_2O

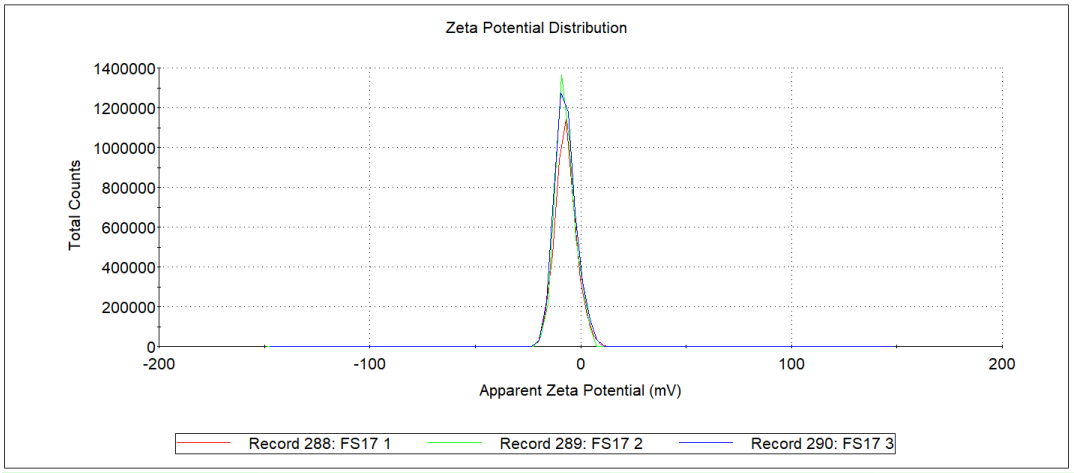

Figure 78: Zeta Potential measures of rGO-MeS in H_2O

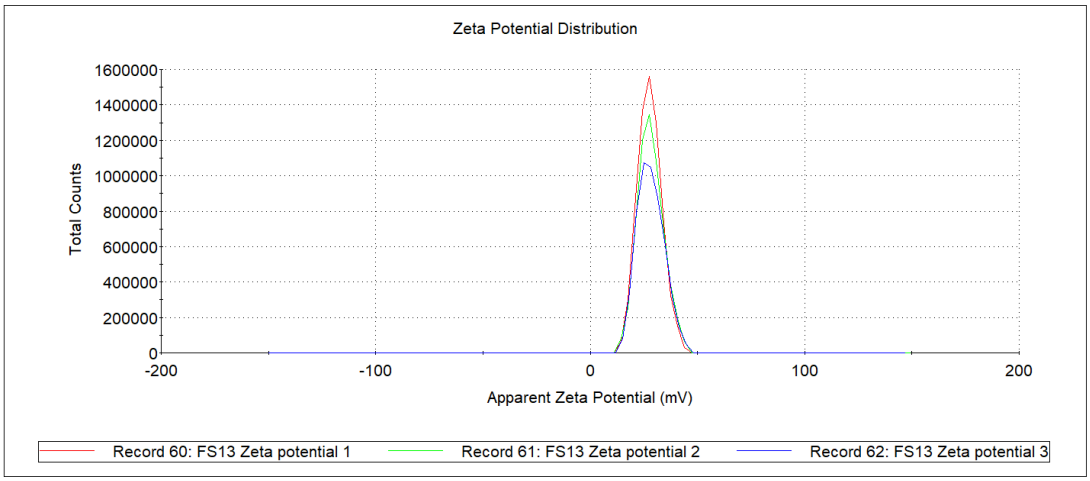

Figure 79: Zeta Potential measures of rGO-N in H_2O

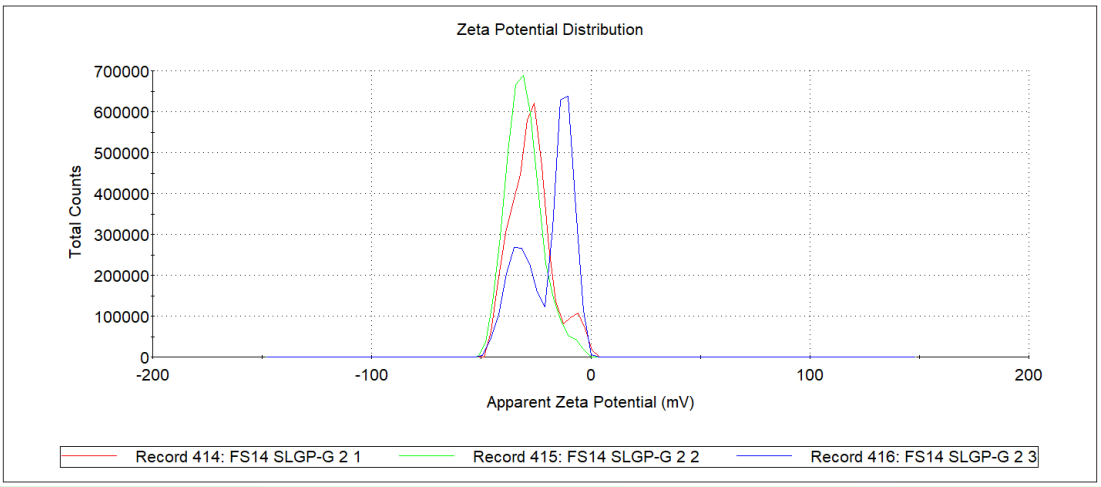

Figure 80: Zeta Potential measures of rGO-G in H_2O

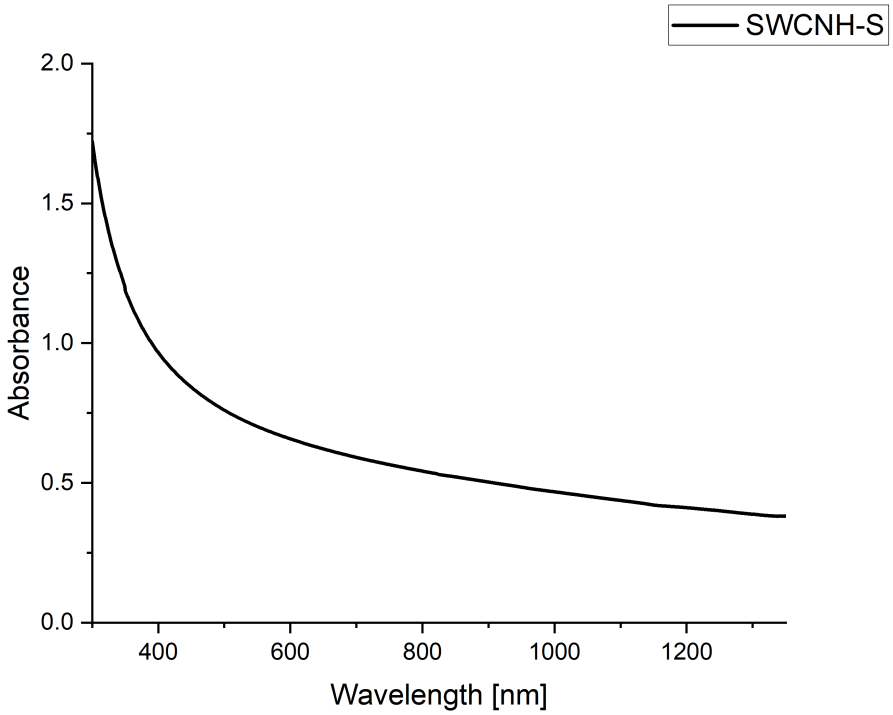

Figure 81: UV-Vis-NIR spectrum of SWCNH-S

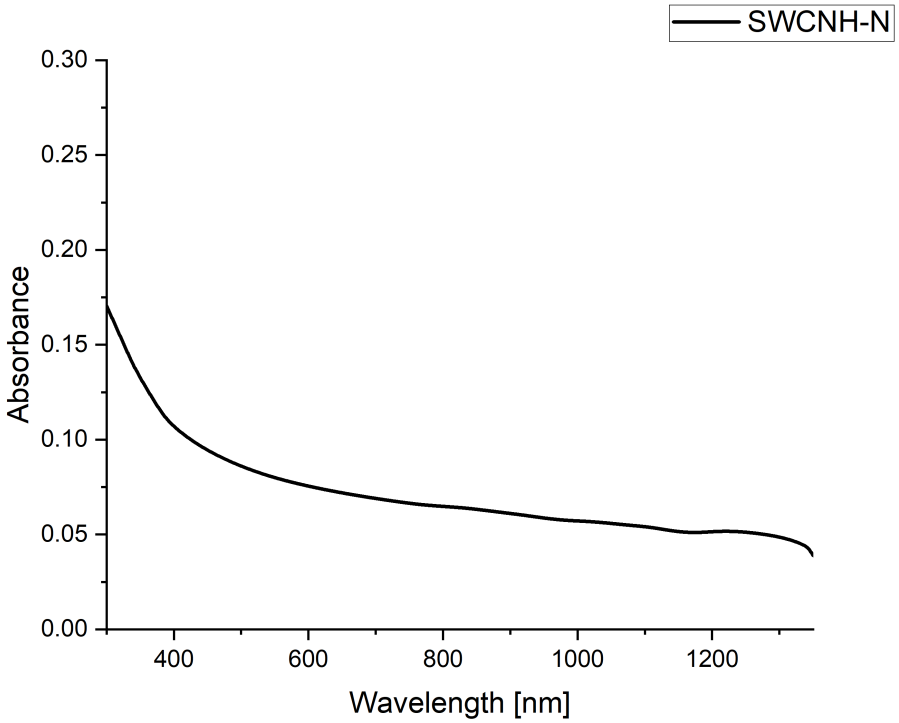

Figure 82: UV-Vis-NIR spectrum of SWCNH-N

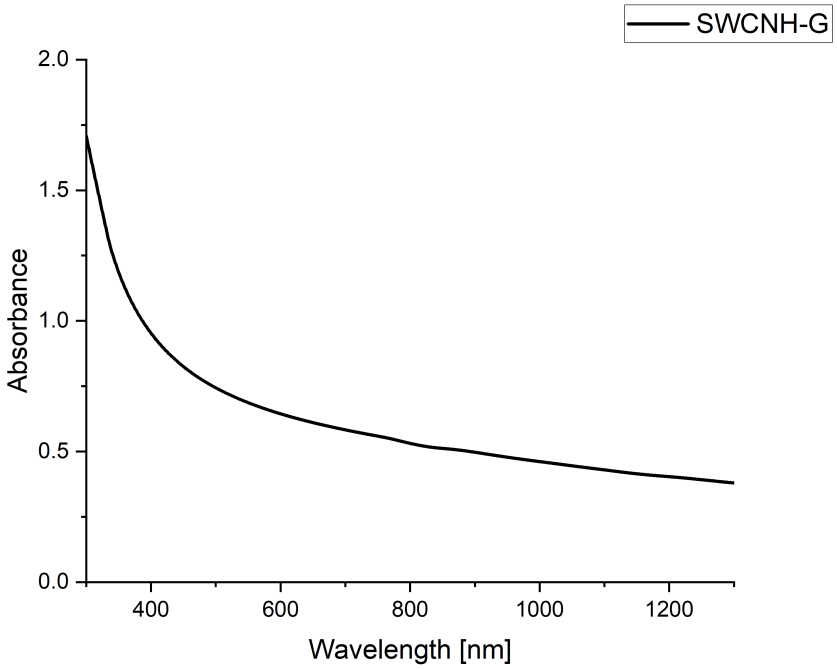

Figure 83: UV-Vis-NIR spectrum of SWCNH-G

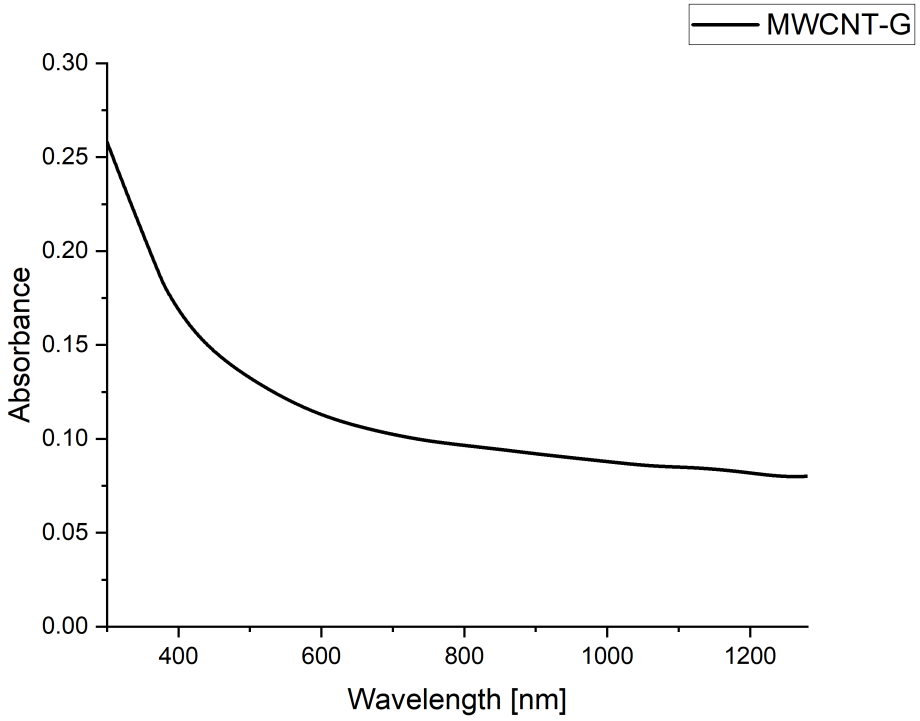

Figure 84: UV-Vis-NIR spectrum of MWCNT-G

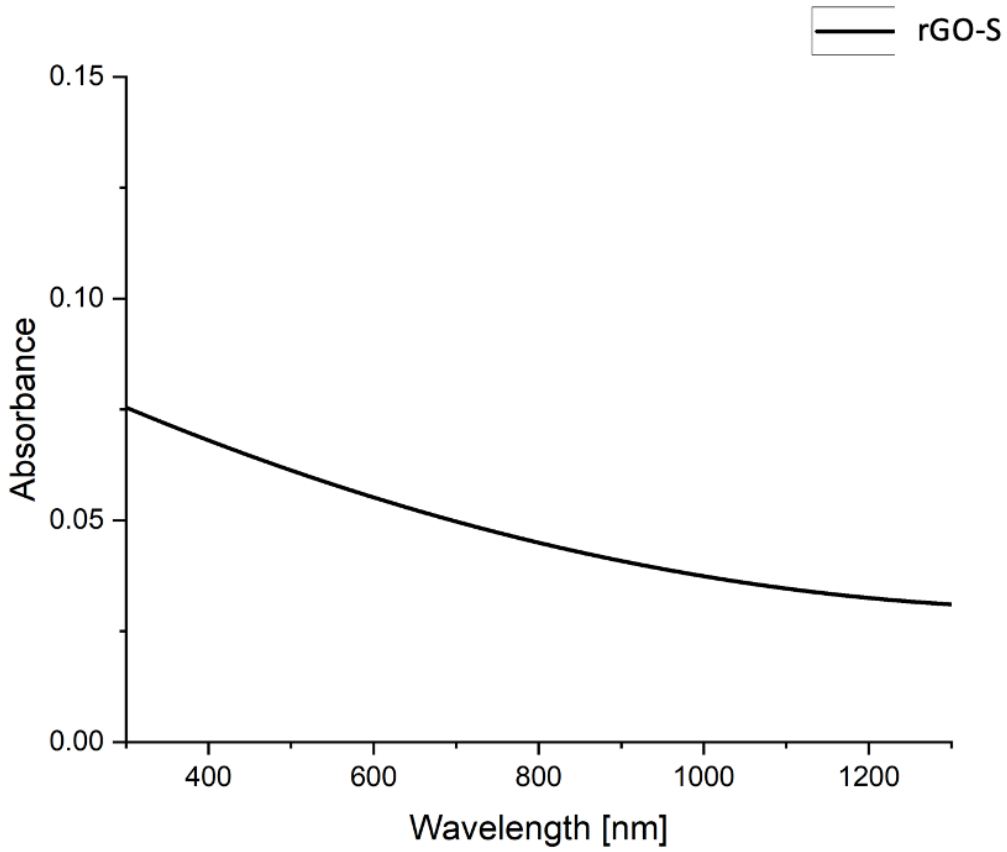

Figure 85: UV-Vis-NIR spectrum of rGO-S

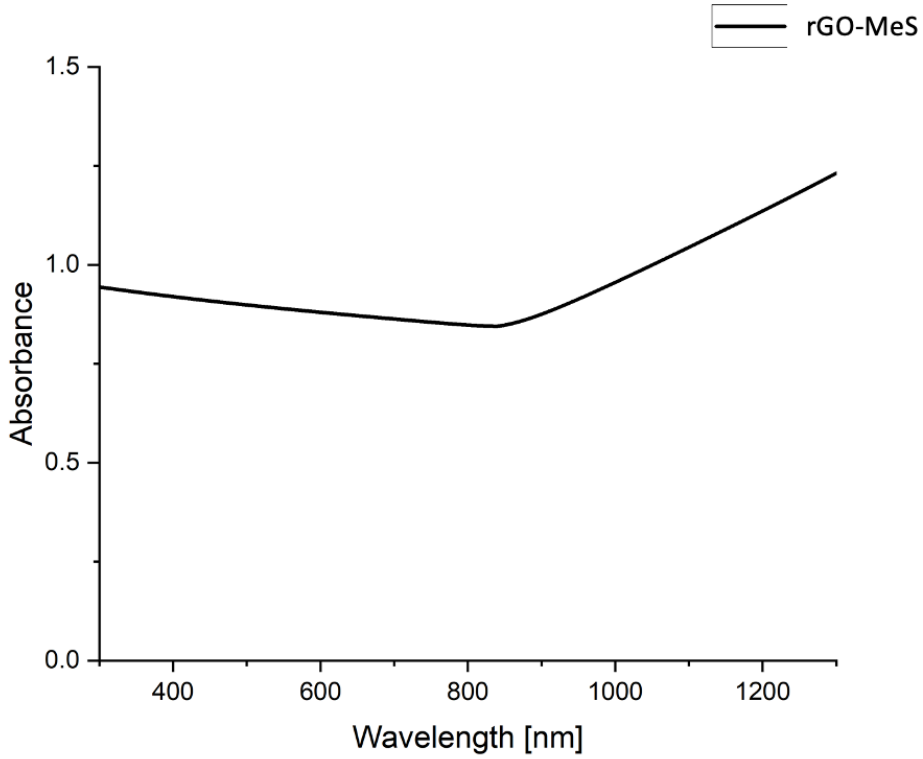

Figure 86: UV-Vis-NIR spectrum of rGO-MeS

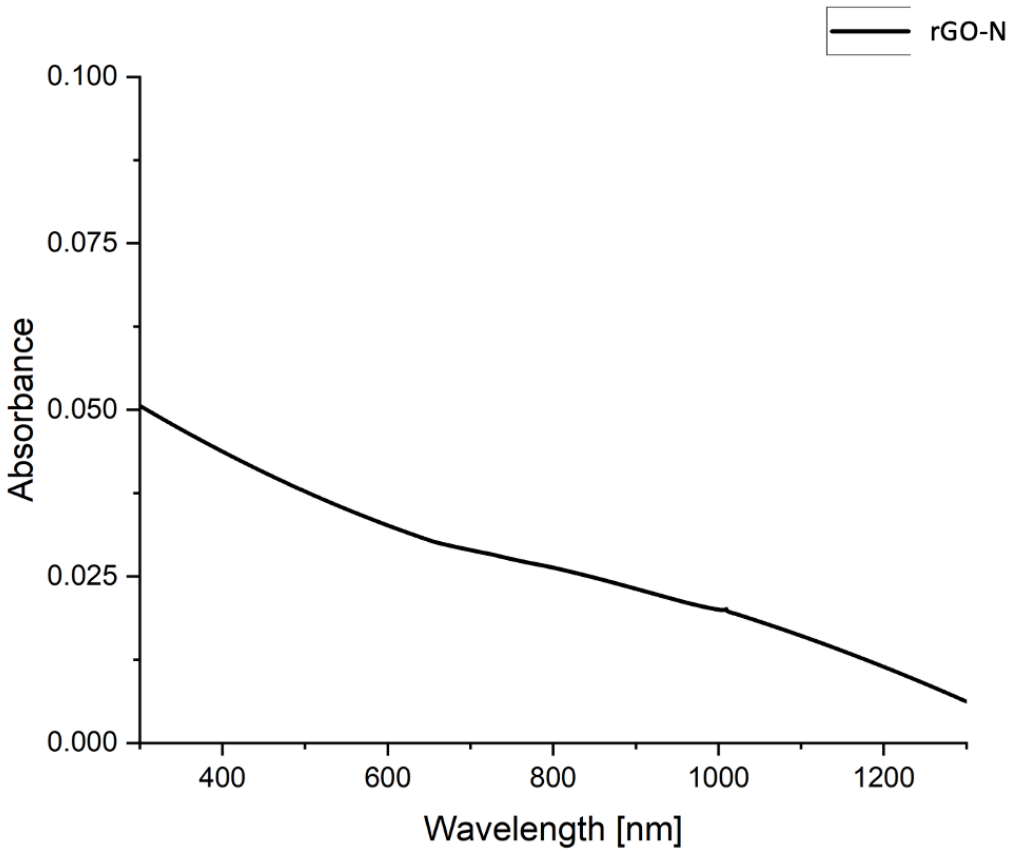

Figure 87: UV-Vis-NIR spectrum of rGO-N

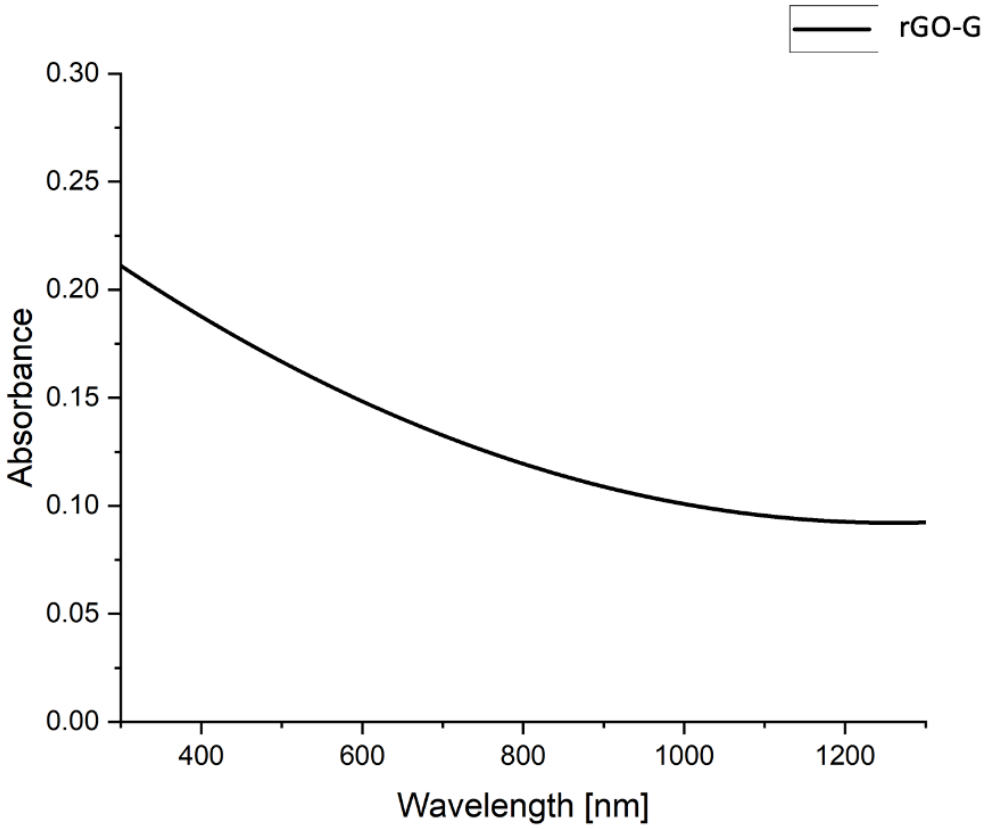

Figure 88: UV-Vis-NIR spectrum of rGO-G